The Dissertation Committee for Julian de Freitas Hallai
certifies that this is the approved version of the following dissertation:

On the Effect of Lüders Bands on the Bending of Steel Tubes

Committee:

Stelios Kyriakides, Supervisor

Michael D. Engelhardt

Chad M. Landis

Kenneth M. Liechti

Krishnaswa Ravi-Chandar

On the Effect of Lüders Bands on the Bending of Steel Tubes

by

Julian de Freitas Hallai, Dipl.-Ing.; M.E.; M.S.E.

Dissertation

Presented to the Faculty of the Graduate School of

The University of Texas at Austin

in Partial Fulfillment

of the Requirements

for the Degree of

Doctor of Philosophy

The University of Texas at Austin

December, 2011

Quelli che s'innamoran di pratica sanza scienza son come'l nocchier ch'entra in navilio sanza timone o bussola, che mai ha certezza dove si vada.

Leonardo Da Vinci

L'observateur doit être le photographe des phénomènes, son observation doit représenter exactement la nature. Il faut observer sans idée préconçue; l'esprit de l'observateur doit être passif, c'est-à-dire se taire; il écoute la nature et écrit sous sa dictée. Mais une fois le fait constaté et le phénomène bien observé, l'idée arrive, le raisonnement intervient et l'expérimentateur apparaît pour interpréter le phénomène.

Claude Bernard

Dedication

To my mother.

Acknowledgements

I would like to express my sincere gratitude to my advisor, Professor Stelios Kyriakides, for his guidance and tireless dedication throughout my studies. His work ethics, commitment to excellence and passion for research are unrivaled and shaped not only this research work but also my growth as researcher and teacher.

This project was conducted with financial support from a consortium of industrial sponsors, under the project Structural Integrity of Offshore Pipelines, which is acknowledged with thanks. I am also grateful for the support given by the Roberto Rocca Education Program and by the University of Texas at Austin.

I would also like to express my appreciation to the members of my dissertation committee, as well as the faculty of the Department of Aerospace Engineering and Engineering Mechanics. Prof. Mark Mear was very influential in my development as teacher.

The knowledgeable and constant computer support from Scott Messec was invaluable. The expertise of technicians Ricardo Palacios, Travis Crooks, Pablo Cortez, and Joseph Pokluda was of great help too.

The friendship of my fellow graduate students and their help motivated me through difficult times. A short list must include Dr. Liang-Hai Lee who is always happy to help and assisted me with my first experiments. The joyful support of Dr. Wen-Yea Jang, the stimulating discussions with Prof. Yannis Korkolis and the friendship of Brian Meason will be remembered. Stavros Gaitanaros often assisted me with my teaching duties and many times helped me to cool down. I am thankful for interacting with all these talented students on a daily basis.

My gratitude goes to Prof. Oscar B. Augusto at University of São Paulo who first introduced me to scientific research and always encouraged me and helped me to follow the academic path.

The unconditional love and support of my parents, Dirce and Alberto, and my brother Denis are warmly acknowledged with gratitude. I am grateful for a supportive family that has always encouraged me to pursue my goals.

My biggest appreciation goes to my wife, Daniella, for her sacrificial and endless love and support.

On the Effect of Lüders Bands on the Bending of Steel Tubes

Julian de Freitas Hallai, Ph.D.

The University of Texas at Austin, 2011

Supervisor: Stelios Kyriakides

In several practical applications, hot-finished steel pipe that exhibits Lüders bands is bent to strains of 2-3%. Lüders banding is a material instability that leads to inhomogeneous plastic deformation in the range of 1-4%. This work investigates the influence of Lüders banding on the inelastic response and stability of tubes under rotation controlled pure bending. It starts with the results of an experimental study involving tubes of several diameter-to-thickness ratios in the range of 33.2 to 14.7 and Lüders strains of 1.8% to 2.7%. In all cases, the initial elastic regime terminates at a local moment maximum and the local nucleation of narrow angled Lüders bands of higher strain on the tension and compression sides of the tube. As the rotation continues, the bands multiply and spread axially causing the affected zone to bend to a higher curvature while the rest of the tube is still at the curvature corresponding to the initial moment maximum. With further rotation of the ends, the higher curvature zone(s) gradually spreads while the moment remains essentially unchanged. For relatively low *D/t* tubes and/or short Lüders strains, the whole tube eventually is deformed to the higher curvature entering the usual hardening regime. Subsequently it continues to deform uniformly until the usual limit moment instability is reached. For high *D/t* tubes and/or materials with longer Lüders strains, the propagation of the larger curvature is interrupted by collapse when a critical

length is Lüders deformed leaving behind part of the structure essentially undeformed. The higher the *D/t* and/or the longer the Lüders strain is, the shorter the critical length.

This class of problems is analyzed using 3D finite elements while the material is modeled as an elastic-plastic solid with an "up-down-up" response over the extent of the Lüders strain, followed by hardening. The analysis reproduces the main features of the mechanical behavior provided the unstable part of the response is suitably calibrated. The uniform curvature elastic regime terminates with the nucleation of localized banded deformation. The bands appear in pockets on the most deformed sites of the tube and propagate into the hitherto intact part of the structure while the moment remains essentially unchanged. The Lüders-deformed section has a higher curvature, ovalizes more than the rest of the tube, and develops wrinkles with a characteristic wavelength. For every tube *D/t* there exists a threshold of Lüders strain separating the two types of behavior. This bounding value of Lüders strain was studied parametrically.

Table of Contents

Nomenclature

a	imperfection amplitude
D	outer diameter
D_o	mean diameter $(= D - t)$
$D_{\max}$, $D_{\min}$	maximum and minimum diameter
E	Young's modulus
E'	slope of the softening stage
F_i	force on i^{th} node
I	moment of inertia
L	tensile specimen gage length or tube effective half-length
m	rate exponent
M	moment
M_o	fully plastic moment $(= \sigma_L {D_o}^2 t)$
N	number of nodes
R	radius of fillet, radius of tube
s	natural coordinate
t	thickness
T	temperature
w	width of tensile specimen or outward normal displacement
w_C	outward normal displacement on the compressive side
w_T	outward normal displacement on the tensile side
$\overline{w}$	initial geometric imperfection
x, y, z	cartesian coordinates
x_o	location of the Lüders front

α	orientation angle of bands w.r.t. axial direction
β	imperfection parameter
δ	cross-head displacement
Δ	ovality $\left(= D_{\max} - D_{\min} / D_{\max} + D_{\min}\right)$
Δ_o	initial ovality
ΔD	change in external diameter in the plane of bending
$\Delta\varepsilon_L$	Lüders strain
$\Delta\varepsilon_{LB}$	bounding Lüders strain
$\Delta\sigma$	material model parameter
ε	strain
ε_{bL}	maximum bending strain at κ_L
$\varepsilon_e{}^p$	equivalent plastic strain
$\dot{\varepsilon}_o$	reference strain rate
$\dot{\varepsilon}^p$	plastic strain rate
θ	slope of tube
$\theta_1,\ \theta_2$	angle of rotation of sprockets
θ_L	angle of rotation at the end of the tube
$\bar{\theta}_{CO}$	average angle of rotation of the two ends of the tube at collapse
$\bar{\theta}_L$	average angle of rotation of the two ends of the tube
κ	curvature
κ_1	normalizing curvature $(= t / D_o{}^2)$
κ_L	curvature at limit moment
λ	wrinkle half-wavelength
λ_e	elastic axisymmetric wrinkle half-wavelength
ν	Poisson's ratio

σ	stress
σ_e	von Mises equivalent stress
σ_L	lower yield stress
σ_U	upper yield stress
$\Sigma(\varepsilon^p)$	measured stress-plastic strain relationship at reference strain rate
ϕ	angle with respect to plane of bending
$\dot{(\ )}$	time derivative or rate

Chapter 1: INTRODUCTION

Offshore pipelines often experience bending that takes the structure into the plastic range. Plastic bending can develop during the installation of the pipeline but also during its operation. Thus, for example, installing the pipeline by the reeling method results in winding it onto a reel with a hub radius of a few meters resulting in strains of 2-3% (Ch. 2 in Kyriakides and Corona, 2007). Other examples that can involve significant plastic bending of a pipeline include upheaval buckling of a buried line due to the passage of hot hydrocarbons at high pressure (Ju and Kyriakides, 1988), and lines installed on the sea floor which are intentionally designed to buckle laterally at regular intervals (*snaking*) in order to relieve the compression induced by temperature and pressure (Bruton et al., 2005).

It is well known that plastic bending of tubes is limited by structural instabilities that are governed by the tube diameter-to-thickness ratio (D/t) and the characteristics of the stress-strain response of the material. Bending ovalizes the tube cross section (Brazier, 1927) gradually reducing its bending rigidity and leads to a limit load instability that is followed by localized deformation and local collapse. This is the limit state of lower D/t tubes. Wrinkling on the compressed side is a second type of instability, which for higher D/t tubes leads to collapse by local kinking (e.g., see Ju and Kyriakides, 1991, 1992; Kyriakides and Ju, 1992; Corona et al., 2006; Kyriakides and Corona, 2007). For intermediate D/t values wrinkling and localization of ovalization can interact (Ju and Kyriakides, 1991).

Plastic bending of tubes is further complicated when the steel exhibits Lüders bands, a material instability that leads to localized deformation over a certain strain range. The main objective of this dissertation is to understand how Lüders bands changes

the response of tubes under bending and how it influences the extent to which they can be safely bent.

1.1 LÜDERS BANDS

Lüders banding, as is known today, is a dislocation driven phenomenon that macroscopically manifests as localized deformation. In the simplest setting involving a uniaxial test on a low carbon steel strip, immediately after first yielding, inclined bands of plastic deformation develop locally. Under displacement controlled stretching, the bands propagate gradually consuming the test section as shown in Fig. 1.1a. During this process, the stress remains essentially unchanged tracing a plateau as shown in Fig. 1.1b. This propagation phase is characterized by the coexistence of two deformation regimes, represented by the dark and lighter colors in the test section shown in the figure. The plateau has a strain range of 1-4%. At the termination of the stress plateau, the material returns to homogeneous deformation and the usual strain hardening behavior.

The phenomenon was first observed by Lüders (1860) during bending of soft cast-steel rods. Several lines appeared on the surface of the bent rods, which he subsequently showed to become more prominent if etched with a weak solution of nitric acid. He did not associate these lines with localization of strain, but attributed them to "molecular motion". Other names given to the phenomenon include Piobert-Lüders bands (Piobert et al., 1842), Hartman lines (after Hartman, 1896), stretcher strains, strain markings and strain or flow figures.

The manufacturing industry views the Lüders bands as undesirable visible surface markings, detracting from the appearance of fabricated metal products (Baren and Nelson, 1970). Thus, they have, mostly empirically, focused on avoiding the phenomenon by means of operations such as temper rolling or skin pass. An expensive

alternative to low-carbon steel is the use of aluminum-killed steel or reducing the carbon and nitrogen content to very low levels. These options are usually not exercised in pipeline manufacture primarily in order to control the costs.

Two main theories for the occurrence of Lüders bands have survived the test of time. Cottrell and Bilby (1949) attributed the upper yield stress in low-carbon steel to the pinning of dislocations by carbon and nitrogen atoms, which naturally tend to form "atmospheres" around them. They postulated that initial yielding requires a higher stress in order to pull the dislocations out of their atmospheres. Once released, the dislocations can be moved by a lower stress, inducing a drop in stress. The pinning effect of interstitial impurities is widely accepted for several reasons including the reappearance of Lüders strain following mild heat-treatment, which allows these atoms to migrate and repin the dislocations (strain aging).

For a limited range of strain rates and temperatures, the increasing mobility of solutes leads to repetitive pinning and unpinning of dislocations, associated with stress drops and rises. This phenomenon is known as Portevin-Le Chatelier (PLC), after Le Chatelier (1909) and Portevin and Le Chatelier (1923), and is associated with *strain rate softening* (Penning, 1972).

The second theory for the appearance of Lüders bands was proposed by Johnston and Gilman (1959), who attributed the load drop to multiplication of dislocations; as their number increases, the stress required to move them decreases (see also Johnston, 1962 and Hahn, 1962). In both theories, Lüders bands are associated with *strain softening*.

1.2 BENDING WITH LÜDERS BANDS

Published accounts of bending with Lüders bands although very limited actually started as early as Lüders' paper in 1860. Nakanishi (1931) investigated Lüders bands in

tension, torsion and bending (see also Nakanishi, 1929, and Nakanishi et al., 1934). He used Fry's etching method (Fry, 1921) to reveal the bands occurring in mild steel square beams under bending. Angled wedge-like localized deformation patterns that start on the surface and die when they approach the neutral axis were observed (see Fig. 1.2).

An attempt at simulating bending of a solid with Lüders bands was made by Shioya and Machida (1984) (see also Shioya and Shiroiri, 1976). They used the work of Johnston and Gilman (1959) and Hahn (1962) and a criterion of yield initiation based on a continuously distributed dislocations model to simulate numerically the yield process of mild steel beams under plane strain bending. They essentially employed a constitutive model that involved an unstable stress-strain curve with gradually decreasing negative slope after the upper yield point. The paper reports some success in reproducing localized wedge-like through thickness deformation bands that have some similarity to those observed by Nakanishi.

Aguirre et al. (2004) studied the interaction of wrinkling and Lüders banding in higher *D/t* tubes (27.2). A moment plateau was traced during which pockets of inclined Lüders bands were found to emanate from peaks of wrinkles. Kyriakides et al. (2008) showed that for a relatively thick tube ($D/t = 18.7$) under pure bending the interaction with Lüders strain of about 1.8% also resulted in an extended moment plateau. As the plateau was being traced two curvature regimes co-existed, one approximately corresponding to the strain at the end of the stress plateau and the second to that at the beginning of the plateau. Under rotation-controlled bending, the larger curvature regime gradually propagated until the whole length of the tube was consumed. Subsequently, the moment increased monotonically and the structure resumed homogeneous bending deformation.

1.3 OUTLINE

This work is a continuation of the studies mentioned above, examining in detail the effect of the tube *D/t* and of the unstable material behavior on the response and stability of tubes under bending. Of particular interest is the complex interaction of Lüders bands in low-carbon steel with the structural instabilities intrinsic to tubular structures under bending. The investigation consists of a large number of small-scale experiments followed by numerical modeling by means of finite element simulations. The focus of Chapter 2 is on the material instability. Tensile tests are reported, followed by simulations using the finite element method and a discussion of the constitutive model used and of the modeling of the phenomenon. Chapter 3 presents representative bending results from an extensive study that involved tubes of several *D/t* values in the range of 33.2 to 14.7 and Lüders strains of 1.8% to 2.7%. These experiments, produce a wealth of phenomena associated with the interaction of Lüders bands with structural nonlinearities. These phenomena are numerically simulated using FE models along with custom constitutive models that aim to reproduce the macroscopic effects of Lüders banding. The results of these simulation efforts are reported in Chapter 4. Once the veracity and robustness of the models is proven, they are used to conduct an extensive parametric study of the problem, presented in Chapter 5. The main findings and conclusions are summarized in Chapter 6.

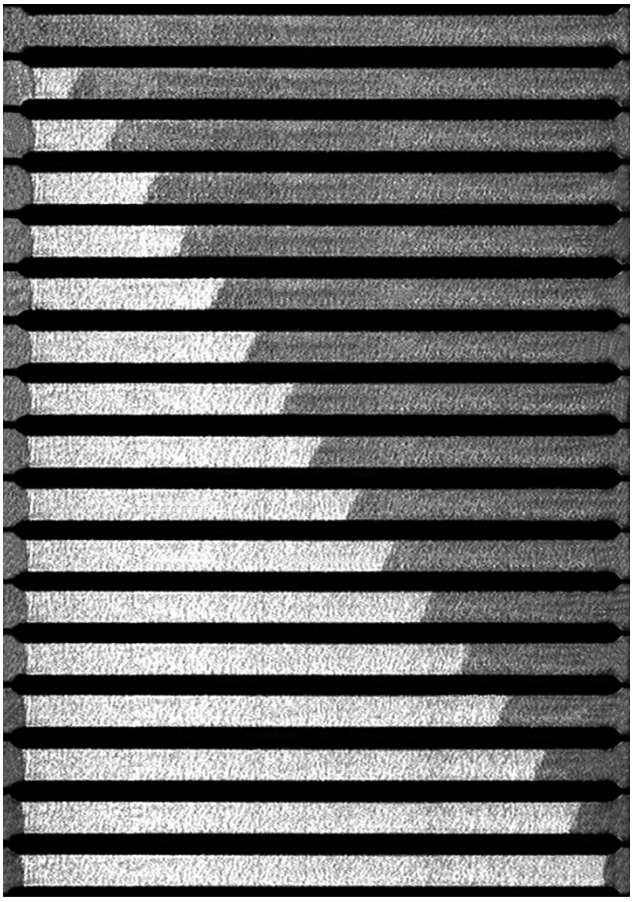

(a)

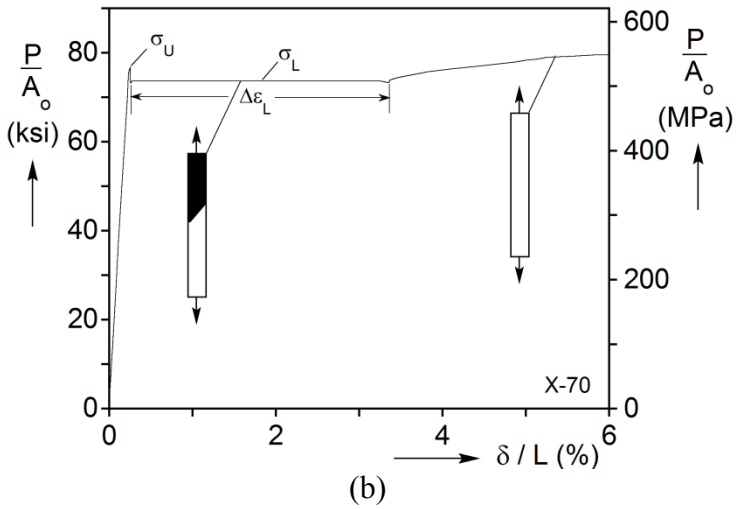

(b)

Fig. 1.1 (a) Photographic sequence showing evolution of Lüders strain. (b) Stress-strain response of a steel exhibiting Lüders banding. (Kyriakides and Miller, 2000).

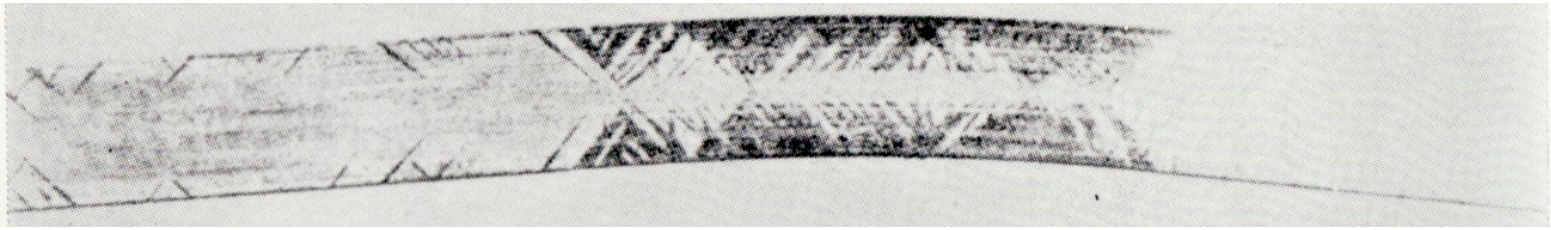

Fig. 1.2 Lüders bands revealed by etching after bending a square beam (Nakanishi, 1929, 1931, 1934).

Chapter 2: MATERIAL CHARACTERIZATION

Before delving into the behavior of tubes with Lüders bands under bending, it is important to understand and be able to model the performance of the material in a simpler setting. This chapter describes uniaxial tension tests on the steels that will be used in the tube bending experiments. The uniaxial tests are subsequently simulated numerically using a constitutive model with a softening branch.

2.1 EXPERIMENTS

All uniaxial tests were performed in standard testing machines (either servo-hydraulic or screw type) under displacement control. The tests were performed at room temperate at the slow rate of $\dot{\delta}/L = 10^{-4}$ s^{-1}. About 70 tensile tests were performed on two materials: 1020 carbon steel and X-65 line-grade steel. Each experiment was performed at least three times and found to be repeatable. The 1020 steel specimens were 0.375×5.750 in (10×146 mm) rectangular strips longitudinally cut out of the tubes that will be used in the bending experiments. The X-65 steel specimens (see Fig. 2.1) were machined from a plate, originally 3/4 in (19 mm) thick; they were extracted along the rolling direction. In addition to the stress-elongation responses, full-field measurements were obtained using brittle coating and digital image correlation techniques.

Figure 2.2 shows a typical engineering stress–elongation response ($\sigma - \delta/L$, L is the length of the test section) recorded in a uniaxial test with Lüders bands. The response is initially linearly elastic and the deformation is uniform along the specimen. Localized plastic deformation initiates at σ_U (upper yield stress) with a sudden drop in stress. Under displacement control, Lüders deformation spreads along the length of the specimen, while the stress remains essentially constant ($\sigma_L \equiv$ lower yield stress, or plateau stress). Part of the specimen has been plastically deformed to the Lüders strain (

$\Delta\varepsilon_L \approx 2.58\%$) while the rest of it is still at the end of the linear elastic regime. Hence, *the macroscopic effect of the material instability is inhomogeneous deformation*. When the whole test section has been deformed to the Lüders strain, the material hardens and the specimen reverts to homogeneous deformation. For such a response, the yield stress is assigned the value of the plateau stress σ_L (45.1 ksi = 313 MPa).

Figure 2.3 shows the continuation of this response until failure of the specimen. The material hardens from a strain of about 2.8% to 21.4%, deforming homogeneously. It reaches an ultimate stress of 59.8 ksi (412 MPa). Beyond this point, the specimen necks and failure occurs at 32.2% strain.

The inhomogeneous nature of the deformation was illustrated by Kyriakides and Miller (2000) (see also Fig. 13.4 in Kyriakides and Corona, 2007) using tensile tests on strips made from similar steels. The strips were coated with *Stresscoat*, a brittle lacquer that shattered at a strain of about 1%, allowing one to differentiate between Lüders deformed material and undeformed material (difference in reflectivity between shattered and intact coating).

A more quantitative analysis can be obtained using the *Digital Image Correlation* technique (DIC), which is a full-field non-contact image analysis method. Before the experiment, the specimen is sprayed first with white paint and then with black paint creating a stochastic intensity pattern on its surface (Fig. 2.4). The experiment is recorded on digital video or timed photography. After the experiment, a post-processing computer program compares the digital images with the first image (corresponding to the reference or undeformed state of the specimen) and calculates the displacement and deformation over the specimen for each image. The image comparison is based on the maximization of a correlation coefficient that is determined by examining pixel grayscale intensities

and extracting the deformation mapping function that relates the images. The method essentially tracks the grayscale intensities in small neighborhoods during deformation.

DIC was used in experiment LU-P5. As expected, the stress-elongation response (Fig. 2.5) is initially linearly elastic, has an upper yield point followed by a stress plateau and then hardening. Figure 2.6 shows contours of axial strain obtained using DIC, corresponding to the locations marked on the response with numbered solid bullets. During the elastic regime, the deformation is homogeneous, as seen in configuration ①. The stress then reaches a local maximum, drops and starts to trace a plateau. In configuration ②, the left end of the specimen has been deformed to about 3%, which corresponds to the strain at the end of the stress plateau; the rest of the specimen is strained to less than 0.5%, still in the elastic deformation regime. From configuration ② to configuration ⑩ a relatively sharp inclined front separating the two strain levels (which remain constant) propagates at nearly constant speed, gradually consuming the specimen as the stress plateau is exhausted. By configuration ⑪, now in the hardening stage of the response, the specimen is seen to be deformed homogeneously again and from this point on, the specimen is deformed uniformly until a maximum stress is reached.

The plastic deformation associated with Lüders banding generates some heat, which tends to heat up the specimen locally. Although at the slow rate at which the tensile tests were conducted the temperature increase was relatively small, it was possible to measure it using a Thermovision® SC4000/6000 infrared camera. The camera was set to monitor the complete gage length and this provided an alternative means of tracking the propagation of the Lüders deformation front. A sequence of recorded temperature contours that correspond to the numbered bullets on the response in Fig. 2.5 is plotted in Fig. 2.7. Although not as sharp as the front separating the two strain levels in Fig. 2.6, it

is possible to track the propagation of a region with slightly larger temperature (~0.5 ^{o}C difference) than its surroundings. Thus, the hottest region is seen in configurations ② to ⑩ to propagate from left to right essentially in the same manner as the front in the strain contours in Fig. 2.6. The front is not as sharp as in the DIC images due to the diffusive character of heat as opposed to lack of resolution in the readings.

In the example presented above, the initiation of the Lüders bands occurred at the left end, followed by propagation of one front from left to right until the specimen is entirely consumed. Nevertheless, this is not always the case. As discussed by Kyriakides and Miller (2000), some tests have two (or more) fronts propagating from the ends of the specimen towards its center. Figure 2.8 shows DIC axial strain contours from an experiment that developed two fronts. It is interesting to note that the localization at the left end initiates along one of the characteristics but quickly switches to the other one (see also Shaw and Kyriakides, 1998). This minimizes the bending moment and keeps the specimen straighter, so it is often a preferred mode of deformation.

2.2 NUMERICAL SIMULATIONS

2.2.1 Constitutive Model

Lüders banding is a dislocation governed material instability, which macroscopically manifests as discontinuous deformation. Simple considerations of dislocation motion put forward initially by Johnston and Gilman (1959) and expanded upon by Hahn (1962) demonstrated that up-down-up stress-strain responses could be derived from such a premise (see also Johnston, 1962). In this work, a simpler, phenomenological, but equivalent approach to this constitutive challenge is followed. An unstable material response is introduced over the extent of the Lüders stress plateau. The construction has a stress peak that is associated with the upper yield stress and a negative

slope over the length of the stress plateau. At the end of the measured stress plateau, the response reverts to stable hardening behavior thus producing the required up-down-up trajectory associated with propagating instabilities (see Kyriakides, 1993, 2001).

Indeed, it has been demonstrated that an elastic-plastic constitutive model calibrated to such a response can reproduce quite faithfully several of the macroscopic effects of Lüders banding (Kyriakides and Miller, 2000; Corona et al. 2002; Aguirre et al., 2004; Kyriakides et al. 2008; see also Shaw and Kyriakides, 1998 and Shaw, 2000, who applied a similar model to propagation of phase transformation bands in a shape memory alloy during loading). Tsukahara and Iung (1998, 1999), Wenman and Plant (2006), Zhang et al. (2008) and Carr et al. (2009) adopted the same idea to simulate Lüders banding with finite elements. Itoh et al. (1992) used Hahn's constitutive equation to obtain an up-down-up material response. Yoshida (2000) and Yoshida et al. (2008) used a constitutive model with an exponential stress drop induced by multiplication of dislocations. Ballarin et al. (2009) adopted a similar strategy, using an exponential up-down-up stress strain curve. Iricibar et al. (1977) used an up-down-up curve in the form of a "stress concentration factor" to explain the propagation of plastic deformation.

Here, a similar constitutive framework is implemented. Thus, a measured engineering stress-strain response such as the one drawn in red color in Fig. 2.9 is modified as follows. The initial linear elastic branch with the measured modulus E is adopted. The elastic branch terminates at the upper yield stress that is $\Delta\sigma/2$ higher than the plateau (σ_L) of the measured response. It is followed by a linear softening branch, which is drawn with a blue dashed line in the figure. Its termination point at the end of the Lüders stress plateau is at a level that makes the areas of the two shaded triangles equal (i.e., $\sigma_L \equiv$ Maxwell stress, Ericksen, 1975; Abeyaratne and Knowles, 2006). Beyond this point, the fit follows the hardening part of the measured stress-strain

response (in piecewise linear manner). In summary, the material is modeled as a finitely deforming elastic-plastic solid that hardens/softens isotropically. The model is calibrated to the true stress-logarithmic strain version of the measured stress-strain response as shown in Fig. 2.9.

It is well known that the introduction of softening in a constitutive model can lead to severe mesh dependence of FE solutions. Such is not the case for the up-down-up stress-strain response assumed here because it exhibits a relatively mild softening that lasts only for part of the deformation history. It will be demonstrated here that the simulation of tensile tests employing such constitutive modeling exhibits negligible mesh dependence. We have still opted, however, to regularize the problem by introducing "mild" rate dependence to the material (see Needleman, 1988; Nacar et al., 1989, among others). We introduce this rate dependence for numerical expediency even though we realize that the steels used in our experiments exhibit specific rate dependence. Furthermore, strain rate has been shown to affect the plateau stress especially when the rate is properly measured locally in the propagating Lüders front (e.g., Hall, 1970; Imamura et al., 1971). A more careful representation of rate dependence is left for a future investigation. Rate dependence is introduced via the commonly used power law as follows:

$$\left(\frac{\dot{\varepsilon}^p}{\dot{\varepsilon}_o}\right)^m = \frac{\sigma}{\Sigma(\varepsilon^p)}. \qquad (2.1)$$

Here $(\dot{\bullet})$ represents a time derivative, $\dot{\varepsilon}_o$ is a reference strain rate, $\Sigma(\varepsilon^p)$ is the measured stress-plastic strain relationship when $\dot{\varepsilon}^p = \dot{\varepsilon}_o$, and m is the rate exponent. For the present materials $\Sigma(\varepsilon^p)$ is the plastic strain version of responses like the one in Fig. 2.9 measured at a rate of $\dot{\varepsilon}_o = 10^{-4}\,s^{-1}$. The rate exponent used is m = 0.001, which is

enough to regularize the numerical solution while simultaneously having only a small effect on the predicted events.

2.2.2 Finite Element Model

The axial response such as the one in Fig. 2.9 is now simulated numerically using a FE model of the axial strip tested. Lüders banding results in inhomogeneous deformation with jumps in strain of the order of the Lüders strain. As in Aguirre et al. (2004) and Kyriakides et al. (2008), we adopt ABAQUS's incompatible elements C3D8I. These are linear elements enhanced to allow for the deformation gradient inside the element to vary while displacement continuity is maintained (see Wilson et al., 1973; Ortiz et al., 1987; Nacar et al., 1989; Simo and Armero, 1992). In order to avoid any directional bias a uniform isotropic mesh is used (see Fig. 2.10). The mesh adopted has two elements through the thickness of the strip, 14 elements along the width and 132 along the length. This density was arrived at from a convergence study that will be discussed later in this section. The model is fixed at the left end while the right end is restrained in the *y*- and *z*- directions and is assigned displacement at constant rate in the *x*-direction ($\dot{\delta}/L = 10^{-4}$ s^{-1} as in the experiments). These boundary conditions induce stress concentrations that trigger localization at both ends of the strip, which occurs along two characteristics as seen in Fig. 2.11 (the bands are inclined at ±55° to the direction of loading: see Bijlaard, 1940; Hill, 1948; and discussion by Shaw and Kyriakides, 1998). In order to initiate a single band, two elements through the thickness on the lower left corner of the strip have σ_U reduced by 2%.

2.2.3 Initiation of Localized Deformation

The finite element model described above is used to simulate Exp. LU-P5. The material response adopted in this simulation is the one drawn with a blue dashed line in

Fig. 2.9. Aguirre et al. (2004) pointed out that the slope of the softening part of the assumed response or, alternatively, the assumed $\Delta\sigma/\sigma_L$ (see Fig. 2.9) must be within a certain range. $\Delta\sigma/\sigma_L = 0.148$ was found to give good results in this case.

Figure 2.12a shows an expanded view of the initial part of the stress-elongation response. Marked on it with solid bullets are 4 points that will help follow the events that take place during the initiation of plastic deformation. Localized deformation starts at point *A*, when the two weaker elements are plastically deformed. Figure 2.12b shows a set of three deformed configurations of the strip, corresponding to the bullets on the response. The color contours represent the equivalent plastic strain. At point *B* the elements at the four corners of the model have been plastically deformed due to stress concentrations. The response reaches a local maximum at *C* and the deformation localizes along two characteristics at both ends of the model. The plastic strain in these bands is about 0.10% (or 0.36% total strain). Beyond this point, the stress drops and all plastic deformation localizes in one of the characteristics on the left side of the model.

2.2.4 Propagation of Localized Deformation

Figure 2.13 shows the calculated stress-elongation response with the elongation normalized by the gage length (drawn in blue color). Figure 2.14 shows a set of nine deformed configurations of the strip, corresponding to the numbered bullets on the response (color contours represent the equivalent plastic strain). The stress-elongation response is seen to reproduce the main features of the corresponding measured response: the initial stress maximum, the level of the stress plateau that follows and the subsequent stable branch are reasonably well reproduced. The extent of the stress plateau is a little longer in the simulation. This increase is proportional to $\Delta\sigma$ and inversely proportional to the slope of hardening stage. The configurations in Fig. 2.14 show localization first

occurring at the left end of the strip and gradually spreading along the length. Configuration ①, still in the linearly elastic part of the response, is free of Lüders bands. In configuration ②, two distinct zones of deformation have developed joined by an inclined front; the Lüders deformed zone is at about 3% while the rest is still at the end of the linearly elastic part of the response (0.26%). The front propagates at constant velocity along the length of the model while the stress remains essentially unchanged. The propagation of the front continues in configurations ② to ⑧ gradually deforming the specimen. The stress plateau is exhausted when the left end is reached in configuration ⑨; the material then enters the hardening regime and the specimen is seen deforming homogeneously again.

2.2.5 Local Response

A representative true stress-equivalent plastic strain response at an integration point is shown in Fig. 2.15. The local response follows the prescribed material curve for the most part, except at the transition between the softening regime and the hardening stage. Figure 2.16a and 2.16b contains the history of true stress and equivalent plastic strain as a function of time for the same integration point (see element in white in Fig. 2.16c). The stress at this integration point initially increases linearly, subsequently remaining constant during the propagation of the Lüders bands on the left of the element. The equivalent plastic strain at the integration point is zero during this stage. At t = 140 s, the front approaches the integration point. The stress then follows the up-down-up trajectory as the equivalent plastic strain increases from zero up to the Lüders strain (see Fig. 2.16b). It takes about 10 s for the front to pass this integration point. After that, the stress and the strain remain essentially constant as the front is propagating to the right of this point. The stress increases after the entire strip is Lüders deformed.

2.2.6 Influence of the Mesh

At this point, it is important to investigate the sensitivity of the simulation to the mesh. Three other isotropic meshes were considered that had 1, 4 and 8 elements through the thickness with a total of 462, 29,586 and 236,544 elements respectively. The corresponding stress-elongation responses are presented in Fig. 2.17. The only noticeable differences occur in the transitions between the linearly elastic and Lüders propagation regime and between the Lüders propagation and (homogeneous) hardening regime. Furthermore, the largest change occurs when comparing the mesh with one element through the thickness with the other meshes. The more refined meshes have essentially the same response as the mesh with element size $t/2$.

More interestingly, Fig. 2.18 shows that the front width is essentially the same for meshes with element sizes $t/2$, $t/4$ and $t/8$. The mesh with element size t is not able to resolve the strain gradient in the front. Figure 2.19 shows a photomicrograph of the grain distribution representative of the steels being analyzed. The grain size is of the order of 8-20 μm. Drawn in the micrograph is a square frame with 120 μm sides, which corresponds to the size of the element of the most refined mesh considered ($t/8$). The element is seen to cover about 8 grains indicating that this mesh is quite fine. Since no mesh dependence was observed we conclude that the problem does not appear to exhibit any mesh dependence. Furthermore, as seen in Fig. 2.20, this result does not depend on the rate exponent either. These analyses show that the up-down-up stress-strain response does not present the same pathological mesh dependence obtained when using softening in other localization problems. Shaw and Kyriakides (1997) and Shaw (2000) simulated the behavior of thin uniaxial NiTi strips using up-down-up stress-strain curves and noted that the strip thickness was the relevant continuum length scale of interest. They did not observe any mesh dependency either.

2.2.7 Front Width

The width of the front in the model is approximately *2t*. The precise geometric characterization of the front is left for a future study but, from the present results, it is clear that the width is influenced by the thickness while the angle of the propagating front is governed by the constraint that the strain along the band be zero. Experimental results confirm the dependence of the front width on the geometry of the specimen when the thickness is large compared to the grain size (Hall, 1950; Moon, 1971; Fujita and Miyazaki, 1978). Lomer (1952) already observed that the grain size affects the sharpness of the Lüders bands but that the band pattern depends primarily on the specimen size and shape. Van Rooyen (1968) measured the strain distribution in a propagating Lüders front and observed that the effective width of the front is proportional to the thickness of a strip specimen. Ananthan and Hall (1991) observed that the nature of the band front depends on the geometry of the cross-section of the specimen.

2.2.8 Conclusion

The results of the finite element numerical simulations confirm that the deformation during Lüders banding, characterized by a propagating narrow angled front, is strongly influenced by overall geometric (structural) effects, suggesting that continuum level events are dominant, regardless of the micromechanical mechanisms involved in Lüders banding. A continuum constitutive model with softening over part of the material response reproduces the main macro mechanical features of the problem.

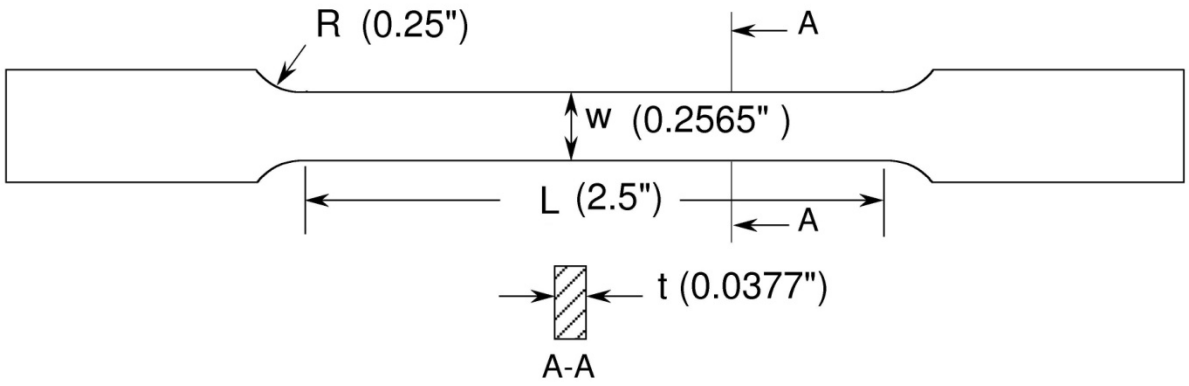

Fig. 2.1 Tensile test specimen geometry used to study Lüders banding.

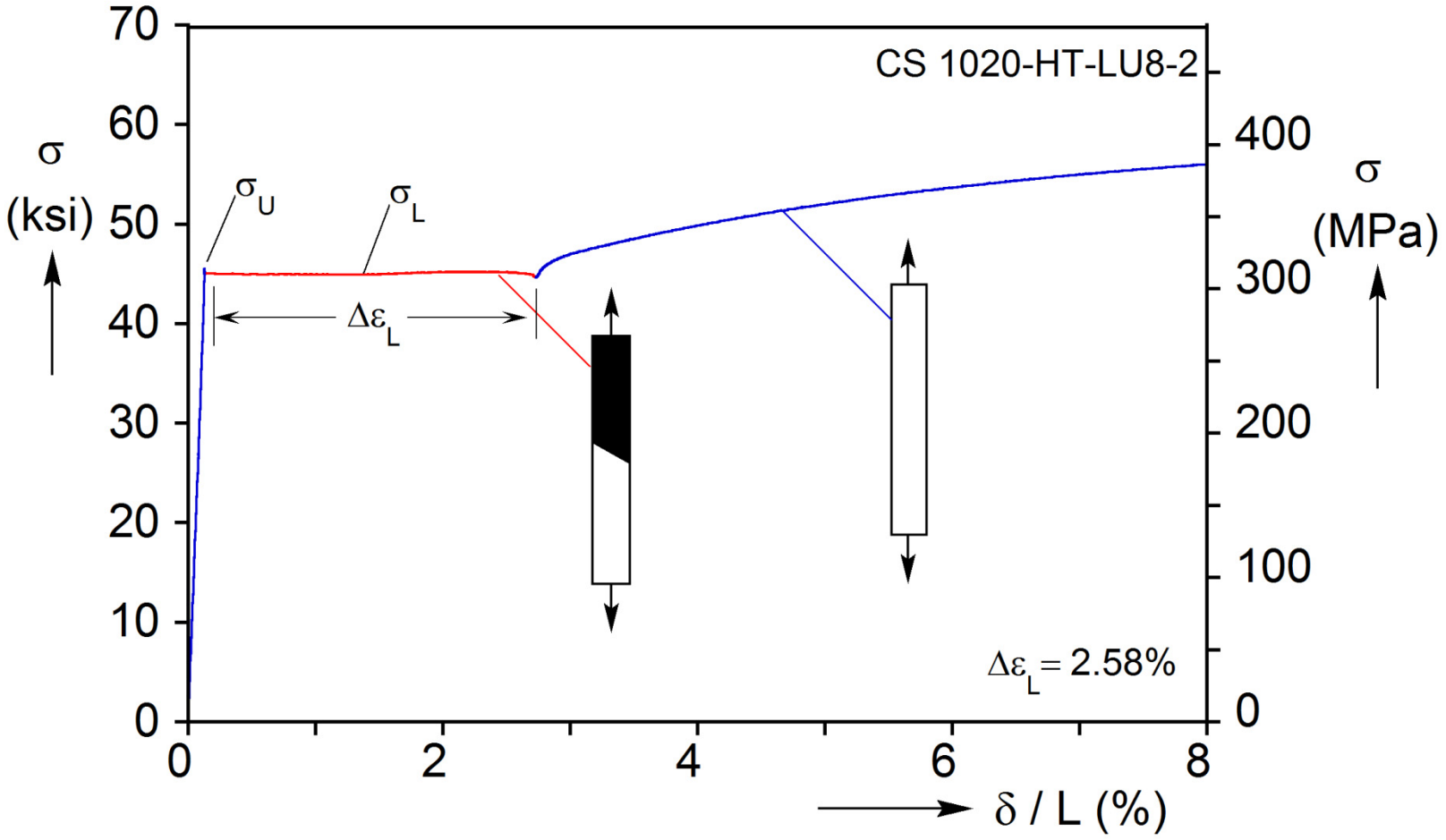

Fig. 2.2 Stress-elongation response of a carbon steel exhibiting Lüders deformation of 2.58% followed by hardening: small strain regime.

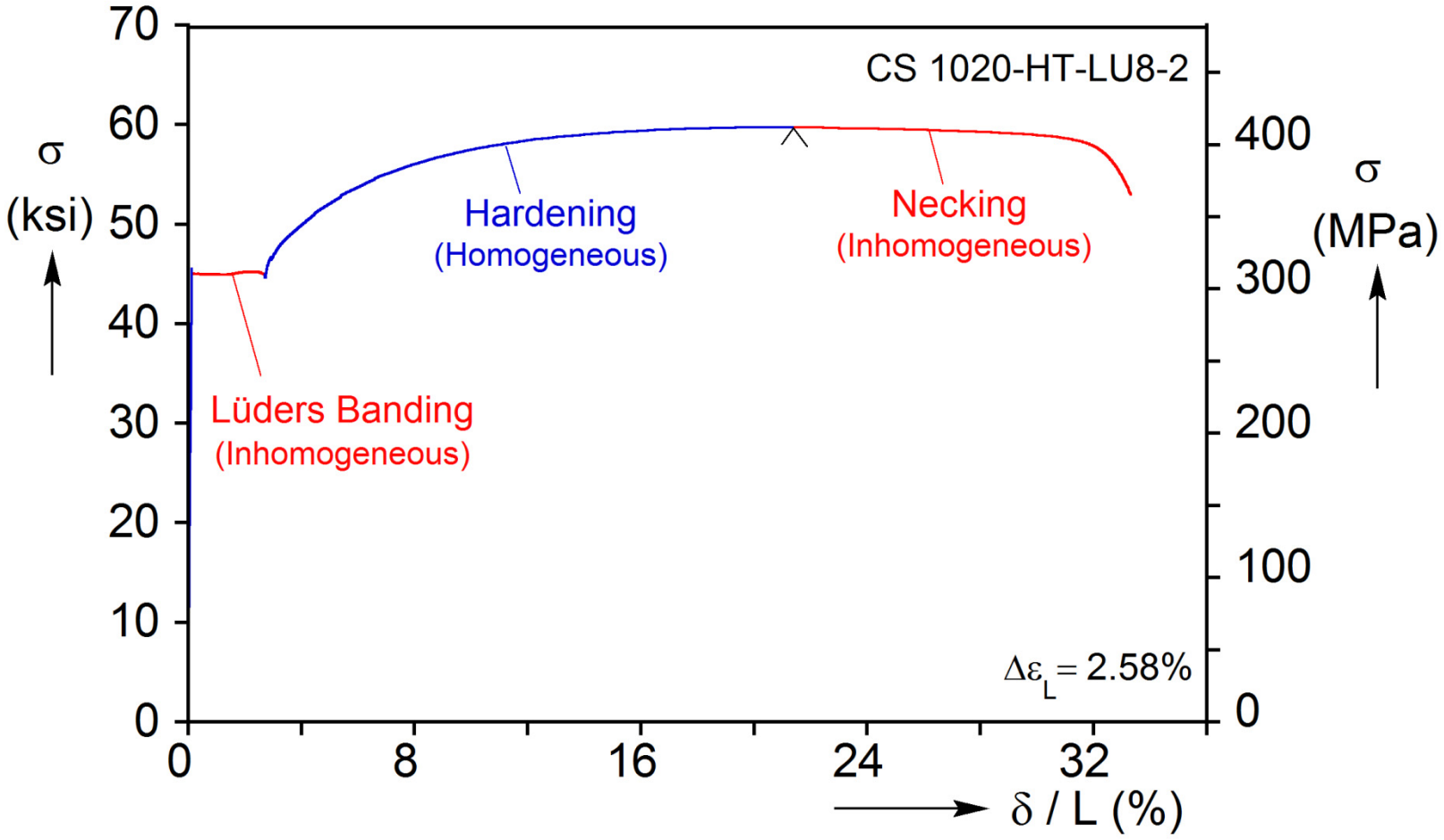

Fig. 2.3 Stress-elongation response of a carbon steel exhibiting Lüders deformation of 2.58% followed by hardening: pulled to failure.

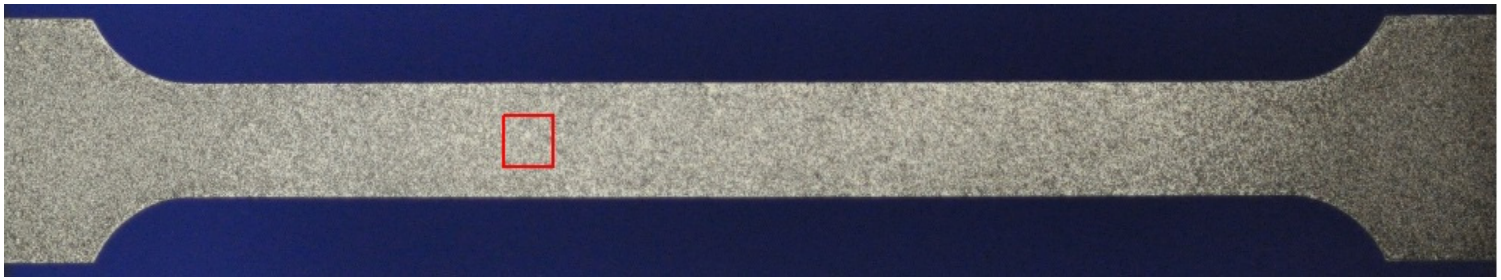

(a)

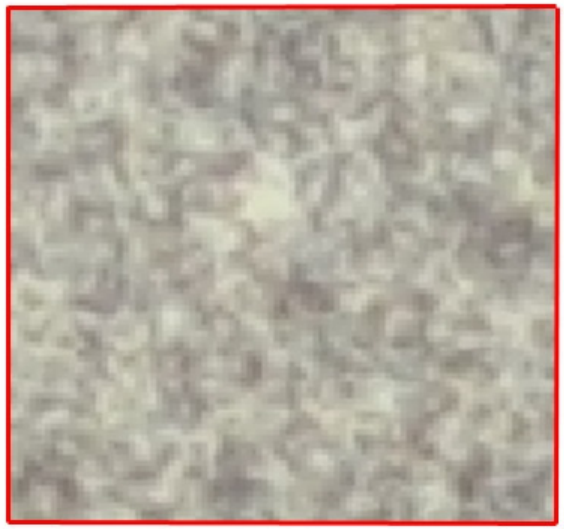

(b)

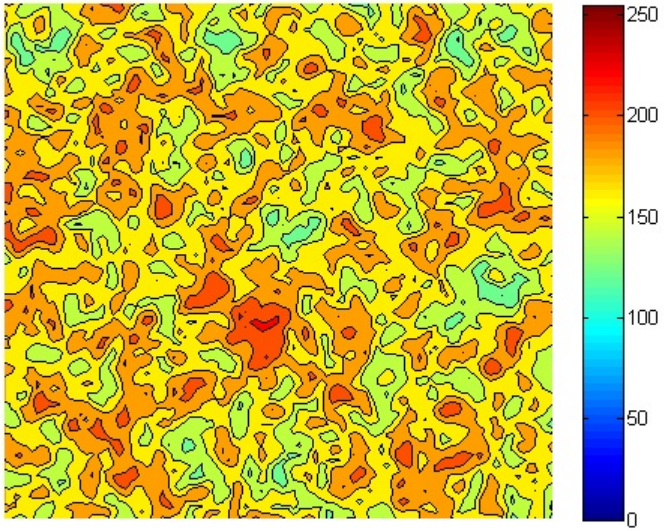

(c)

Fig. 2.4 (a) Stochastic pattern on the surface of specimen LU-P4, (b) 100 x 100 pixels window and (c) corresponding grayscale levels.

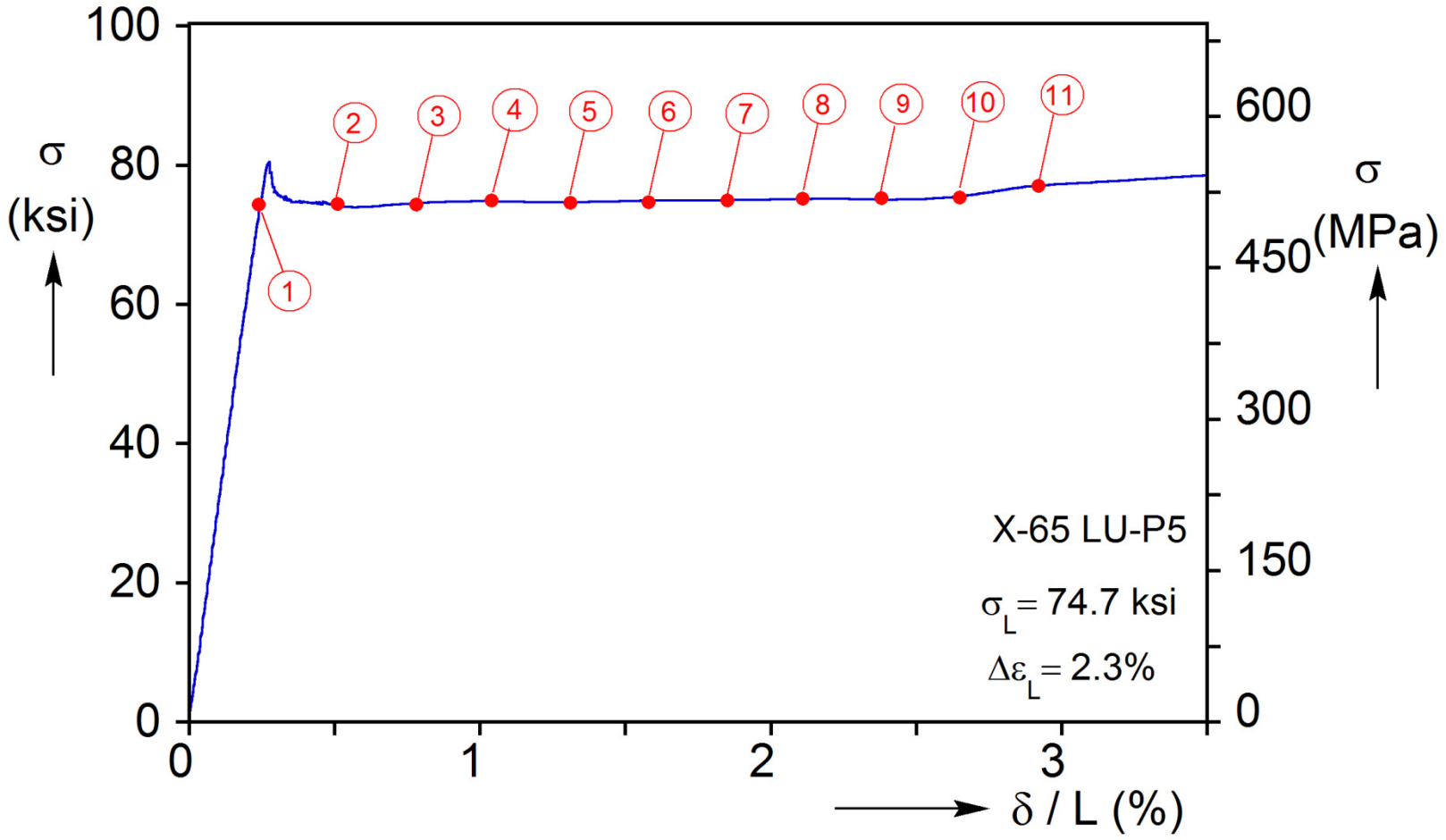

Fig. 2.5 Stress-elongation response of Exp. LU-P5.

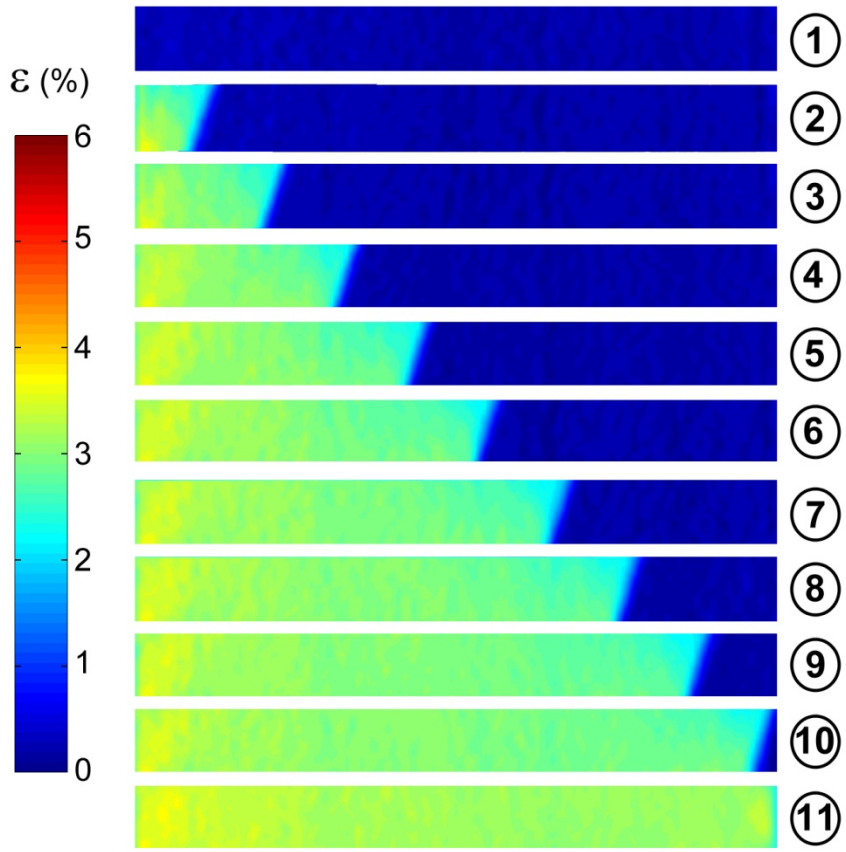

Fig. 2.6 Contours of axial strain for Exp. LU-P5 (numbers correspond to bullets marked on response in Fig. 2.5).

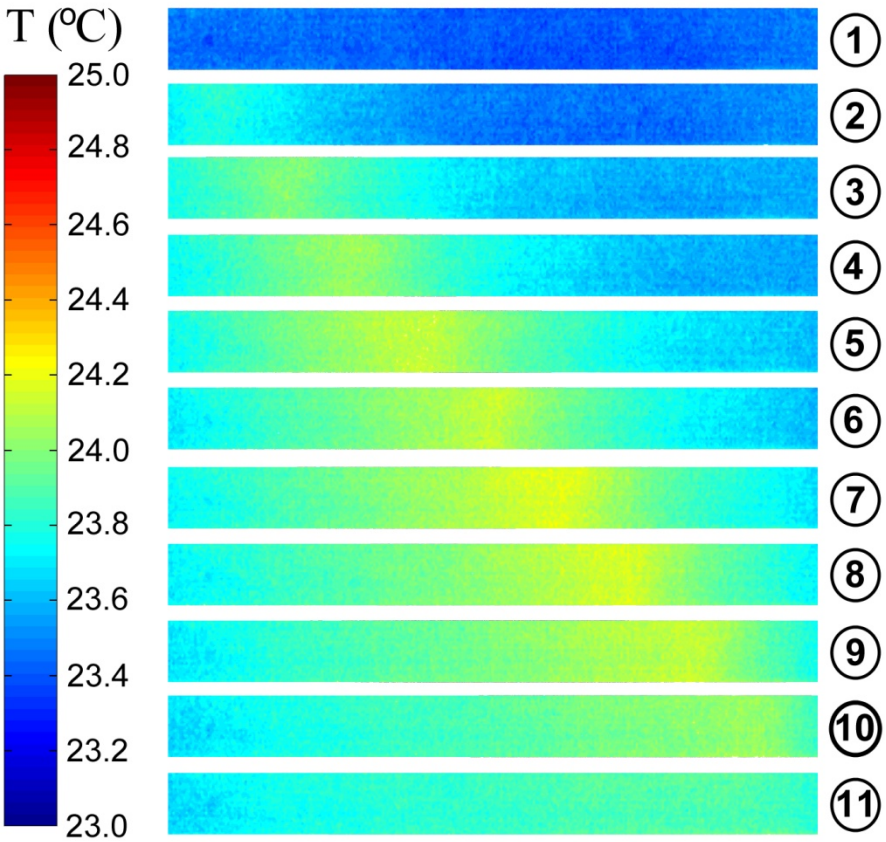

Fig. 2.7 Surface temperature for Exp. LU-P5 (numbers correspond to bullets marked on response in Fig. 2.5).

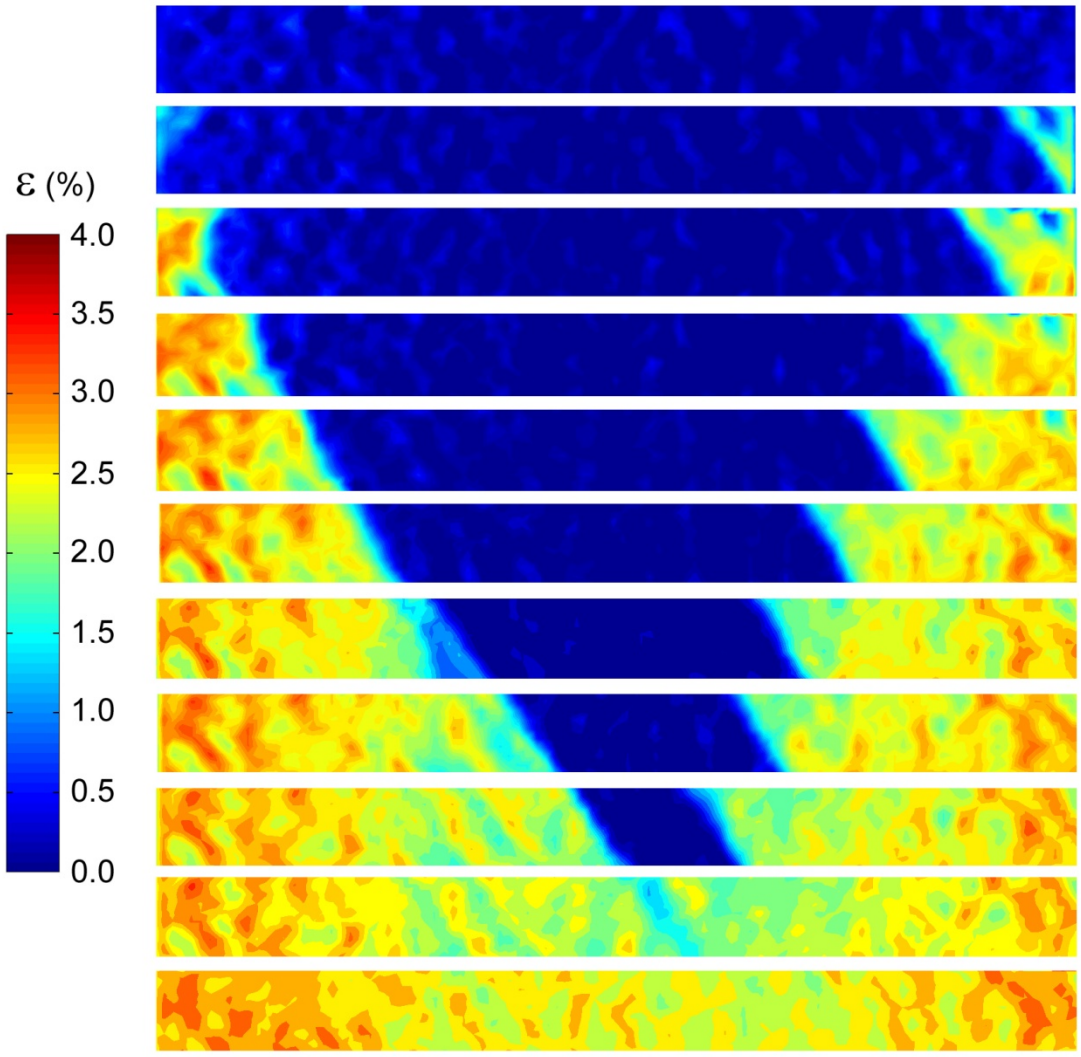

Fig. 2.8 Two coexisting Lüders fronts propagating towards each other (Exp. LU11-2-DIC-1).

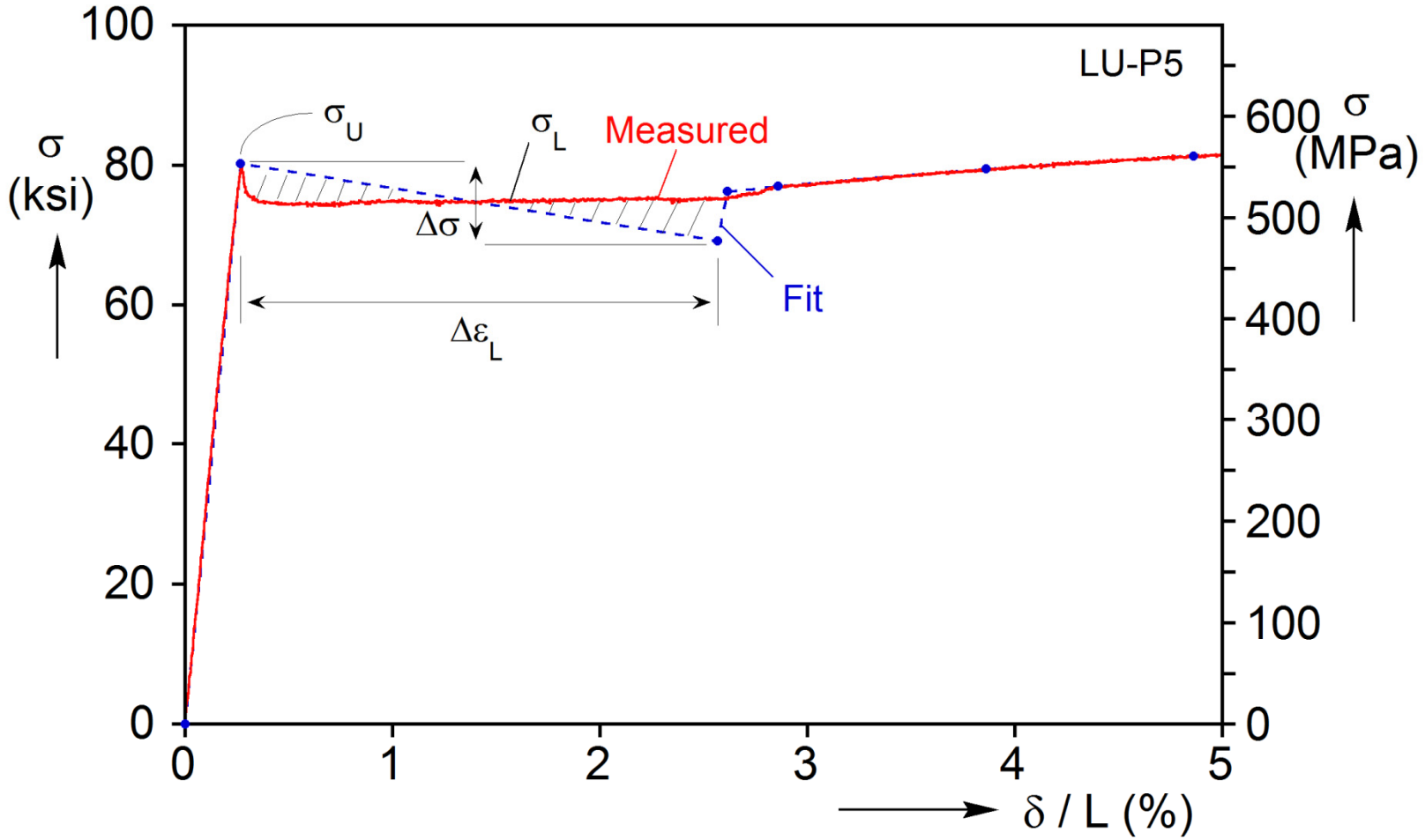

Fig. 2.9 Measured response and stress-strain response adopted for LU-P5.

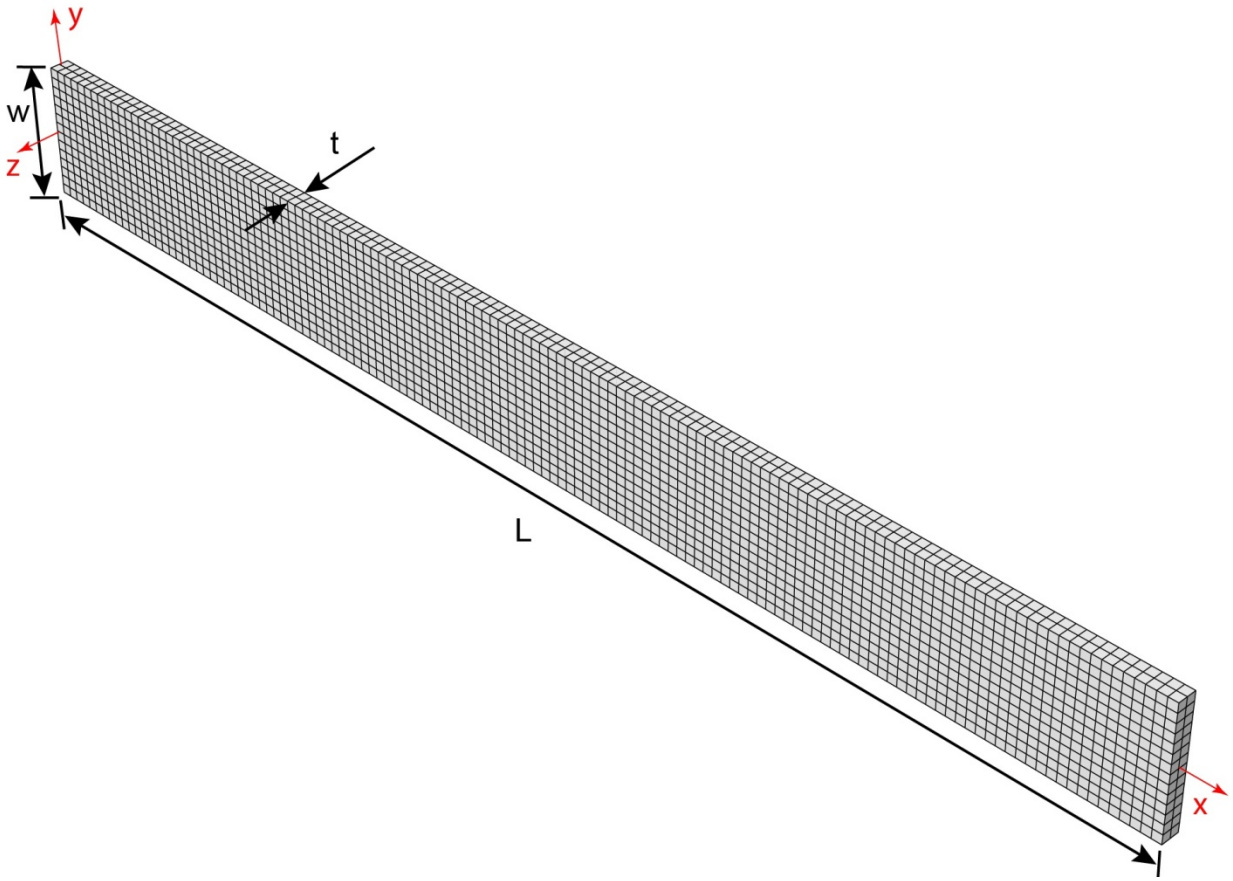

Fig. 2.10 Geometry and mesh of finite element method.

Fig. 2.11 Contours of equivalent plastic strain showing localization along both characteristics at both ends of the model.

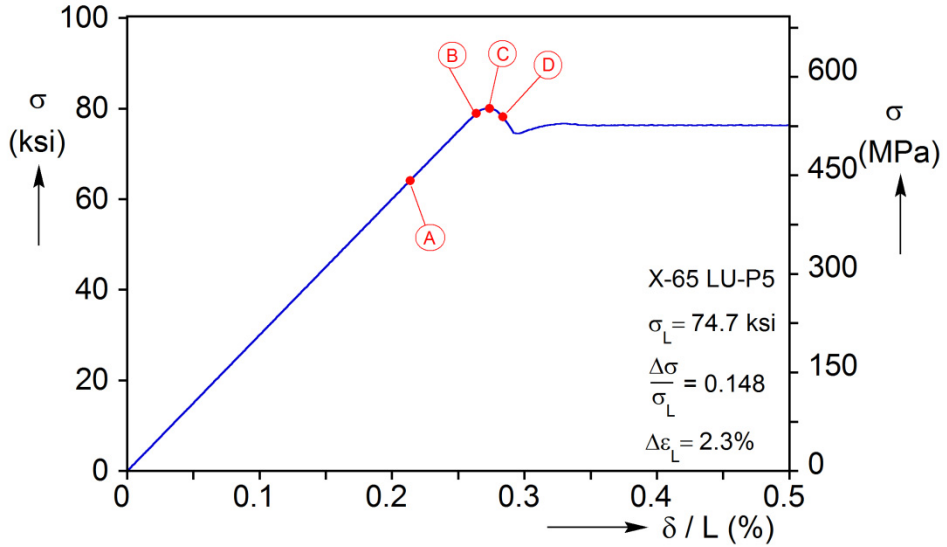

(a)

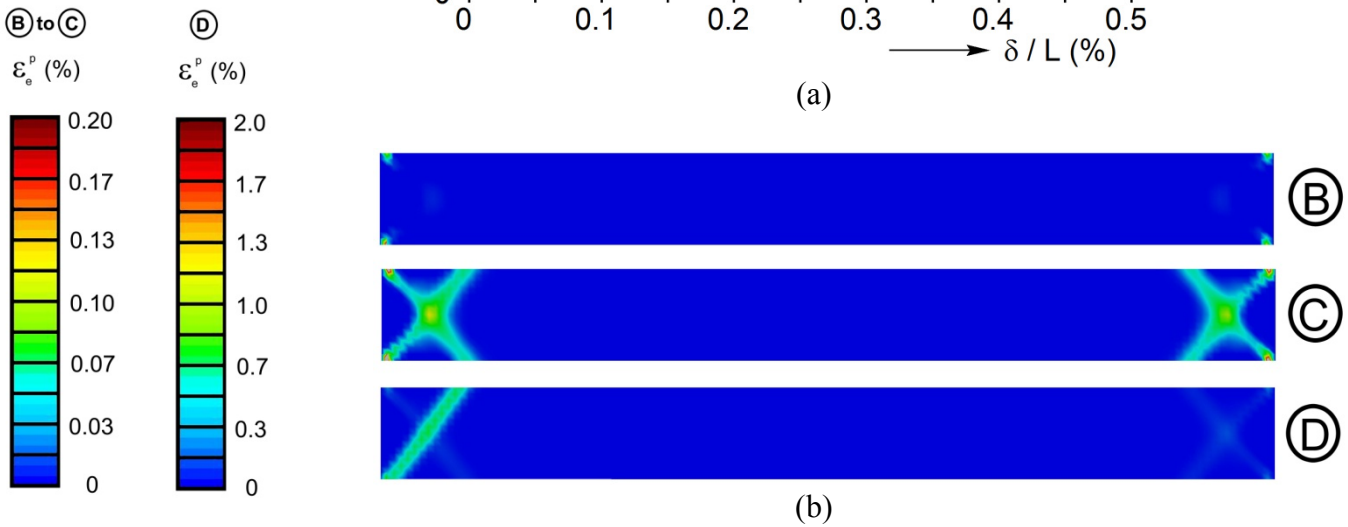

(b)

Fig. 2.12 Initiation of plastic deformation.

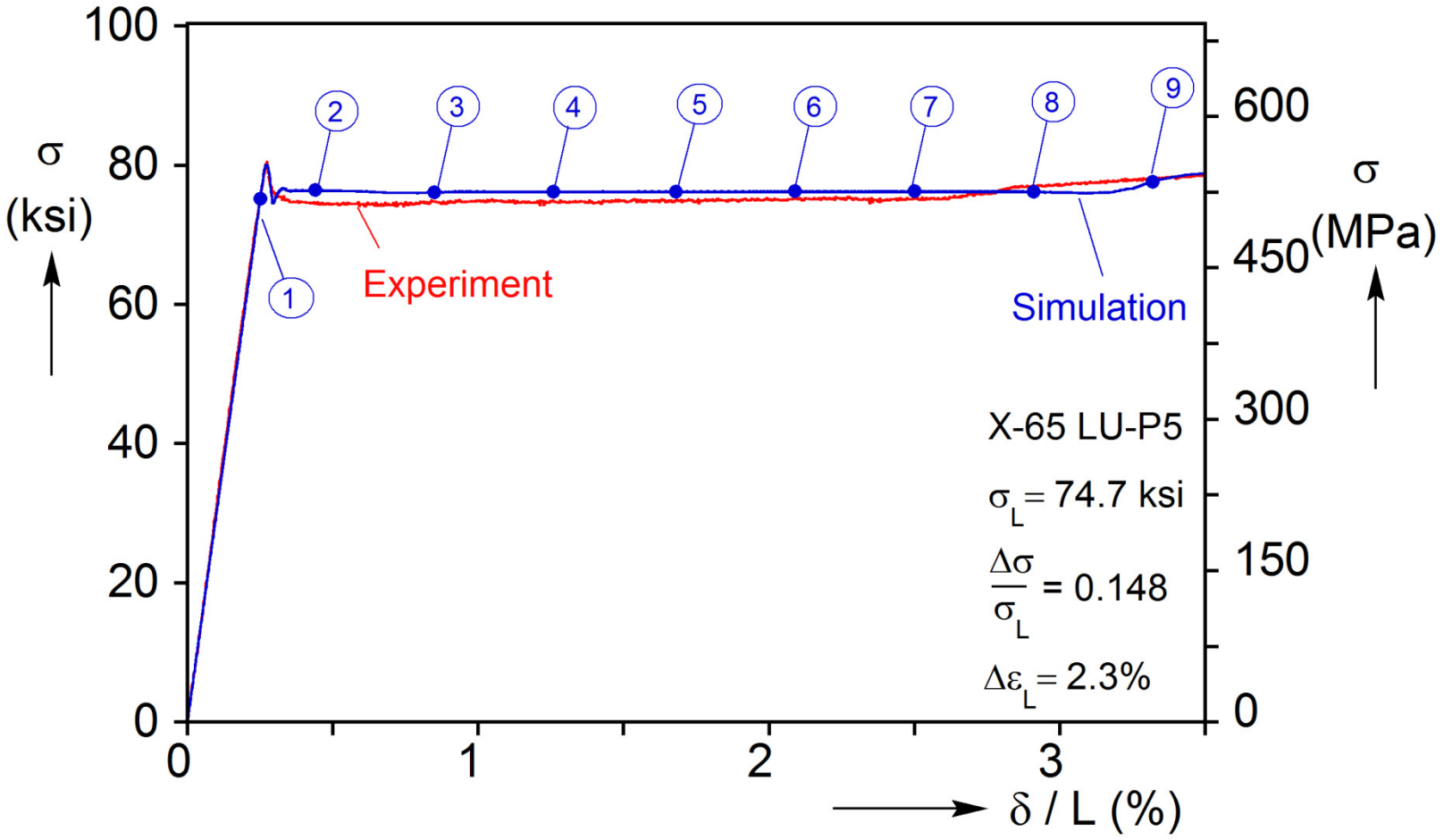

Fig. 2.13 Comparison of measured and calculated stress-elongation responses.

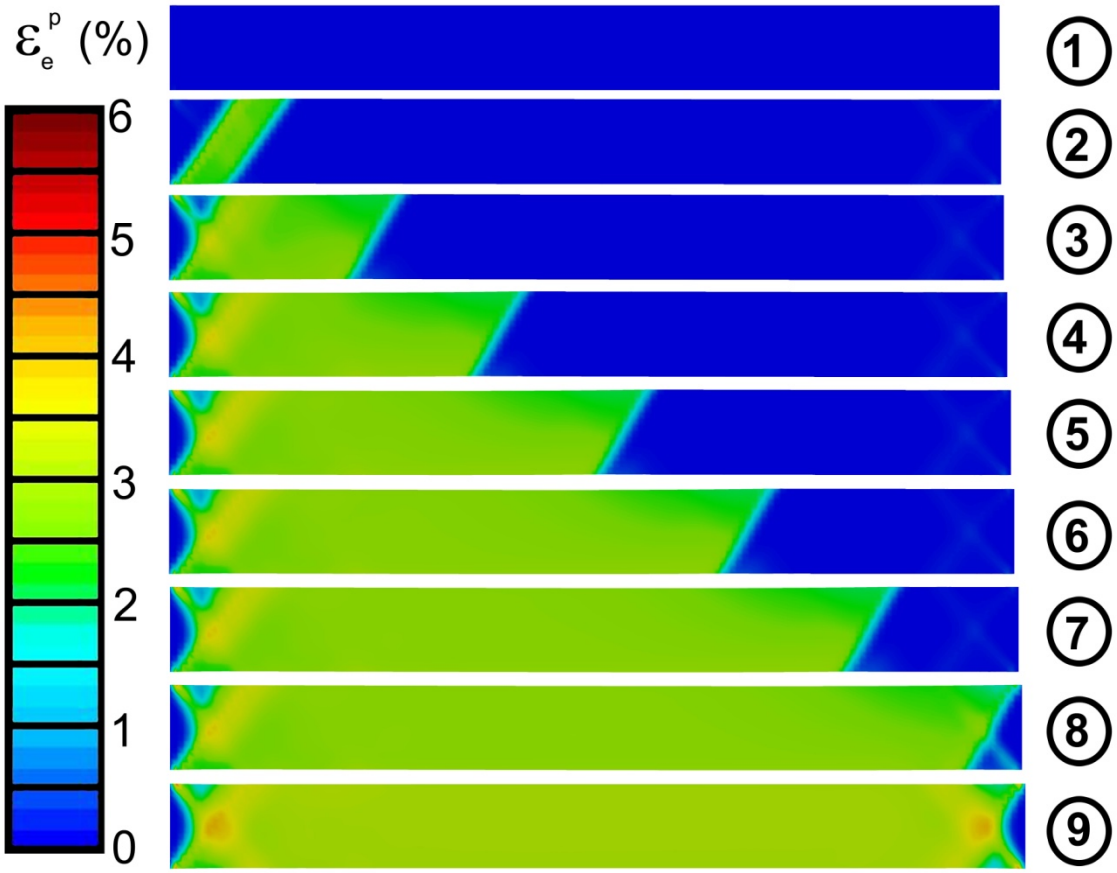

Fig. 2.14 Calculated deformed configurations corresponding to response in Fig. 2.13. Color keys represent equivalent plastic strain.

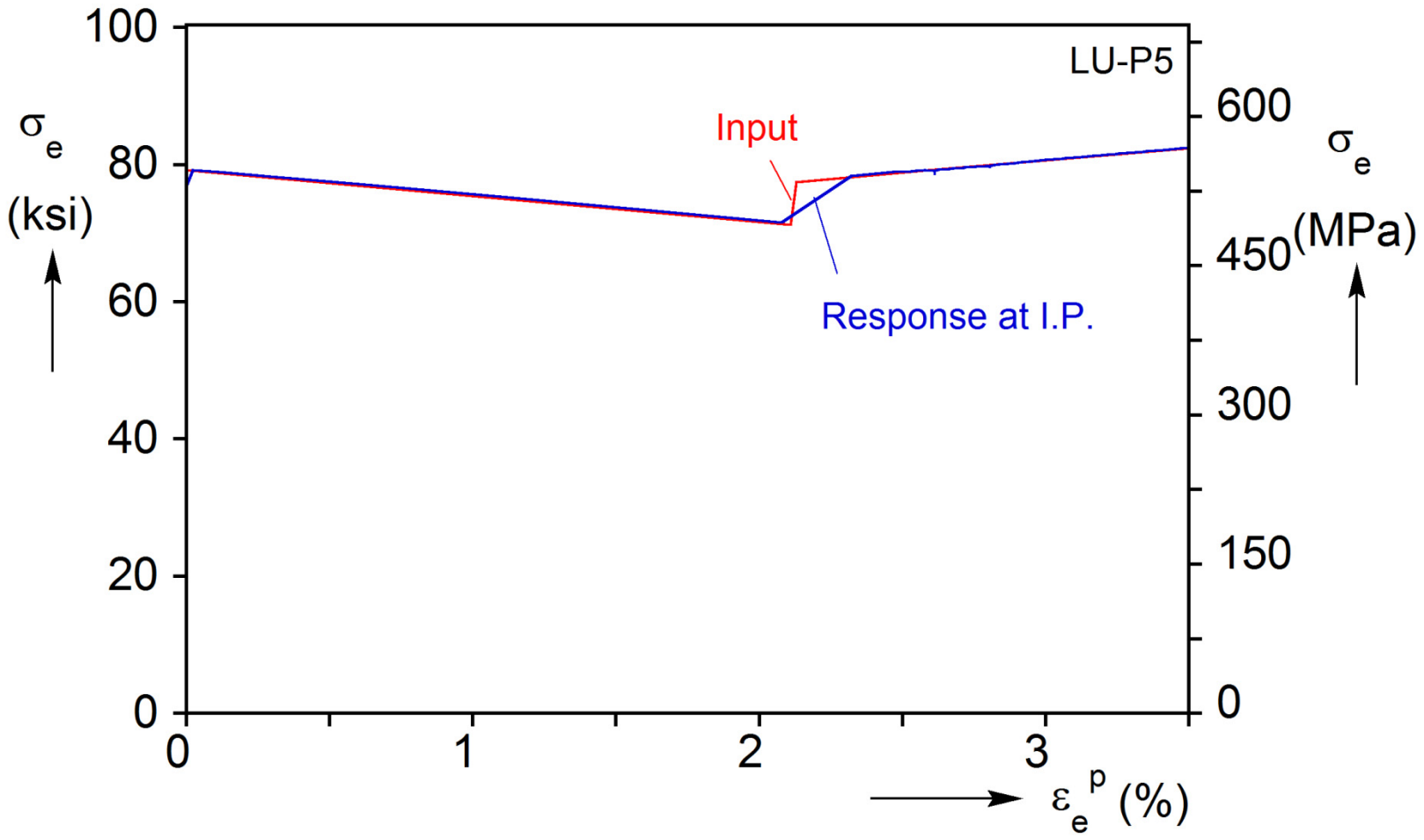

Fig. 2.15 True stress - equivalent plastic strain at an integration point of the FE model.

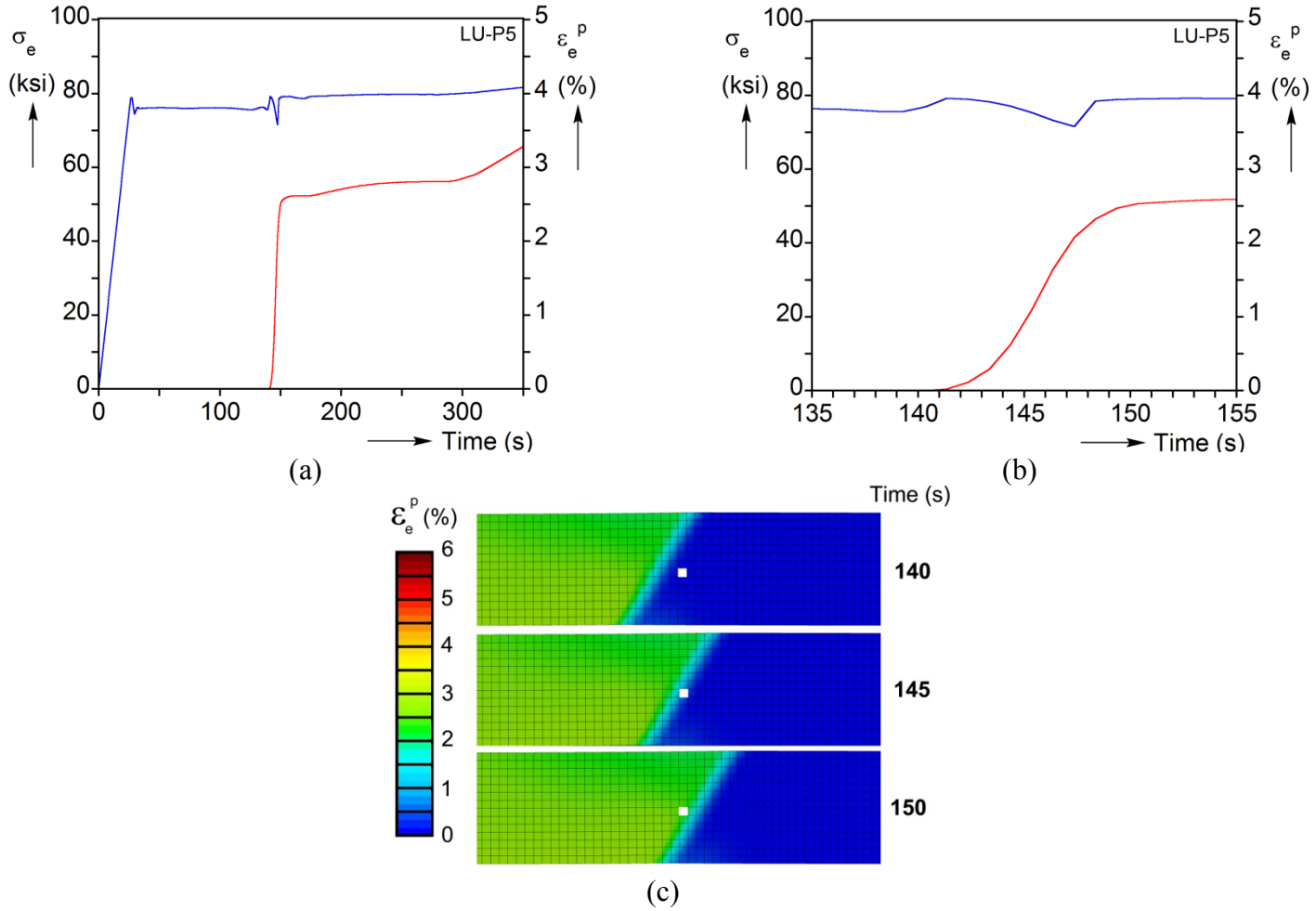

Fig. 2.16 History of true stress and equivalent plastic strain at an integration point. (a) history during propagation of the front along the specimen; (b) stress and strain when the front is passing the integration point and (c) contours of equivalent plastic strain showing the front passing the integration point (element in white).

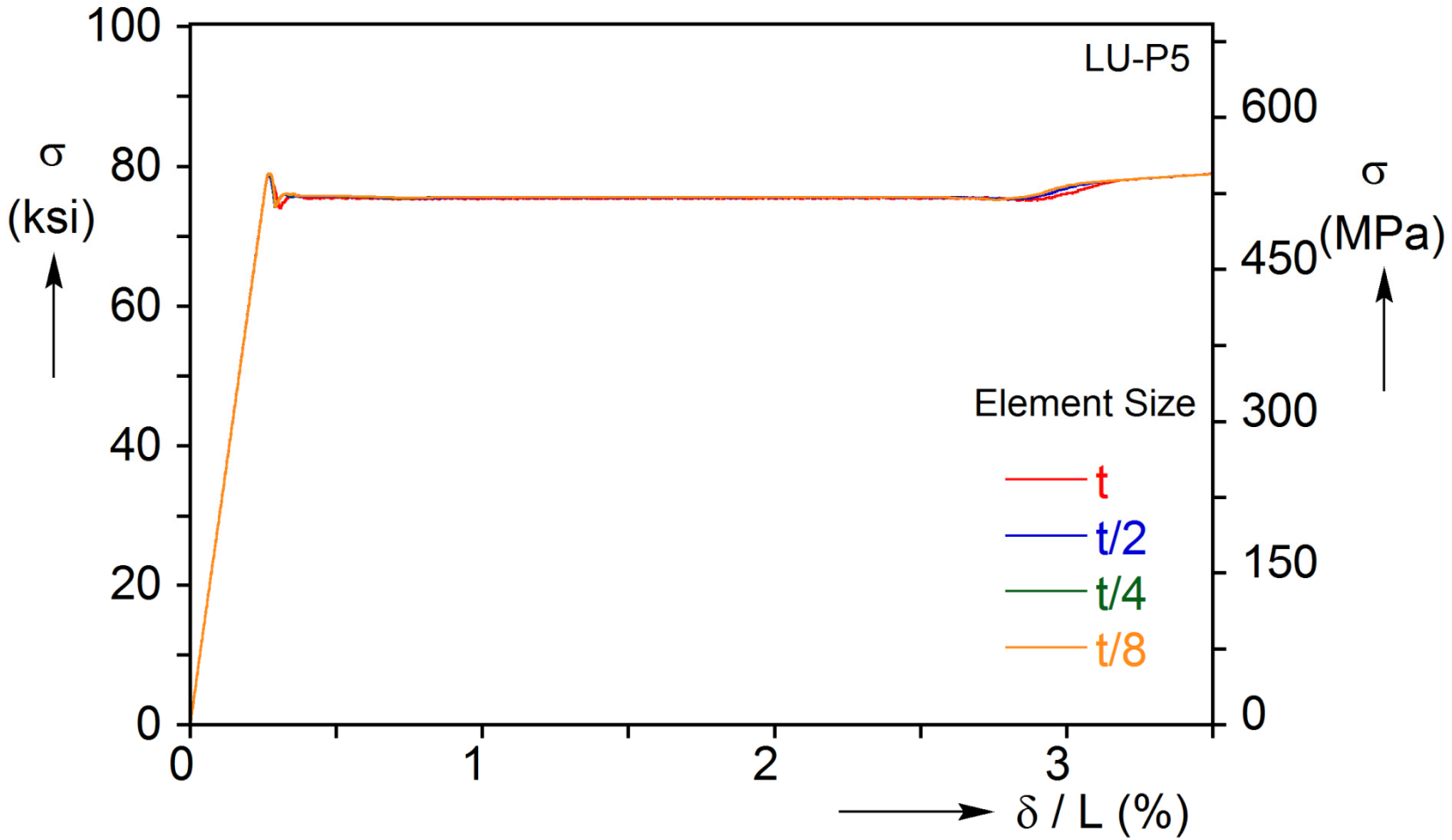

Fig. 2.17 Calculated stress-elongation responses for four mesh sizes.

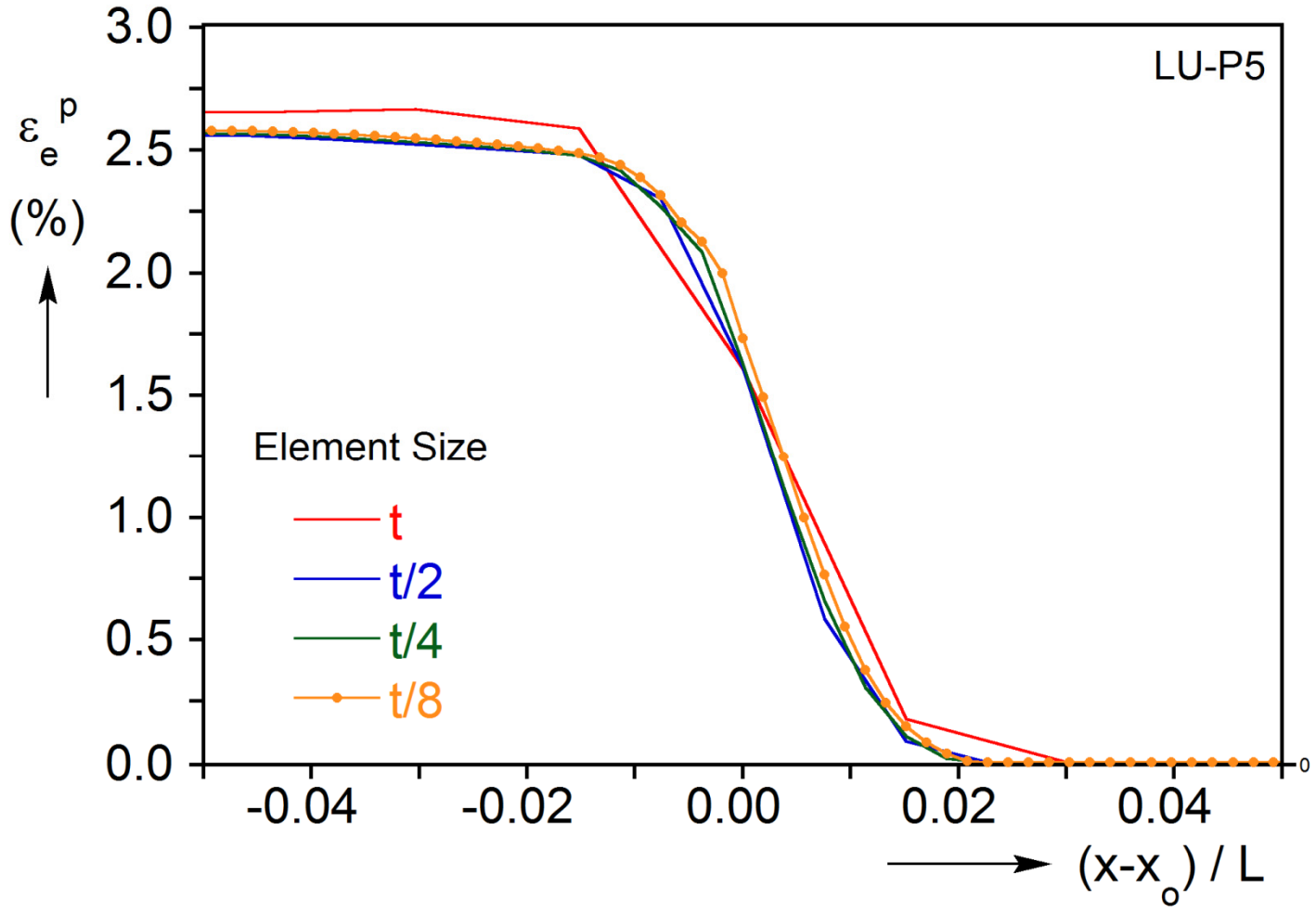

Fig. 2.18 Equivalent plastic strain at the interface of Lüders deformed and undeformed zones for four mesh sizes.

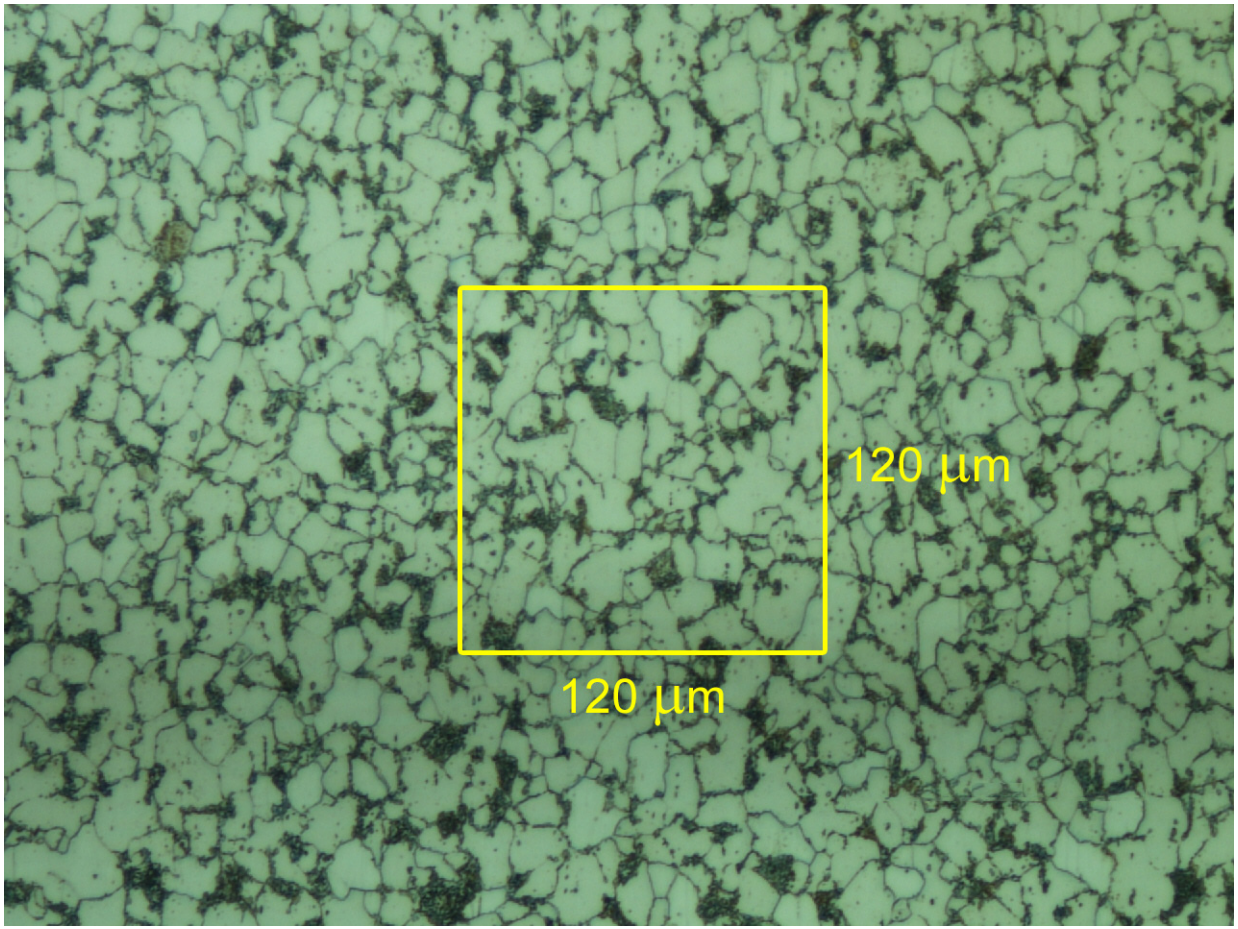

Fig. 2.19 Photomicrograph showing grain size of steel of tube used in Exp. LU11-5. Included for comparison is the outline of an element with size *t*/8.

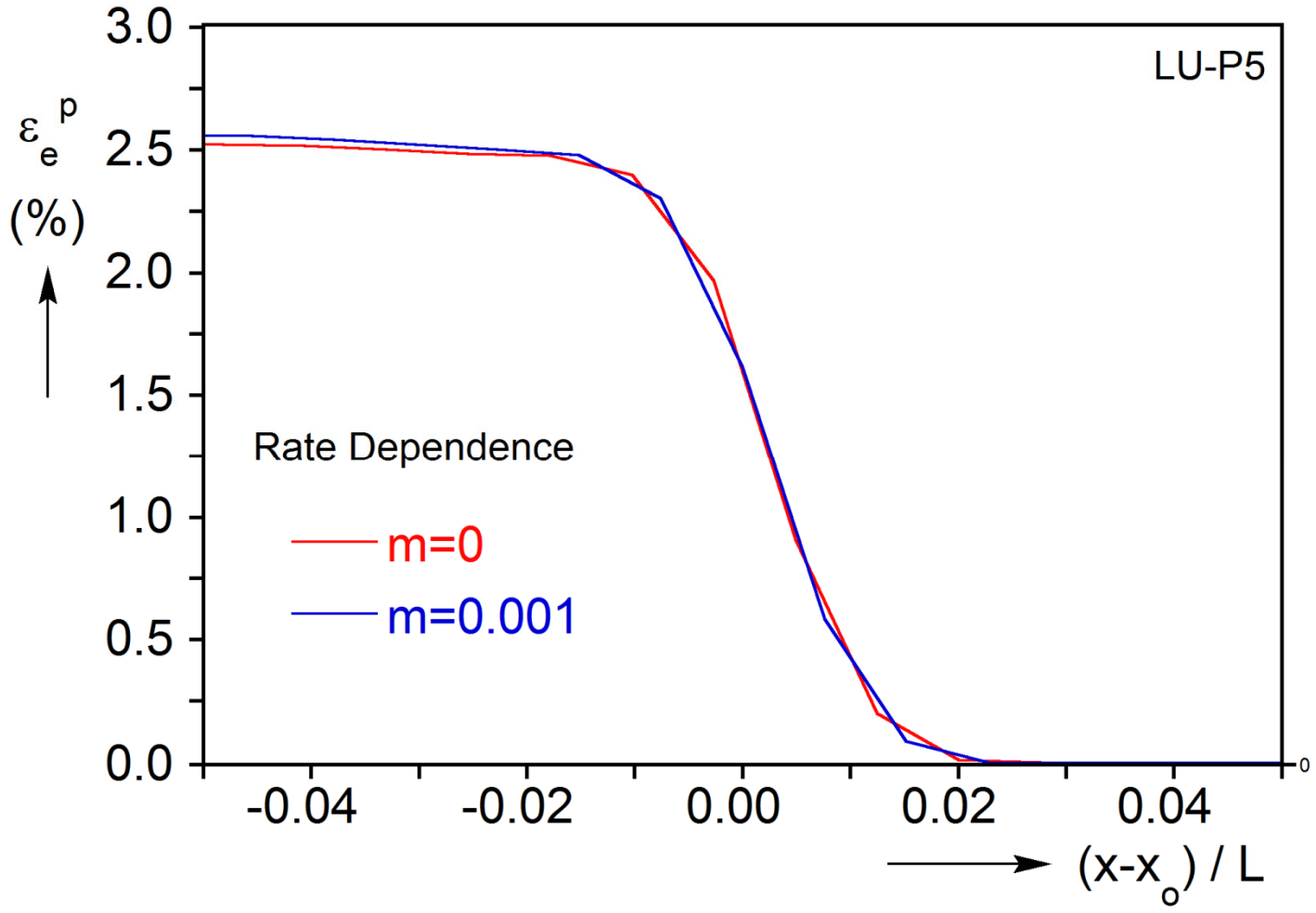

Fig. 2.20 Lüders front shape calculated with and without rate dependence.

Chapter 3: BENDING EXPERIMENTS

The effect of Lüders banding on the response of steel tubes under pure bending was investigated experimentally. In this chapter, the experimental facilities and procedures used are first described followed by the experimental results and main observations.

3.1 BENDING SPECIMENS

The experiments were carried out on low-carbon steel (CS) 1020 tubes with nominal diameters (D) of 1.25 and 1.375 in (32 and 35 mm) and D/t values in the range of 14.7 to 33.2. They were manufactured by electric-resistance welding (ERW) followed by DOM (drawn over mandrel process). In view of this cold forming process in the as-received state the materials have a monotonic stress-strain response. In order for the Lüders bands to reappear the tubes were thus heat-treated in a vacuum furnace (*Bodycote*, Houston, TX). The heat treatment consisted of heating the tubes to 1292^{o}F (700^{o}C) maintaining this temperature for 40 minutes and then quenching the tubes (see Figs. 3.1 and 3.2). This treatment also lowers the yield stress and increases ductility (see a typical stress-elongation response of heat treated tubes in Fig. 3.3). Following the heat treatment the tubes developed Lüders strains in the range of about 1.8% to 2.7% and yield (plateau) stresses in the range of 32-52 ksi (220-358 MPa).

Tensile tests were performed on 0.375×5.750 in (10×146 mm) longitudinal strips cut out of the heat-treated tubes during the course of this investigation. The tensile tests were conducted under displacement control at a strain rate of 10^{-4} s^{-1} (when deformation is uniform). In addition to the stress-elongation responses, full-field measurements were obtained using brittle coating and digital image correlation techniques. More details about these tests were presented in Chapter 2.

3.2 EXPERIMENTAL FACILITIES

3.2.1 Four Point Bending Machine

The heat-treated tubes were bent to collapse in the custom four-point bending facility shown in Fig. 3.4 (see Corona and Kyriakides, 1988; Kyriakides and Corona, 2007). The bending machine consists of two free-turning sprockets mounted on two stiff support beams. Heavy chains run around the sprockets and are connected to two actuators and in-line load cells to form a closed loop. Solid steel extension rods are closely fitted into each end of the tube and the assembly is mounted onto the bending machine. The solid rods engage smooth rollers housed in each sprocket assembly as shown in the figure. The machine is activated by simultaneously contracting one of the cylinders and extending the other, in the process rotating the sprockets and the solid rods. The roller arrangement allows an essentially four-point bending loading of the tube and the required inward translation of the rods. A "hard" machine is essential for testing structures beyond limit loads so the device was designed to be stiff relative to the test specimens.

The bending machine is operated by a closed-loop, servo-controlled system, shown schematically in Fig. 3.5, that can be run under either moment or rotation control (Corona and Kyriakides, 1991). The present experiments were run under rotation control at a rate that corresponds to a maximum bending strain rate of 10^{-4} s^{-1} (for uniform deformation).

The applied moment (M) is monitored by the in-line load cells shown in Fig. 3.4a, and rotary transducers (RVDTs) record the rotation of the sprockets (θ_α, α=1,2). While the deformation of the tube is uniform, its curvature can be obtained from

$$\kappa_{measured} = \frac{\theta_1 + \theta_2}{2L}. \tag{3.1}$$

where $2L$ is the effective length of the specimen. The transducer signals $\{M, \theta_1, \theta_2\}$ are monitored through a computer-operated data acquisition system.

The moment capacity of the bending machine is 15,000 lb-in (1,700 N-m) and the maximum combined rotation of the sprockets is 120 degrees, determined by the full stroke of the cylinders (10 in—254 mm).

3.2.2 Ovality and Wrinkle Measuring

The change in diameter was monitored during some experiments with lightweight transducers riding on the deforming tube. Such transducers (see Fig. 3.6a) consist of a lightly spring loaded slide that engages the tube with knife-edges and measures continuously the diameter (Kyriakides and Corona, 2007).

A high resolution scanning transducer, shown in Fig. 3.6b, was used to measure the axial profiles of wrinkles after the experiments (see Kyriakides and Corona, 2007).

3.2.3 Video Recording

The global deformation of the deforming tube was monitored and recorded using a high-resolution color digital video camera (Sony XCD-U100CR). The camera employs the IEEE 1394.b interface, which attains data-transfer rates of up to 800 MB/s. The experiments were recorded at 2 frames/s in 1600×1200 pixels (UXGA).

3.2.4 Brittle Coating

A brittle coating, *Stresscoat* SK-80F, was used in the present study to make observations of the initiation and evolution of Lüders bands in several tube bending experiments. A thin layer of brittle coating (~0.004 in - 100 μm) sprayed on the tubes before the test was cured at about 120 ^{o}F (49 ^{o}C) for 24 hrs. After it is cured, the coating

is a brittle ceramic that shatters when strained sufficiently either in tension or compression (~±1% strain) thus mapping localization bands on the surface of the tube.

3.3 Experimental Procedures

For each tube *D/t* family, several 36 in (0.9 m) long specimens were cut from 20 ft long (6 m) mother tubes and sent for heat-treatment. A section about 8 in (200 mm) long was removed from each heat-treated tube from which narrow axial strips were extracted. Such strips were tested in tension, recording the stress-strain response of the material up to failure. The remainder of each tube was used in the bending experiment usually resulting in a 15*D* long test section (note that part of the specimen length engages the solid rod inserts).

Before bending measurements of the geometry of each tube were made. Several diameter measurements were taken at 4.0 in (100 mm) intervals along the length of the tube and the average value of the measurements is listed under *D* in Table 3.1, while Δ_o represents the initial ovality. The wall thickness was measured at the two ends, and *t* in Table 3.1 represents the average value for each tube. It is noteworthy that because of the manufacturing process used for this class of tubes, the wall thickness was consistently uniform around the circumference.

The data and video acquisition systems were then prepared and an initial reading was taken as reference. Subsequently, the test specimen was fitted with the solid rod extensions and mounted on to the bending device. The tube was bent until localized collapse initiated. Because of the relatively large rotations that are required to take most of the tubes to collapse, the weight of the rods and friction in the rollers had to be taken into account. The process for correcting the moment-rotation data measured is described in Appendix A.

3.4 Experimental Results

Several bending experiments were conducted for each of five tube *D/t* values in the range of 14.7-33.2. Here, for brevity, results from eight representative tests, at least one from each *D/t* considered, will be discussed. The main geometric and material parameters of the eight specimens are listed in Table 3.1.

3.4.1 Bending of a Tube with a Monotonic Stress-Strain Response

Figure 3.7 shows a typical moment-curvature response of a tube that has a monotonic stress-strain curve (see LU3-0 in Fig. 3.3). The response exhibits a linearly elastic regime, which gradually becomes nonlinear initially because of the induced ovalization and later due to material nonlinearity. The increasing ovalization gradually reduces the bending rigidity and eventually a limit moment is attained (identified with a caret "^"). The tube has uniform curvature up to the limit load. Beyond this point, it develops initially a diffuse localized ovalization that extends over a length of few diameters, which subsequently sharpens into local inward kink.

3.4.2 Bending of Tubes with Lüders Bands

a. D/t = 24.3, $\Delta\varepsilon_L$ = 1.89%

The main features of the bending experiments of tubes with Lüders bands will be discussed by comparing results from two experiments on tubes of the same *D*/*t* = 24.3: LU9-1 and LU3-3. Their stress-strain responses, shown in Fig. 3.8, have the same elastic modulus (E), plateau stress (σ_L) and hardening behavior but have different Lüders strains ($\Delta\varepsilon_L$): LU9-1 has $\Delta\varepsilon_L = 1.89\%$ while LU3-3 has $\Delta\varepsilon_L = 2.55\%$ (see Table 3.1). Figure 3.9 shows the measured moment vs. the average of the two rotations recorded by the RVDTs, $\bar{\theta}_L$, for LU9-1. (We note that, when the tube deformation is uniform the curvature of the tube is given by $\kappa = \bar{\theta}_L / L$). The moment is normalized by the fully

plastic moment ($M_o = \sigma_L D_o{}^2 t$, $D_o = D - t$) and the average rotation by $Lt/D_o{}^2$ ($\equiv L\kappa_1$). Figure 3.10 shows a set of nine full-span deformed configuration of the tube that correspond to the locations marked on the response with numbered solid bullets.

The overall behavior is very similar to that described in Kyriakides et al. (2008) for a thicker tube. The moment-rotation response exhibits an initial stiff and linear behavior corresponding to the linearly elastic regime of the material. The tube bends uniformly, as confirmed by configuration ① in Fig. 3.10, approximately with the elastic bending rigidity of the tube (*EI*). The moment attains a local maximum of $M = 1.04 M_o$ and then drops sharply down to a value that is close to M_o, where it starts to trace a somewhat ragged moment plateau. The moment plateau and its level are equivalent to the Lüders stress plateau in the uniaxial tension test. Indeed, as is often observed during the initiation of Lüders banding in a uniaxial test, some nonlinearity in the moment-rotation response is seen to occur just prior to the moment maximum, indicating that a limited amount of Lüders banding has already initiated. Most probably, this takes place adjacent to the ends of the solid rod inserts where some stress concentrations are unavoidably present. The moment drop is a definite sign that an instability has initiated. As we will see in the next section, Lüders deformation nucleates in the form of bands that are inclined to the axis of the tube on the top and bottom surfaces (see also Aguirre et al., 2004). The more macroscopic effect of the nucleation of the bands is the localization of curvature initially in a zone approximately 2*D* long; in other words, a zone that is bent to a higher curvature than the rest of the structure. In the present experiment, this first occurred at the two ends of the tube close to the interface with the solid rod inserts (that penetrate 3.2*D* into the tube) as illustrated by configuration ②. As $\bar{\theta}_L$ increases, zones of higher curvature spread inwards, first from the RHS (see ③) but subsequently from the LHS also (see ④ and ⑤). So in configuration ④ the two zones of higher curvature

become apparent with the middle section of the tube having a visibly smaller curvature (approximately M_o/EI). In configuration ⑤ the two zones of higher curvature have propagated towards the center. The gradual spreading of the two higher curvature zones continues in configuration ⑥. Their growth is not necessarily continuous but instead one side propagates some distance and stops, then the other side propagates and so on. This starting, stopping and restarting of propagation is responsible for most of the jaggedness of the moment plateau as each restart involves re-initiation of the Lüders banding. By configuration ⑦, the higher curvature has spread to essentially the whole tube. The end of the stress plateau is characterized by a small dip in the moment, which is associated with the meeting of the two propagating fronts of Lüders deformation. Such "load" troughs are commonly observed at the termination of "load" plateaus in other systems that experience propagating instabilities (e.g., see Shaw and Kyriakides, 1997; and Kyriakides and Miller, 2000, for tension tests on NiTi and steel strips respectively).

It is interesting to note that the curvature at the termination of the plateau approximately corresponds to the curvature of the localization induced by Lüders banding. The end of the plateau occurred at a curvature of $\kappa = 1.44\kappa_1$. This corresponds to a maximum bending strain of 3.22% in the outermost fibers of the tube. By contrast, the end of the Lüders stress plateau in the uniaxial tension test occurred at a strain of 1.89%. This difference indicates that for bending localization triggered by the Lüders deformation to take place, more than just the fibers furthest from the neutral axis of the tube must be involved.

Subsequent to the last moment dip, the moment increases monotonically and the curvature of the tube grows uniformly as seen in configuration ⑧, signs that a significant part of the material has now entered the stable, monotonically increasing part of the stress-strain response. Throughout this bending history, the tube cross section has been

ovalizing locally during the moment plateau and subsequently uniformly (see results for LU10-2 that follow). Thus, at some point during the uniform bending phase further increase in the moment becomes impossible, and a limit moment is reached at a value of $M = 1.09M_o$ and a curvature of $\kappa = 1.85\kappa_1$ (marked in Fig. 3.9 with a caret "^"). Beyond this point, localized diffuse ovalization develops about four diameters from the RHS end of the tube (see configuration ⑨). In other words, the structure is collapsing and the test is terminated. The tube behavior during this part of the response is similar in most respects to that seen during the bending of tubes with a monotonically increasing material response like that shown in Fig. 3.7 (see also Kyriakides and Ju, 1992, and Ch. 8 in Kyriakides and Corona, 2007).

In the way of highlighting the inhomogeneous deformation that develops during the moment plateau, several of the video images were used to quantify its extent. To this end, deformed tube images like the ones in Fig. 3.10 (1600×1200 pixels) are first converted into grayscale and then using an edge detection program, developed in MATLAB, the edges are located and then smoothened producing results like those in Figs. 3.11a and 3.12a that correspond to configurations ⑤ and ⑦ in Fig. 3.10. The slope $\theta(s)$ of each edge is then calculated and once again smoothened. Figures 3.11b and 3.12b show the mean of the two $\theta(s)$ loci calculated from each configuration as a function of the natural coordinate s. Since the local curvature of the tube is $\kappa = d\theta/ds$, a linear $\theta(s)$ trajectory represents a uniformly bent tube, as indeed is the case for configuration ⑦ in Fig. 3.12b. By contrast, $\theta(s)$ in Fig. 3.11b is essentially trilinear with a central section with a low slope and two outer sections with a common higher slope. In this configuration, the relatively undeformed portion covers approximately one-third of the tube test section. It is important to note that the smaller slope corresponds to a curvature of $\kappa = 0.10\kappa_1$, a value that is close to that of the first moment maximum. By contrast, the

larger slope corresponds to $\kappa = 1.36\kappa_1$, a value that is approximately equal to the curvature at the end of the moment plateau. By configuration ⑦, essentially all of the test section has been deformed to this value reflected in the nearly linear $\theta(s)$ trajectory in Fig. 3.12b. Clearly, this scheme, although laborious, can be used to monitor quantitatively the evolution of inhomogeneous bending in such experiments.

b. Ovalization of Tube Cross Section

As is well known, bending induces ovalization to the cross section of a tube, a nonlinearity that tends to reduce its bending rigidity and can lead to a limit load instability. It is thus worth examining how ovality evolves in tubes that experience Lüders bands induced localized bending of the type described in the previous section. To this end, separate experiments were conducted on tubes with Lüders bands in which the change in diameter in the plane of bending was monitored at two locations along their length. Results from one of these experiments, LU10-2, from a tube with similar geometric and material parameters as those of LU9-1, will be used to demonstrate the evolution of ovalization (main problem parameters listed in Table 3.1). Figure 3.13a shows the recorded moment – end-rotation response, which is very similar to the one of LU9-1 in Fig. 3.9. Figure 3.13b shows the change in diameter ($\Delta D/D$) as a function of the end-rotation at points A and B located at the axial positions marked in the schematic of the tube included as an inset. The change in diameter was monitored with lightweight transducers like the one in Fig. 3.6a, riding on the deforming tube.

The evolution of deformation in this tube was in most respects similar to that of LU9-1. As the moment plateau is traversed, localized curvature develops close to the two ends approximately in the same manner as shown in Fig. 3.10. Simultaneously, the central section of the tube remains essentially at the curvature that corresponds to the first

moment maximum ($\bar{\theta}_L / L\kappa_1 \approx 0.1$). During the initial homogeneous phase of bending (I), the tube deforms uniformly and the two transducers record the same change in diameter (too small for the scale of Fig. 3.13b). As the end-rotation increases, the zones of larger curvature propagate inwards. After the first moment maximum, transducer A in the neighborhood of the localizing zone on the RHS experiences the higher curvature early in the bending history and ΔD is seen to increase between $\bar{\theta}_L / L\kappa_1$ of 0.4 and 0.8. Subsequently, the local ovality stays nearly constant until the end of the moment plateau is reached at $\bar{\theta}_L / L\kappa_1 \approx 1.5$. By contrast, during most of this bending history transducer B near the mid-span records essentially no change in ΔD. The ovality at this location only starts to grow for $\bar{\theta}_L / L\kappa_1 > 1.2$ as the larger curvature regime approaches it (note that the transition between the two deformation regimes is about D long). By the end of the moment plateau, ΔD at B has increased to the same level as that of location A.

During the subsequent uniform bending phase (III) the two transducers record very similar values of ΔD. Following the moment maximum at $\bar{\theta}_L / L\kappa_1 = 1.9$, deformation localizes once more, this time close to the end of the tube on the RHS. Consequently, site A experiences an acceleration in the growth of ΔD while at site B it stops growing registering a small decrease in ΔD because of the dropping moment (see similar results at the end of a bending test on a hardening material tube in Fig. 2.20b of Kyriakides and Ju, 1992). Marked with vertical dashed lines in Fig. 3.13b are the boundaries of the four regimes of behavior. Regimes I and III represent homogenous deformation and II and IV inhomogeneous. In summary then, the inhomogeneous bending that results from Lüders banding induces in turn inhomogeneous ovalization. The ovality is larger in Lüders deformed sites and smaller in unaffected ones.

c. D/t = 24.3, $\Delta\varepsilon_L$ = 2.55%

Turning now to results from Exp. LU3-3, its geometric and material characteristics are essentially the same except that the material exhibits a longer Lüders plateau of $\Delta\varepsilon_L = 2.55\%$. The measured moment-end rotation response is shown in Fig. 3.14 and a set of full-span deformed configurations corresponding to it in Fig. 3.15. Initially, the response and deformation are similar to those in Figs. 3.9 and 3.10: the tube bends uniformly in the elastic range (configuration ①); a local maximum of $M = 1.09M_o$ is attained, followed by a ragged plateau at a level of nearly M_o. Lüders banding nucleates essentially simultaneously at the two sites adjacent to the solid rod inserts; this leads to localization of curvature at these sites that can be seen in configuration ②. As the end-rotation continues to increase, the two higher curvature zones propagate inwards, as evidenced in images ③ to ⑥. By configuration ⑦, the growth of the higher curvature zones appears to start to give way to an increase of the ovalization at the RHS site. This local reduction in bending rigidity causes an initially gradual drop in the moment, which after configuration ⑧ becomes more precipitous. The tube now clearly is collapsing at this site by diffuse ovalization that extends over a section approximately 5*D* long. This has occurred even though more than half of the tube remains in the lower curvature regime. Further rotation causes the localization to sharpen into a local kink. To avoid further damage the test was terminated, the structure was unloaded, and the specimen removed from the bending machine. The onset of collapse, designated in Table 3.1 as $\bar{\theta}_{CO}/L\kappa_1$, is at 1.56.

Figure 3.16a shows configuration ⑥ with its edges marked and Fig. 3.16b shows the calculated slope $\theta(s)$. The trilinear nature of $\theta(s)$ is a quantitative verification of the coexistence of two curvatures. Once again the central portion has a curvature that corresponds to the beginning of the plateau ($\kappa = 0.12\kappa_1$). By contrast, the curvature at

the two ends is approximately $\kappa = 1.95\kappa_1$, a value that does not appear in Fig. 3.14 because it could not be sustained for longer domains than the ones seen in image ⑥.

A photograph of the specimen following unloading is shown in Fig. 3.17. Indicated with arrows are the edges of the test section. Also visible is a section of about 5*D* long that experienced the severe local ovalization associated with the collapse of the structure. Interestingly, the central lower curvature section has sprung back to a nearly straight configuration. This is the case for a section of about 3*D* long at its center while sections further out have a very small curvature indicating that they had experienced a small amount of plastic deformation. Clearly, in this case, the higher Lüders strain made the structure less stable. It appears that the higher curvature induced by Lüders banding could not be sustained by the whole structure. Accordingly, when a critical length of the tube was deformed to the corresponding curvature, it collapsed. Undoubtedly, this is an undesirable consequence of the larger Lüders strain that limits the performance of the structure and must be understood.

3.4.3 Summary of Results of Additional Experiments

Results from five additional experiments with *D/t* ratios in the range of 14.7 to 33.2 will now be briefly outlined concentrating on similarities and differences from the two cases presented in Section 3.4.2. The main geometric and material parameters of the tubes are summarized in Table 3.1. The stress-strain responses of the five tubes appear in Fig. 3.18 where they are identified by the LUx-y experiment number listed in Table 3.1. All responses exhibit Lüders stress plateaus of different levels and different extents (respectively listed under σ_L and $\Delta\varepsilon_L$ in the Table). However, the five responses have very similar hardening. The moment-end rotation responses of the five new cases appear in Fig. 3.19. Each response is identified by the tube *D/t* and the extent of the Lüders

strain, $\Delta\varepsilon_L$ in %; thus for example, the response of LU4-3 is depicted as 18.8:1.8. Each of these experiments was repeated at least twice more and found to be repeatable, with the exception of the thinner ones where initial geometric imperfections can influence collapse.

All tubes exhibit a linearly elastic regime that terminates when localization commences at the first moment maximum. The normalization adopted does not capture differences in the elastic bending rigidity and thus the different initial slopes. All cases developed moment plateaus at the level of about M_o during which Lüders banding and localized bending of the type reported in Figs. 3.10 and 3.15 took place. For two cases, 14.7:2.4 (LU7-3) and 18.8:1.8 (LU4-3), the plateaus are fully developed, the tubes then enter the hardening regime, and eventually collapse by localized diffuse ovalization. In other words, similar to LU9-1 (see Figs. 3.9 and 3.10) and LU10-2 (Fig. 3.13a) these tubes survived the inhomogeneous bending phase and returned to uniform stable bending. Subsequently, they collapsed following the natural limit moment instability induced by ovalization (marked by "^" on these responses). The normalized curvatures at the limit moments, κ_L/κ_1, listed in Table 3.1 are numerically similar for the four cases. However, the curvature (κ_L) and the maximum bending strain (ε_{bL}) are different; they increase significantly as the *D/t* decreases as illustrated in Fig. 3.20a that shows three of these specimens.

The responses of the remaining three specimens 33.2:2.2 (LU11-1), 26.8:2.2 (LU12-1), and 18.6:2.7 (LU5-3) were terminated by local structural instabilities that occurred during the inhomogeneous bending deformation phase (i.e., similar to LU3-3). For the higher *D/t* tubes like LU11-1, initially pockets of wrinkles appeared along the whole length of the tube. Deformation localized at one end and spread over a very short length of the specimen. This caused the amplitude of wrinkles in this zone to grow

quickly with one of them localizing resulting in collapse (see Fig. 3.21a). This pocket of wrinkles and the localization of one of them are captured in the photograph shown in Fig. 3.21b. The length of the specimen that sustains the larger curvature depends on the Lüders strain and the *D/t*. Thus, for the high *D/t* specimen in Fig. 3.21a it is quite small. The four specimens that collapsed before reaching homogeneous deformation are shown together in Fig. 3.20b. The critical Lüders deformed length is seen to increase as the *D/t* decreases. By contrast, the sections unaffected by Lüders banding are seen to remain essentially straight and circular.

As mentioned earlier, the response of tubes with higher D/ts can also be influenced by small initial geometric imperfection. The effect of imperfections is illustrated in Fig. 3.22 that shows moment-rotation responses from three tubes that originated from the same mother tube, LU12. The otherwise identical tubes collapse at different rotation levels, presumably because of small differences in initial imperfections.

3.4.4 Visualization of Lüders Bands in Bent Tubes

A number of separate experiments were performed on tubes of two different *D/t* values aimed to capture the onset and evolution of Lüders bands using specimens coated with the brittle coating *Stresscoat*. The following summarizes the observations made from this effort. The brittle coating shatters when it is strained to a value of about ±1.0%. Thus, immediately after the first moment drop, narrow bands of shattered coating inclined at $\pm\alpha$ to the axis of the tube show up on both the compressed and tensioned sides of the specimen at the site where Lüders banding initiates. As mentioned above, for higher *D/t* tubes pockets of wrinkles initiate early in the bending history. As Aguirre et al. (2004) showed, pockets of Lüders bands tend to initiate at peaks of such wrinkles. Figure 3.23a shows several clusters of Lüders bands that initiated in a tube with *D/t* = 33.1 while

Fig. 3.23b shows a close-up of one of the pockets (geometry and material properties similar to those of LU11-1). Initially, the bands are a fraction of a millimeter wide (~0.5 mm), make angles that range between ±(45-55)^{o} with the axis of the tube and cover about 120^{o} sectors. We note that the shattering of the *Stresscoat* is sensitive to its thickness. Since the coating was applied by manual spraying, its thickness varied to some degree and this is probably responsible for partial development of some of the bands in the two images. It is not clear if this band width is influenced by the shattering mechanism of the coating. This issue requires further investigation.

In this experiment, localized bending developed close to one end of the specimen and consequently Lüders banding concentrated at this site. New bands appeared here while the width of the initial bands grew covering a zone that was about 2*D* long. As this zone spread, inclined bands initiated at both of its ends. As was the case for LU11-1, the high curvature could not be sustained over a long span and the tube collapsed in a similar manner to that shown in Fig. 3.21. One of the edges of the high curvature zone can be seen in the upper ends of both images in Fig. 3.23.

3.4.5 Bending Induced Wrinkling

All tubes tested developed wrinkles. For the higher *D/t* cases, the wrinkles were more pronounced while for the lower values less so and appeared mainly in the localization sites. The wavelengths of these wrinkles were measured usually at the termination of the test. Figure 3.24 shows a histogram of the half wavelengths λ measured for the five tube *D/t* families tested (normalized by $\sqrt{Dt}$). The wavelengths are in the range of $0.4 < \lambda/\sqrt{Dt} < 2.0$, which is very similar to corresponding results reported in Aguirre et al. (2004) for tubes with *D/t* = 27.2. This wide spread in the wavelengths recorded is at variance with similar measurements performed in bending

experiments on tubes with monotonically increasing stress-strain responses where the scatter is only of the order of a few percent (e.g., see Fig. 5 in Ju and Kyriakides (1992) and Fig. 1 in Corona et al. (2006)). The large scatter in the present measurements may be related to the fact that at the time of the initiation of the wrinkles the material did not have a characteristic modulus. Included in the figure is the wavelength of axisymmetric elastic buckling modes under axial compression, which is independent of the modulus and is given by

$$\lambda_e = \frac{\pi\sqrt{D_o t}}{\left[48\left(1-\nu^2\right)\right]^{\frac{1}{4}}}. \tag{3.2}$$

Interestingly, λ_e falls close to the most commonly occurring wavelengths. (Note that λ_e does not differ significantly from the corresponding half wavelength of elastic wrinkles formed under bending—see Fig. 6 in Ju and Kyriakides, 1992). In view of this trend and lacking a better alternative, the tubes analyzed in the next chapters will be assigned axisymmetric initial imperfections with wavelengths λ_e.

Exp. No.	D in (mm)	t in (mm)	$\frac{D}{t}$	Δ_o (%)	$\frac{2L}{D}$	σ_L ksi (MPa)	$\Delta\varepsilon_L$ %	$\frac{\kappa_L}{\kappa_1}$	ε_{bL} %	$\frac{\bar{\theta}_{CO}}{L\kappa_1}$
LU11-1	1.255 (31.88)	0.0378 (0.961)	33.19	0.04	14.9	51.98 (358.5)	2.16	-	-	0.78
LU12-1	1.378 (35.01)	0.0516 (1.310)	26.72	0.05	15.0	38.47 (265.3)	2.21	-	-	1.16
LU3-3	1.253 (31.83)	0.0517 (1.312)	24.26	0.02	15.1	37.28 (257.1)	2.55	-	-	1.56
LU9-1	1.254 (31.85)	0.0516 (1.311)	24.31	0.05	14.9	36.91 (254.5)	1.89	1.851	4.14	-
LU10-2	1.254 (31.84)	0.0509 (1.293)	24.62	0.06	17.5	40.19 (277.2)	1.90	1.880	4.15	-
LU5-3	1.252 (31.81)	0.0674 (1.711)	18.59	0.02	14.9	42.91 (295.9)	2.71	-	-	1.65
LU4-3	1.252 (31.80)	0.0666 (1.692)	18.80	0.02	15.0	31.85 (219.6)	1.78	1.992	5.91	-
LU7-3	1.252 (31.80)	0.0853 (2.166)	14.68	0.02	12.9	44.15 (304.5)	2.43	1.798	7.05	-

Table 3.1 Major geometric and material parameters of tubes tested.

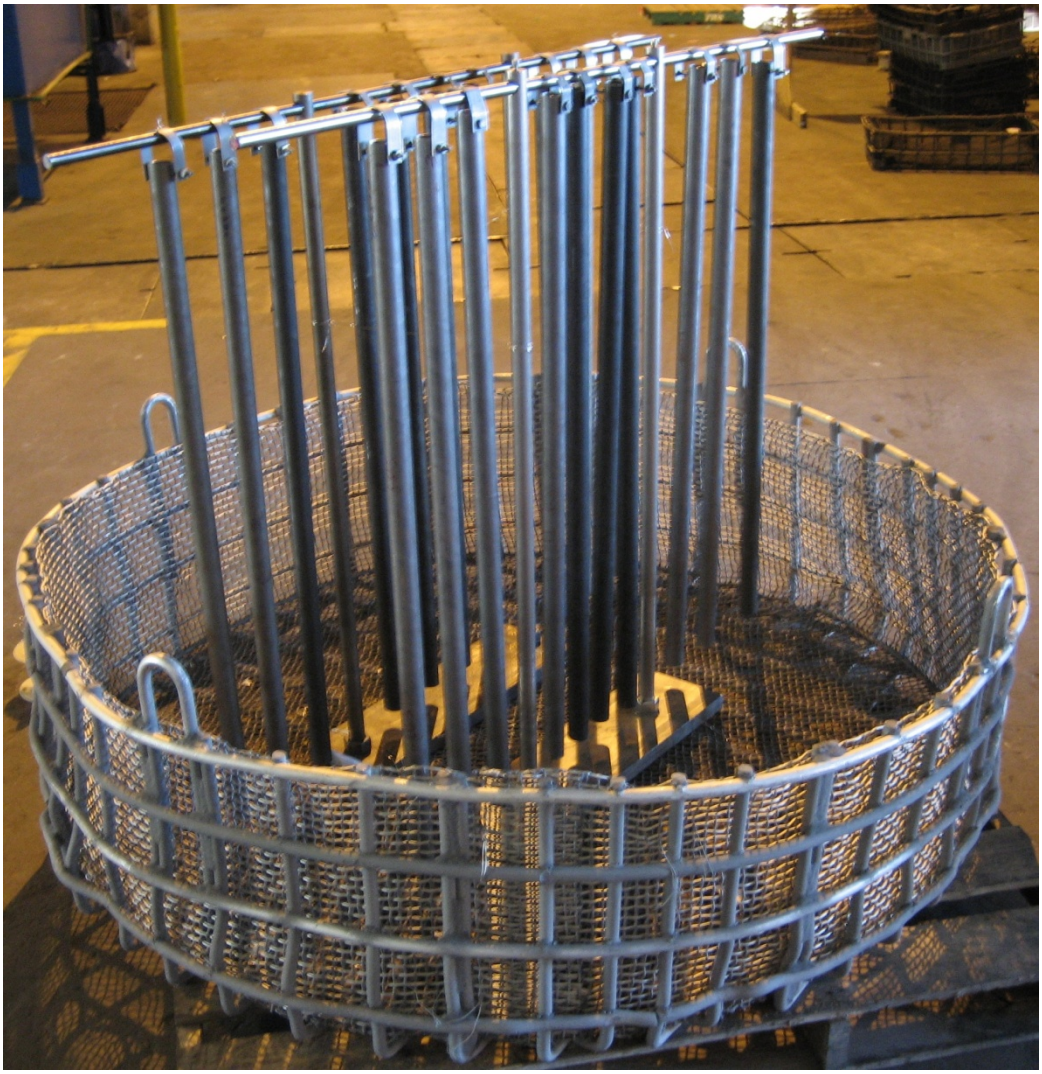

Fig. 3.1 Tubes ready for heat treatment.

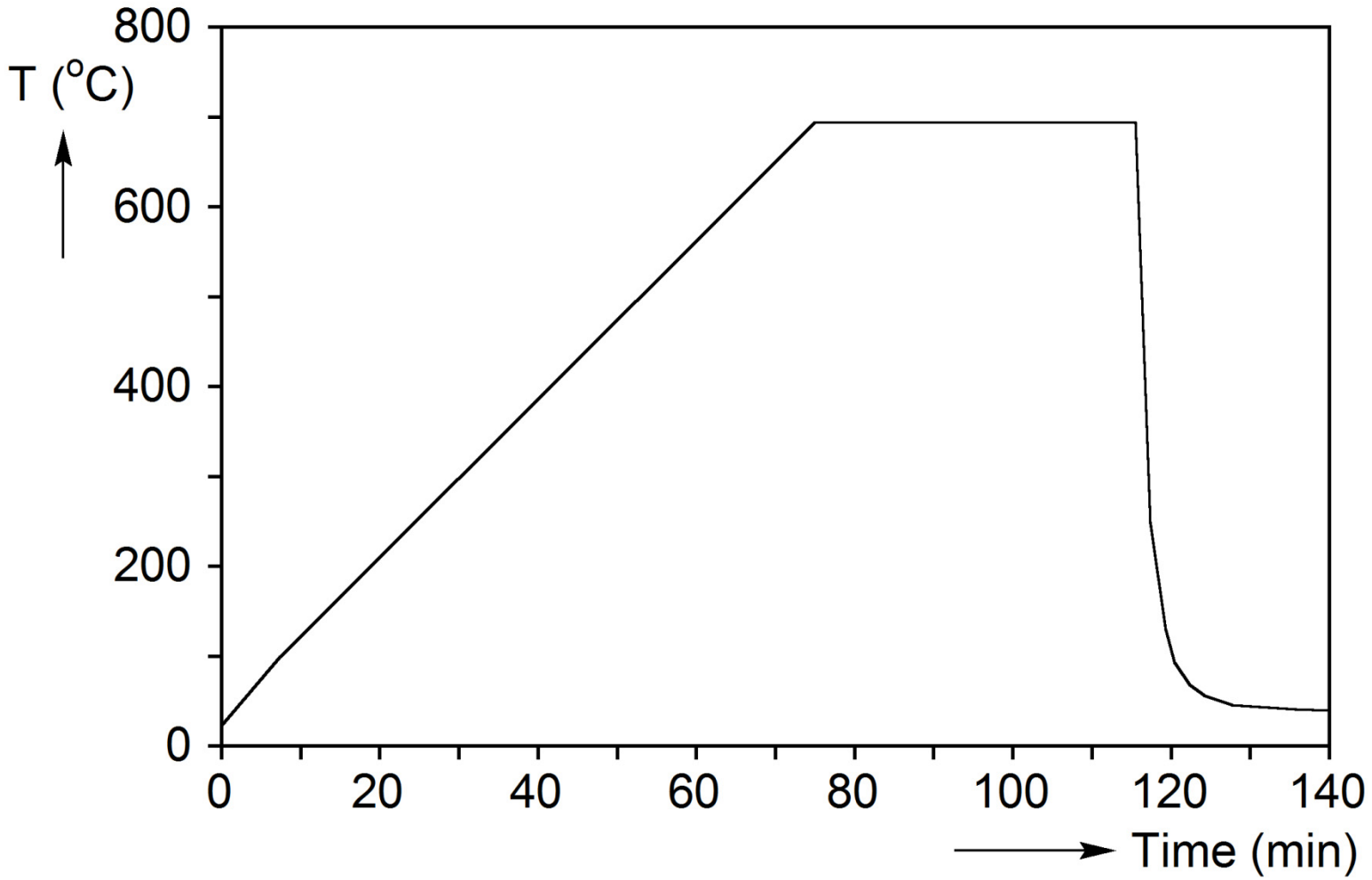

Fig. 3.2 Temperature history during heat treatment.

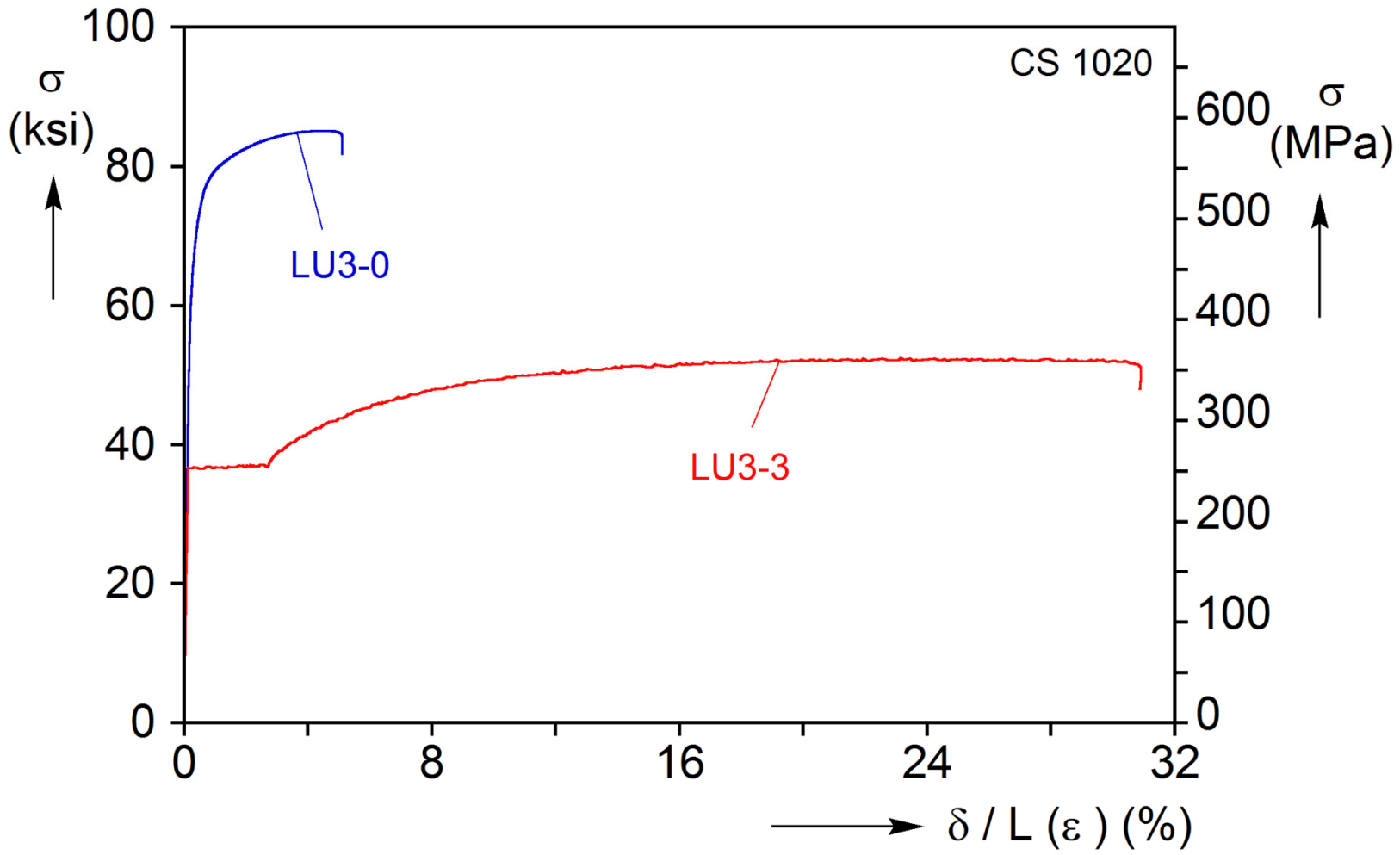

Fig. 3.3 Stress-elongation response of a carbon steel before (LU3-0) and after (LU3-3) heat treatment.

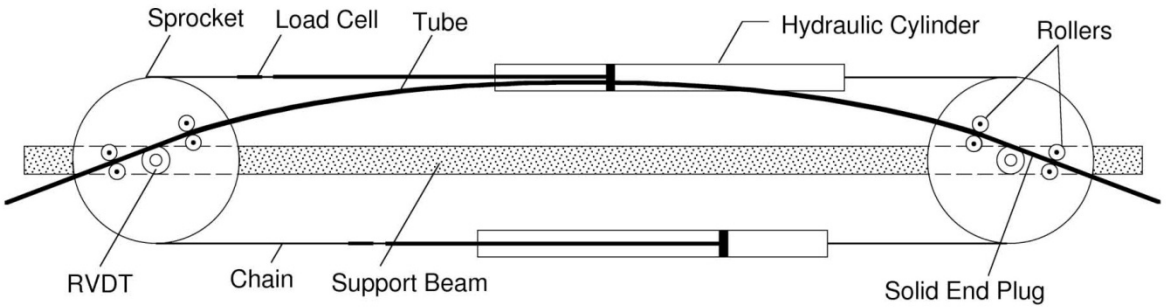

(a)

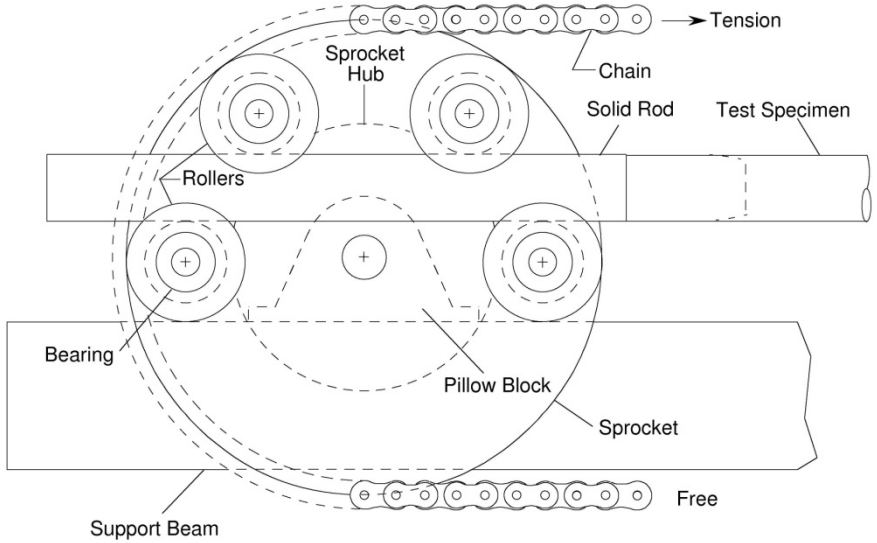

(b)

Fig. 3.4 Schematics showing the pure bending testing facility used in the experiments. (a) Bending machine and (b) load transfer assembly.

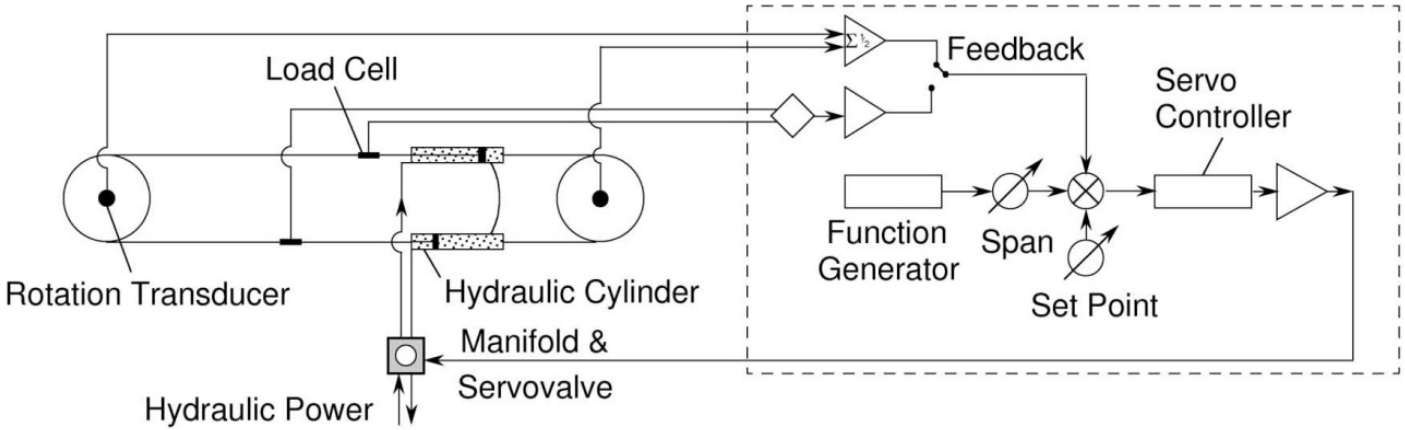

Fig. 3.5 Closed-loop controller of the bending machine operating in rotation control.

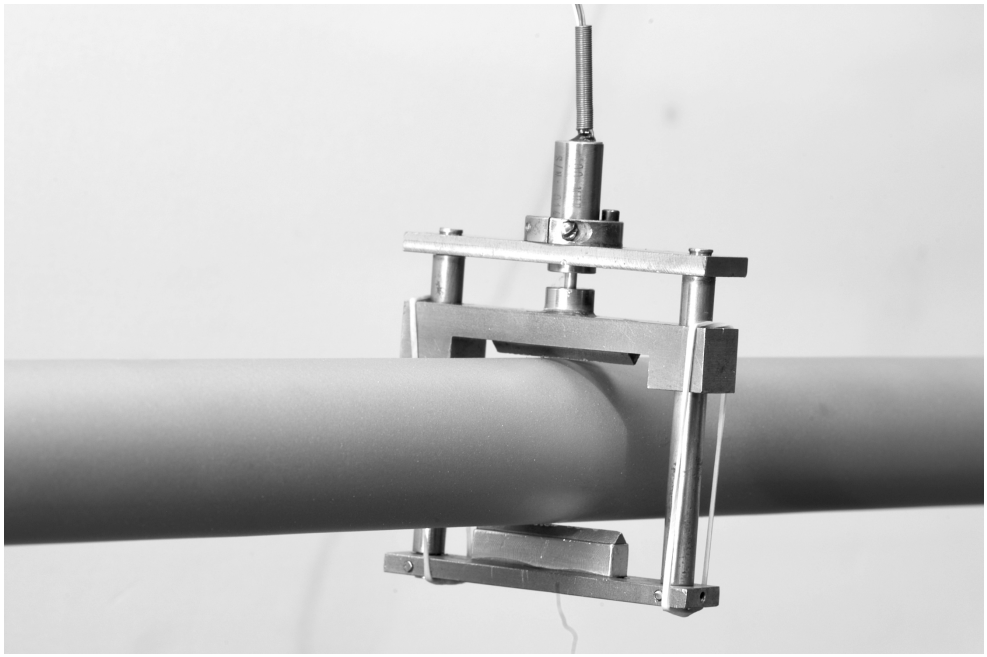

(a)

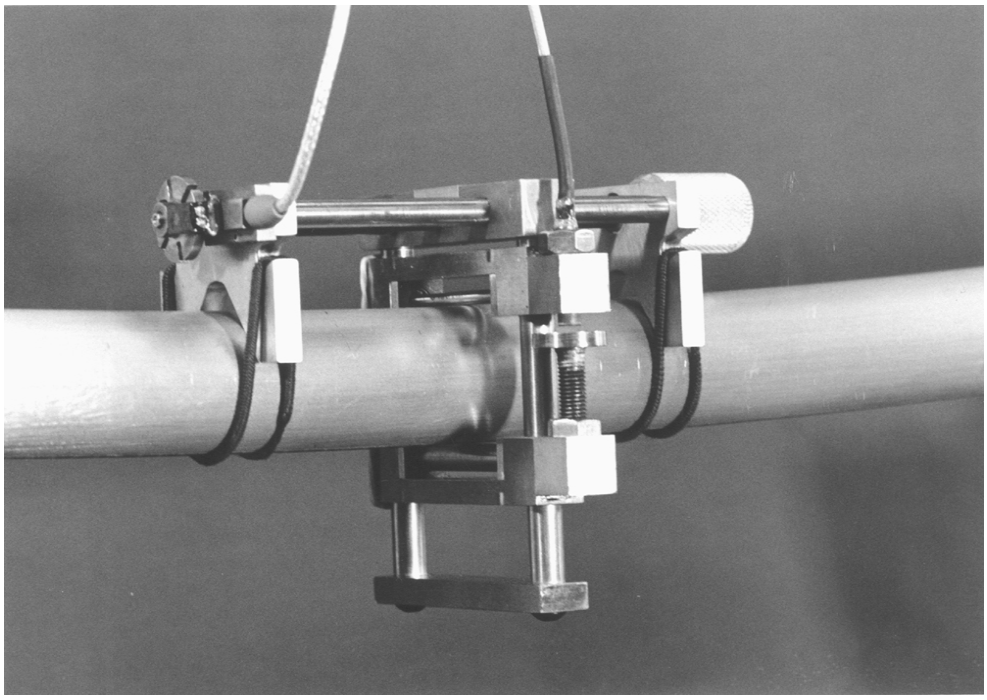

(b)

Fig. 3.6 (a) Instrument for measuring ΔD at a fixed axial location.
(b) Instrument for measuring ΔD along the specimen length.

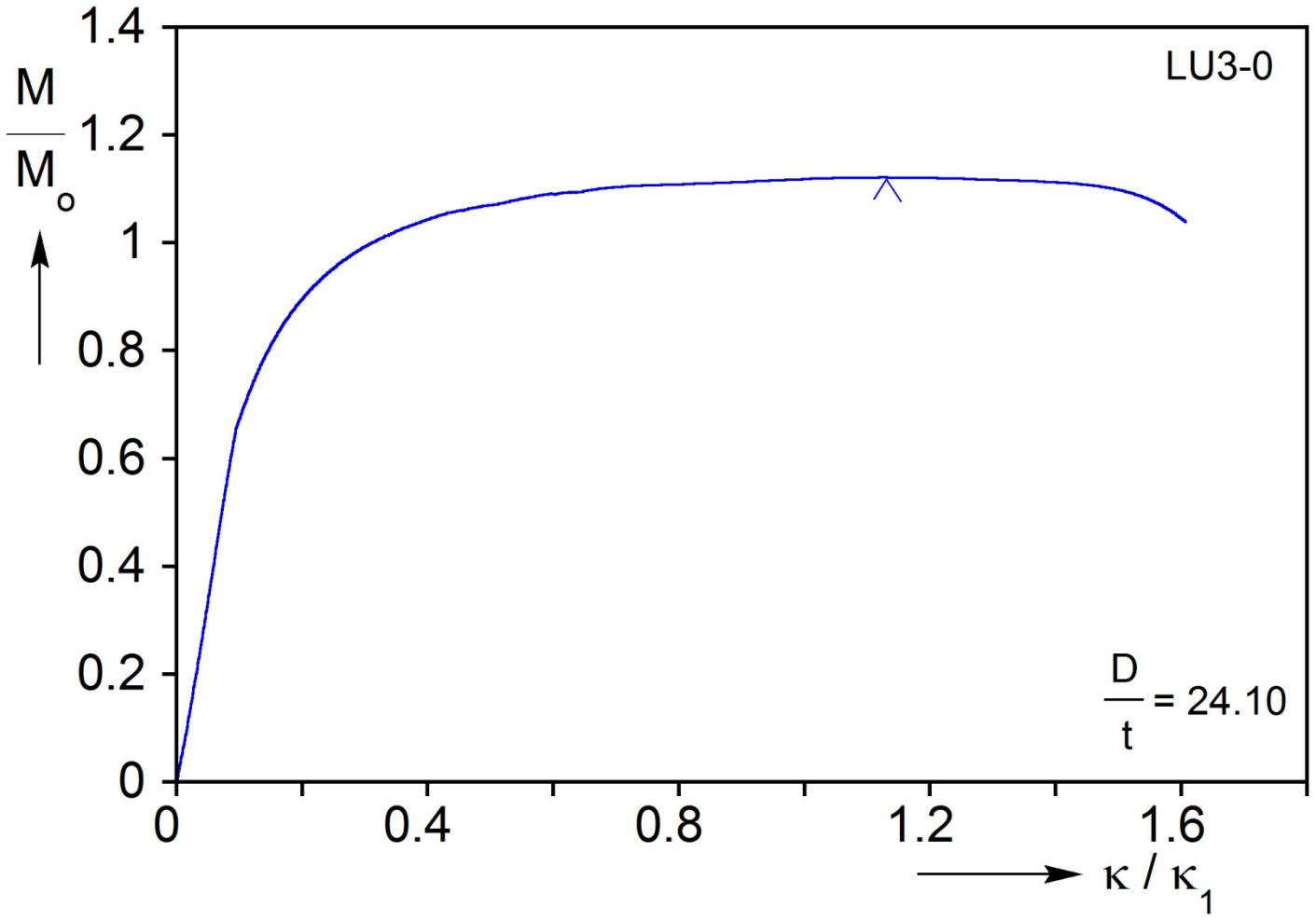

Fig. 3.7 Moment vs. curvature response recorded in Exp. LU3-0 (before heat treatment).

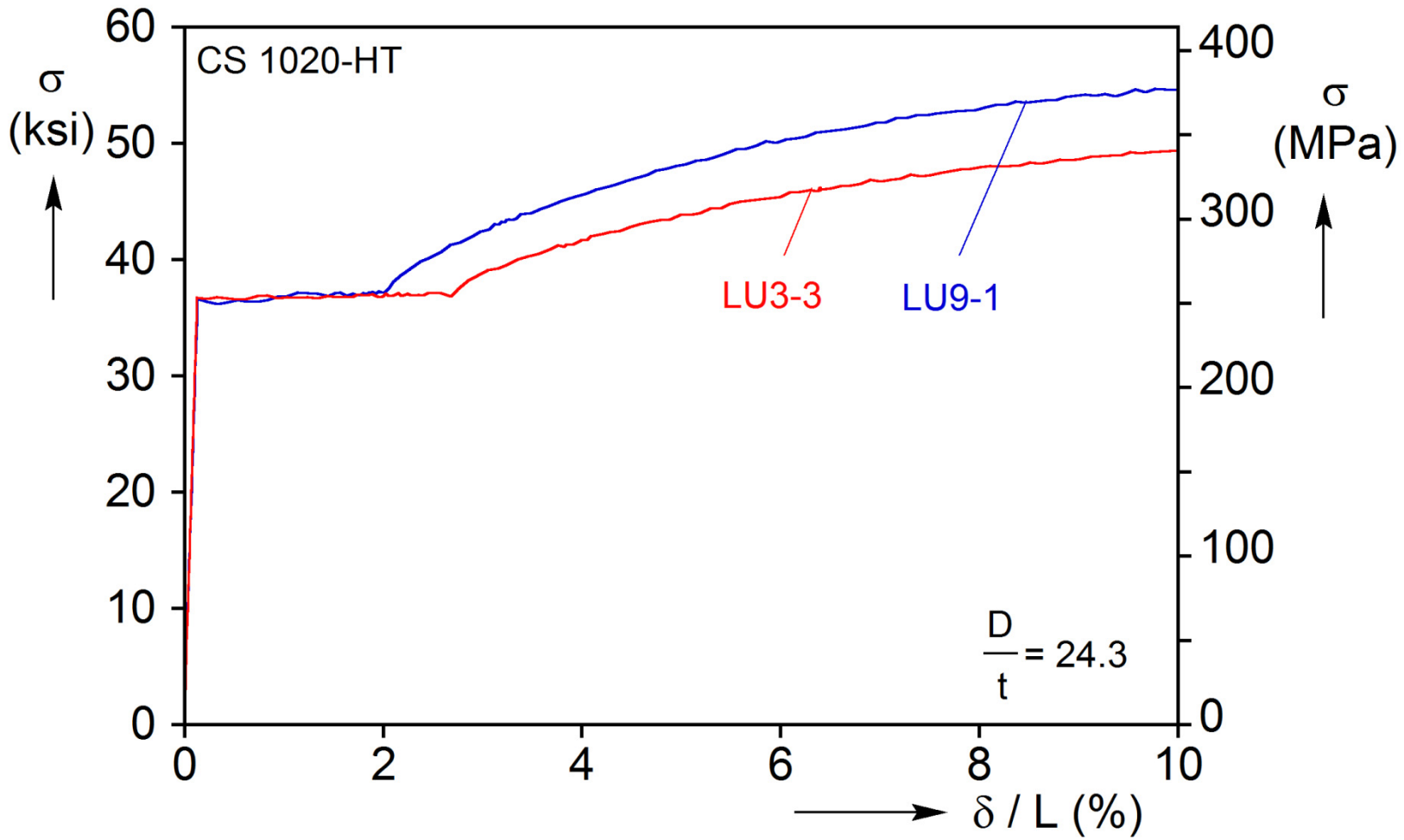

Fig. 3.8 Stress-elongation responses with different Lüders strains.

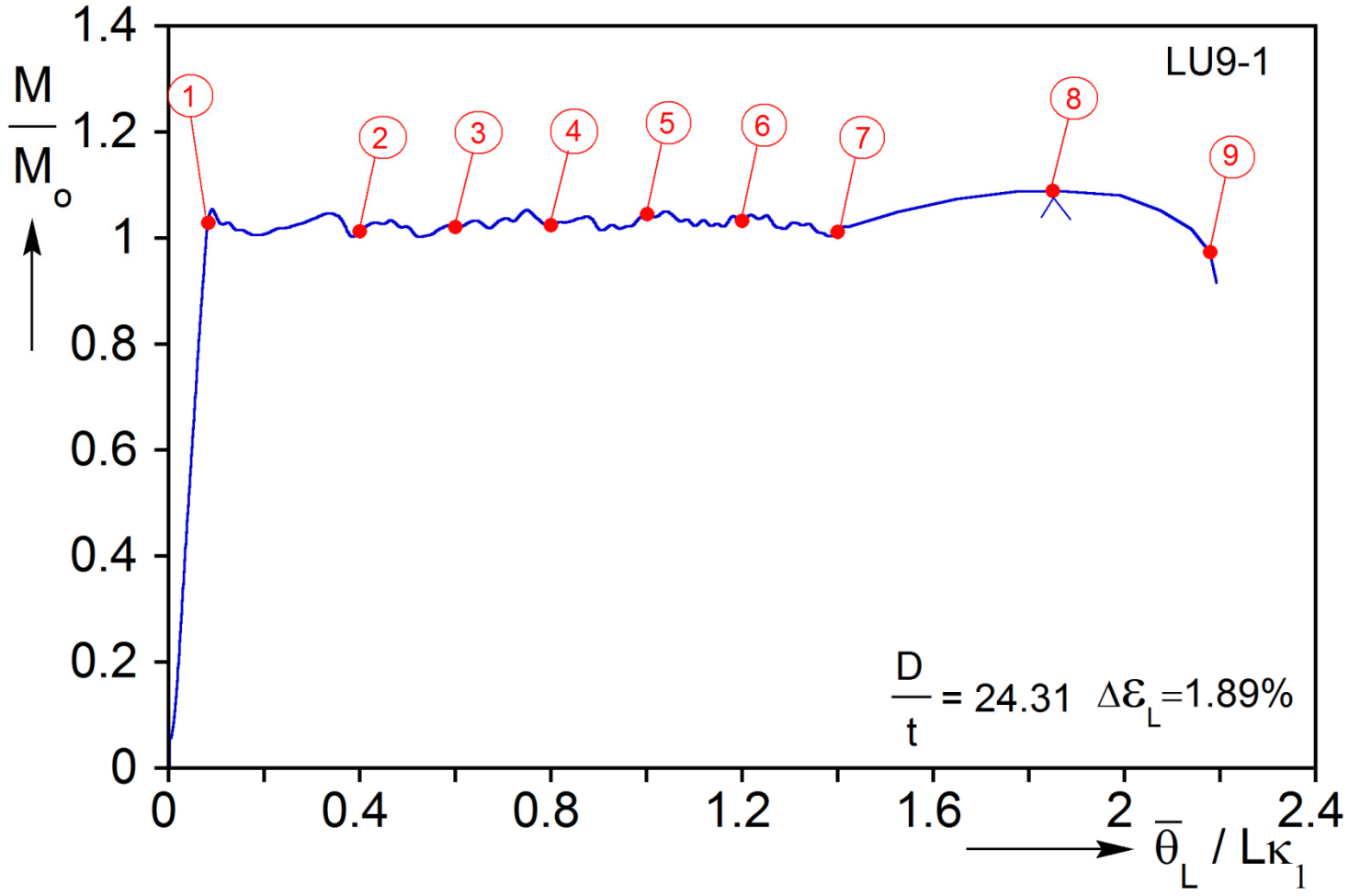

Fig. 3.9 Moment vs. end-rotation response recorded in Exp. LU9-1.

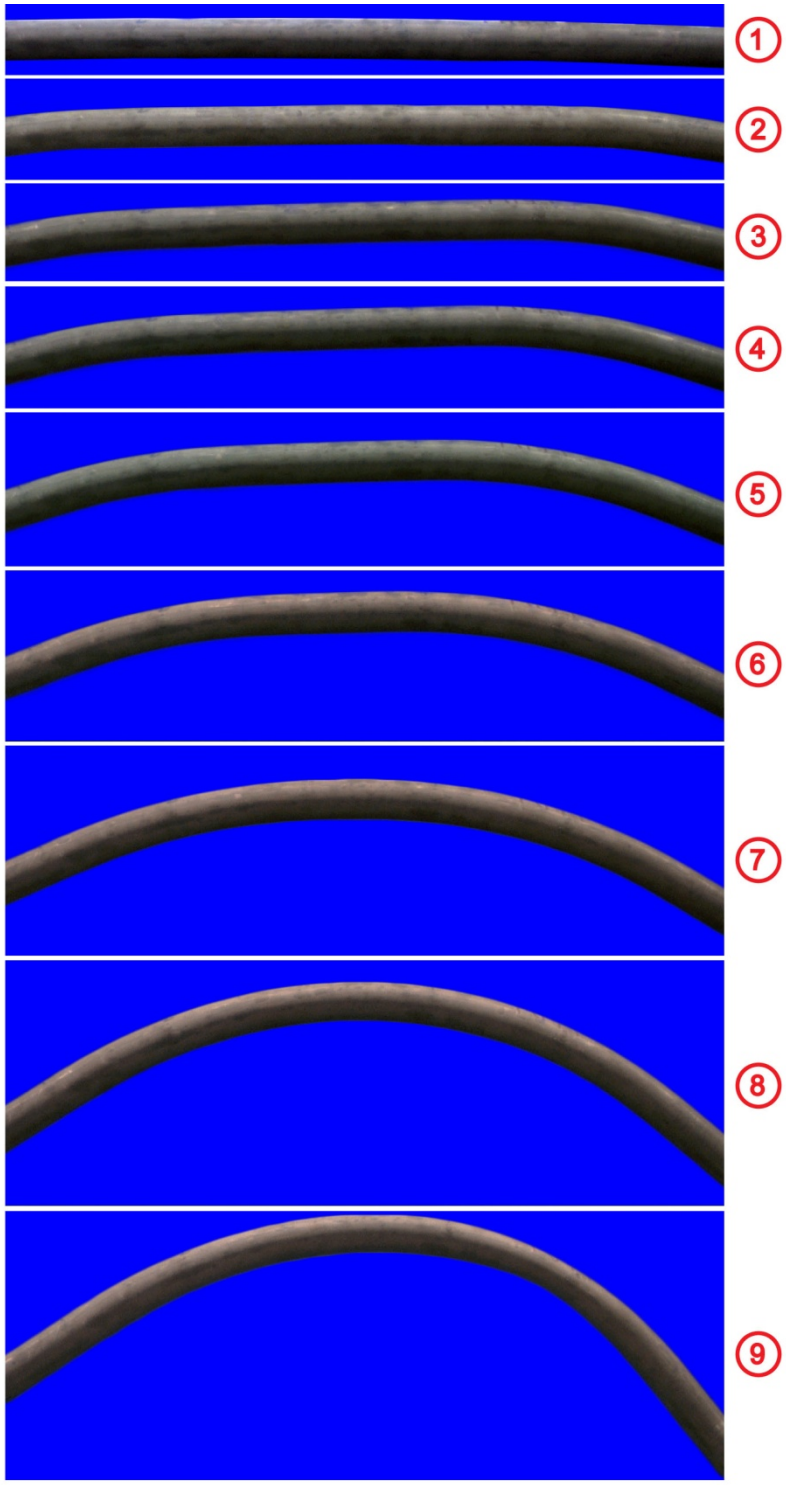

Fig. 3.10 Sequence of specimen bent configurations for Exp. LU9-1 (numbers correspond to bullets marked on response in Fig. 3.9).

(a)

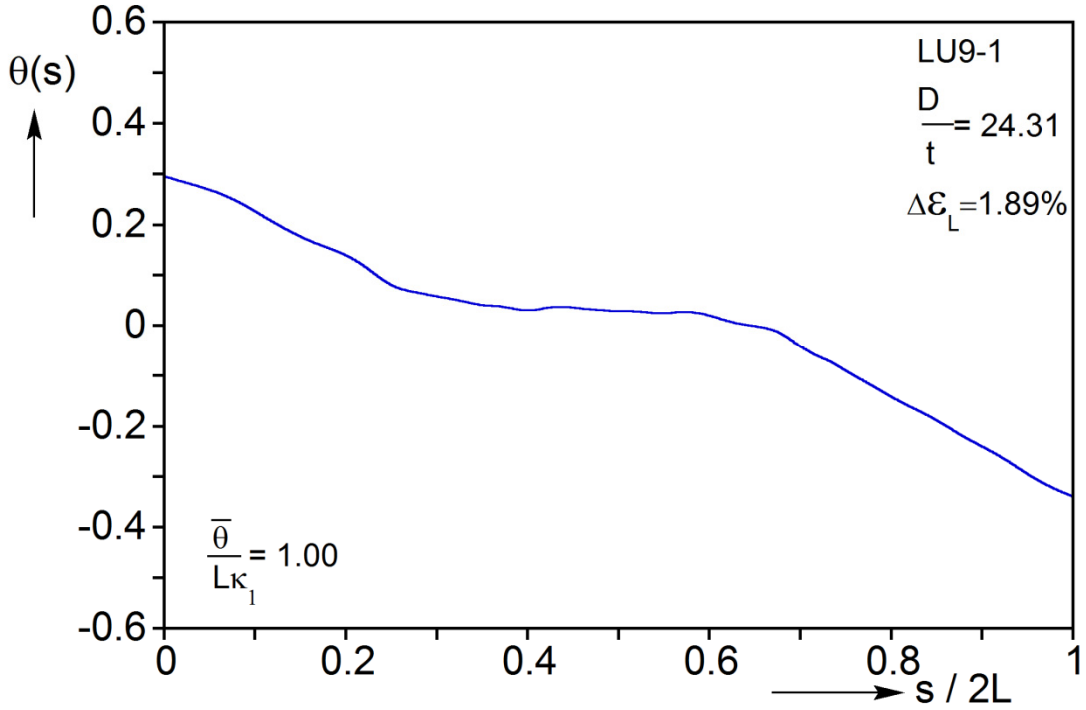

(b)

Fig. 3.11 Configuration ⑤ in Fig. 3.10. (a) Specimen edges and (b) corresponding $\theta(s)$.

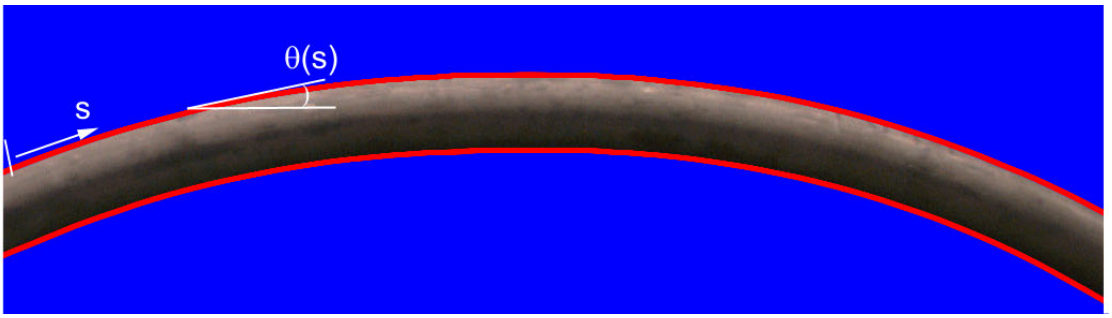

(a)

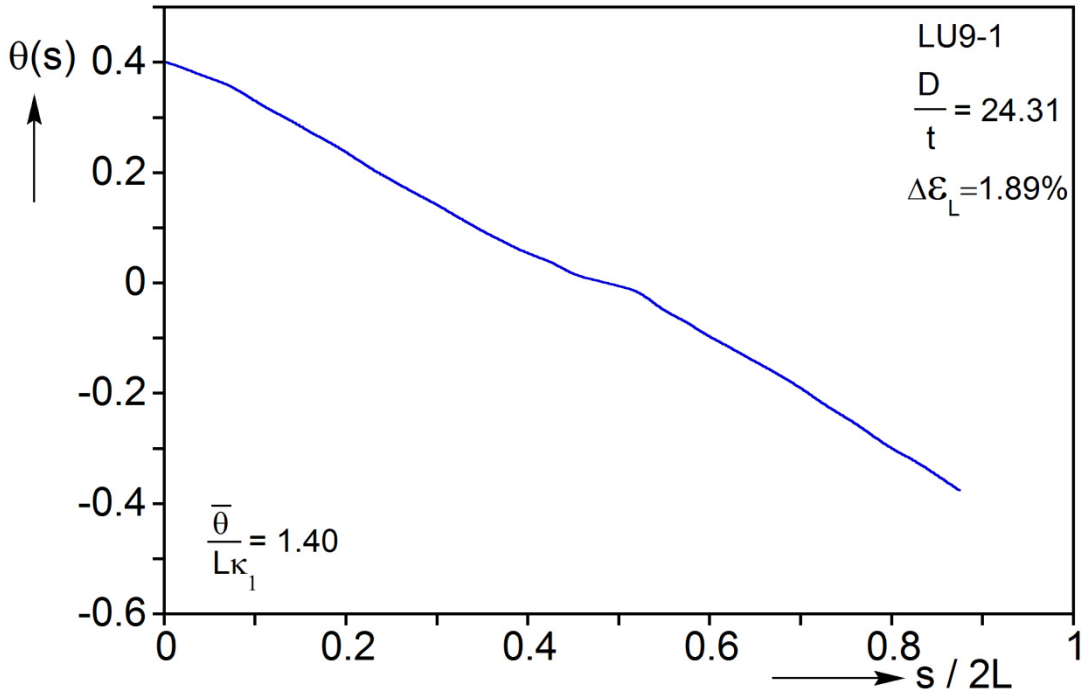

(b)

Fig. 3.12 Configuration ⑦ in Fig. 3.10. (a) Specimen edges and (b) corresponding $\theta(s)$.

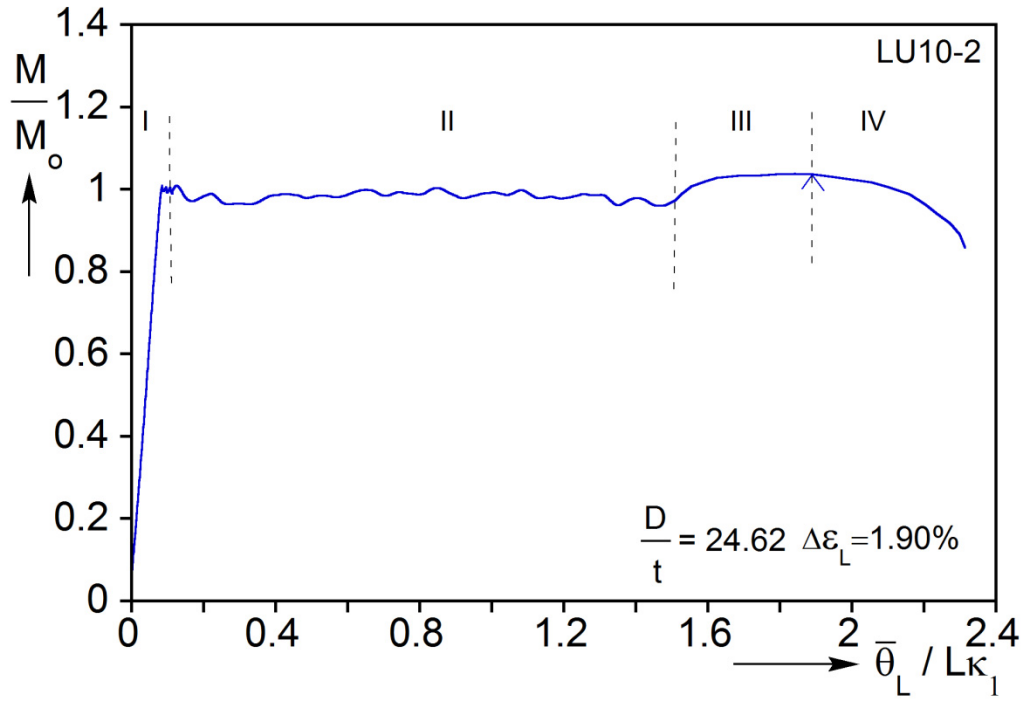

(a)

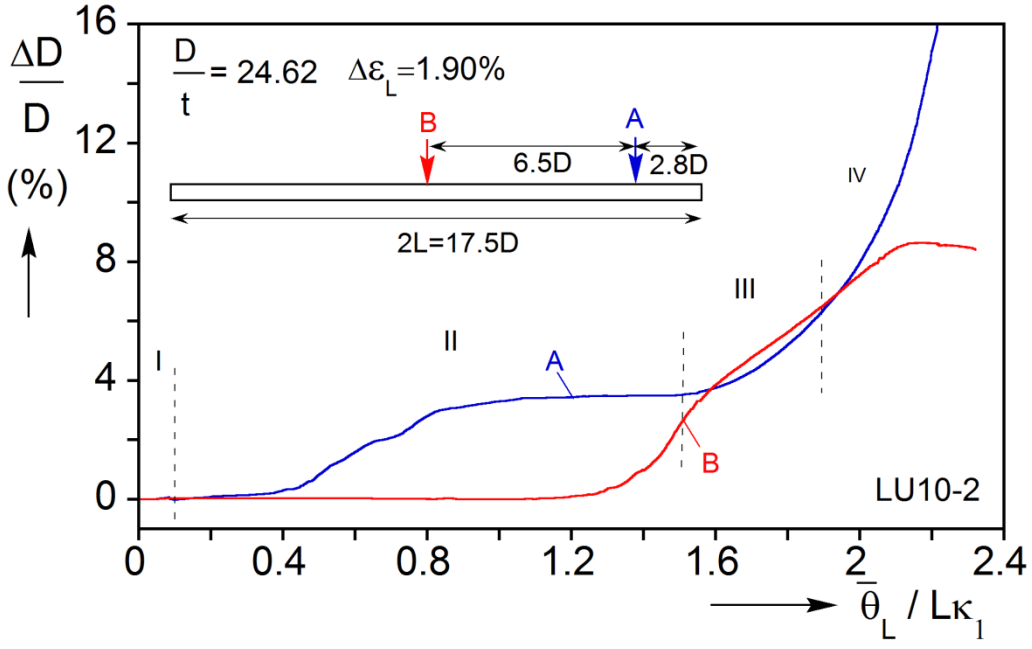

(b)

Fig. 3.13 Results from bending experiment on LU10-2: (a) moment vs. end-rotation response and (b) change in diameter recorded at two locations.

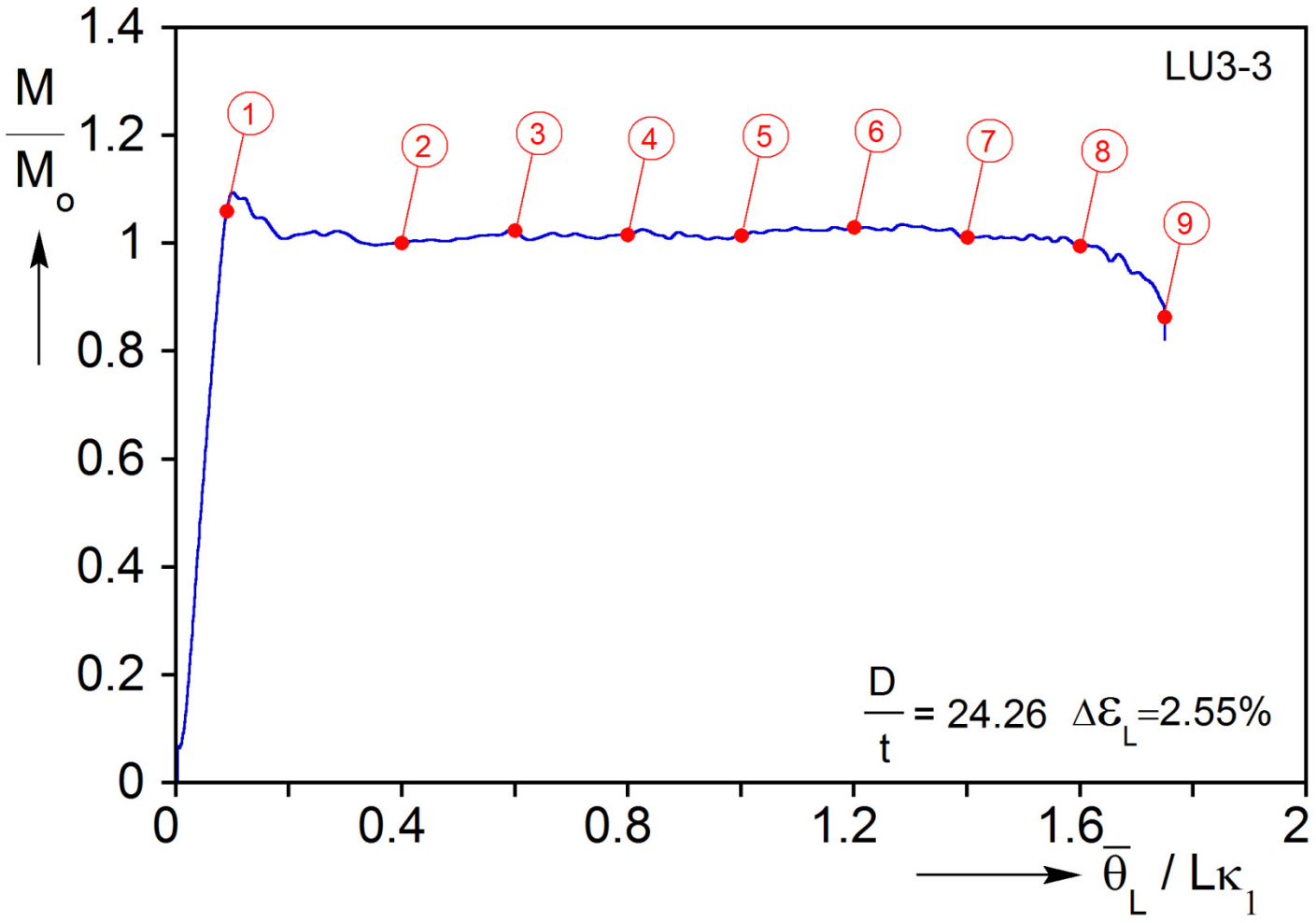

Fig. 3.14 Moment vs. end-rotation response recorded in Exp. LU3-3.

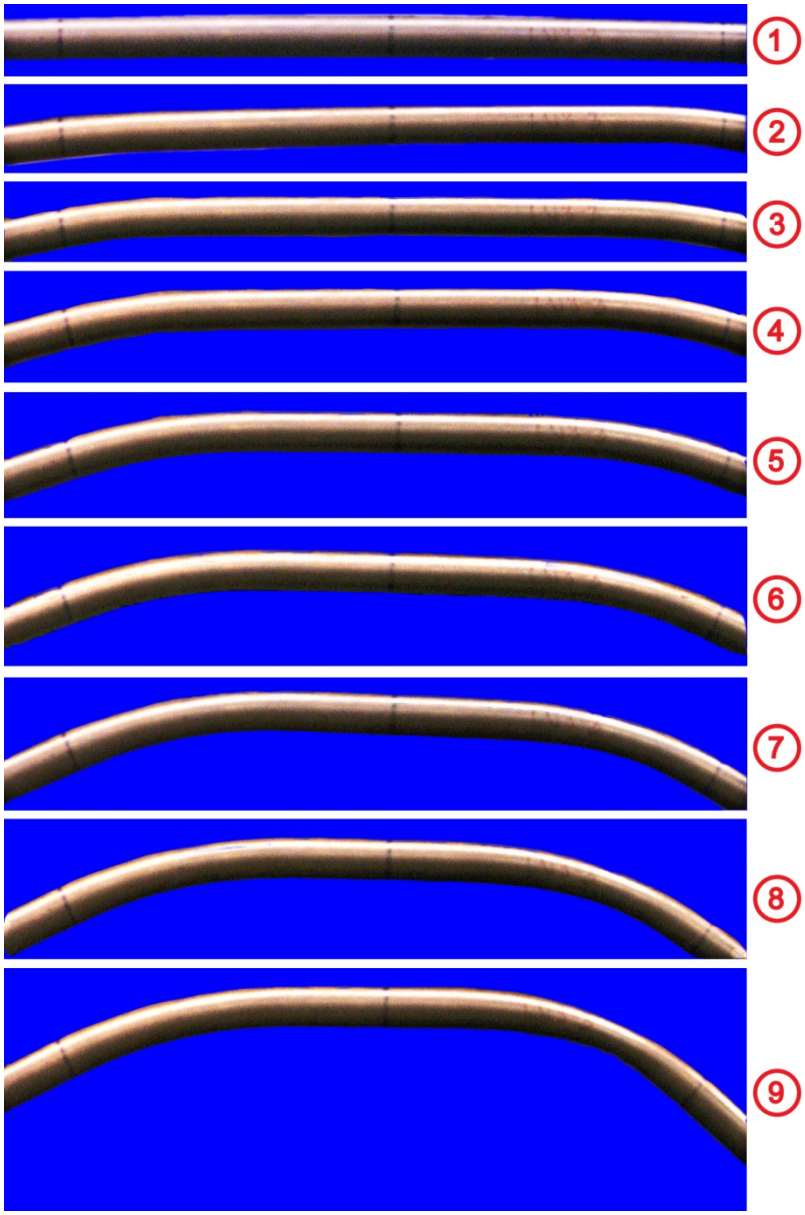

Fig. 3.15 Sequence of specimen bent configurations for Exp. LU3-3 (numbers correspond to bullets marked on response in Fig. 3.14).

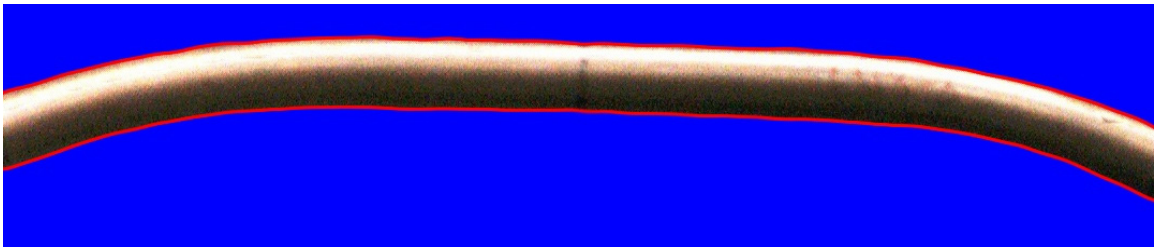

(a)

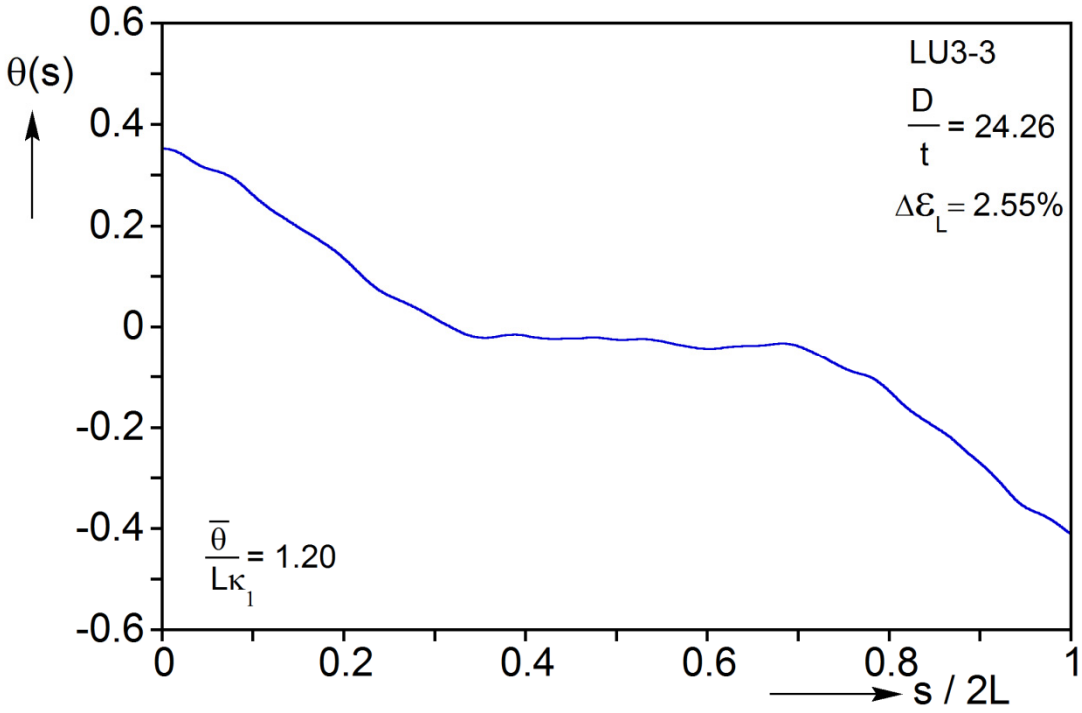

(b)

Fig. 3.16 Configuration ⑥ in Fig. 3.15. (a) Specimen edges and (b) corresponding $\theta(s)$.

Fig. 3.17 Tube from Exp. LU3-3 showing localized ovalization on the LHS, high curvature on the RHS and nearly undeformed section in the center.

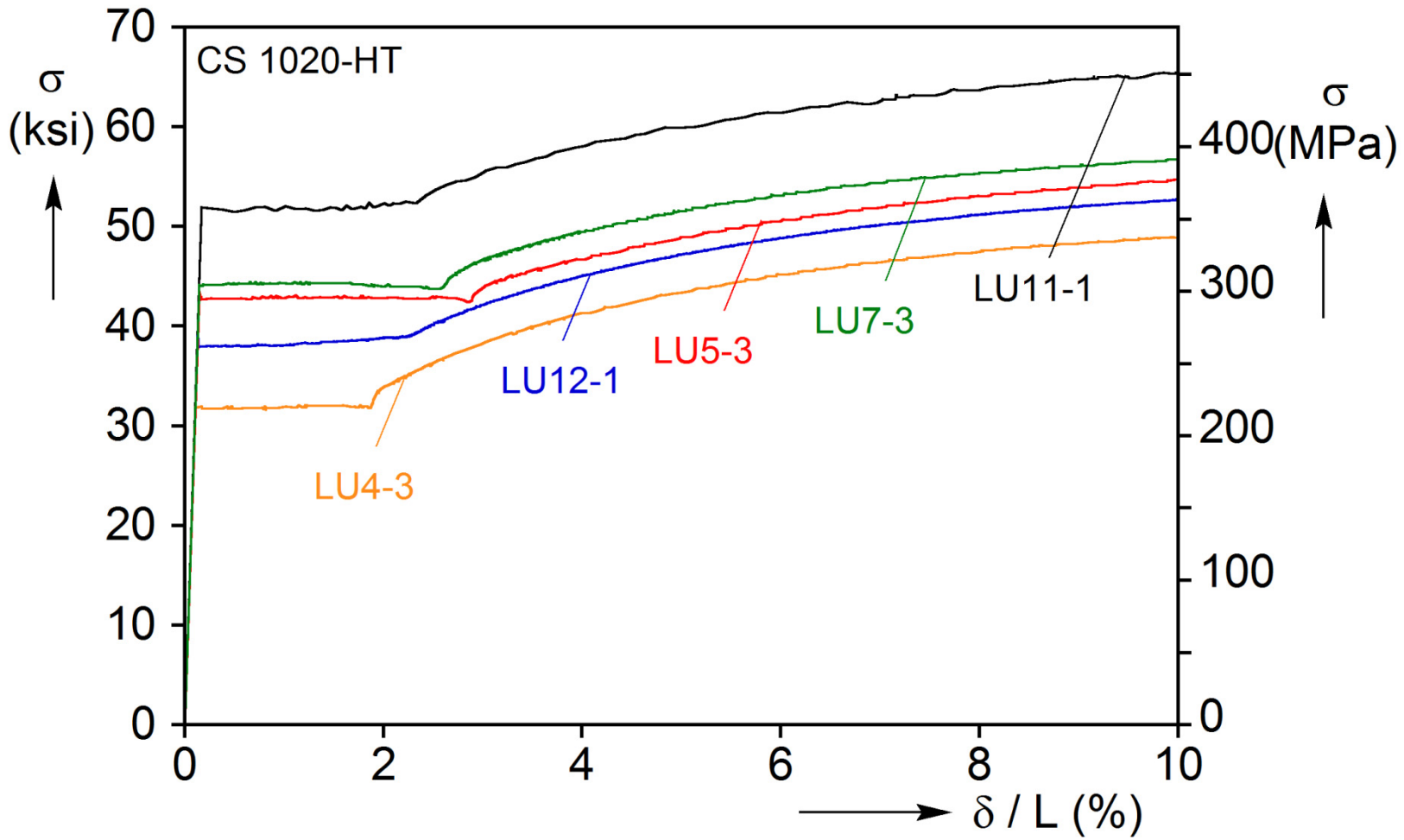

Fig. 3.18 Stress–elongation responses from a set of tubes of various *D/t* ratios and Lüders strains.

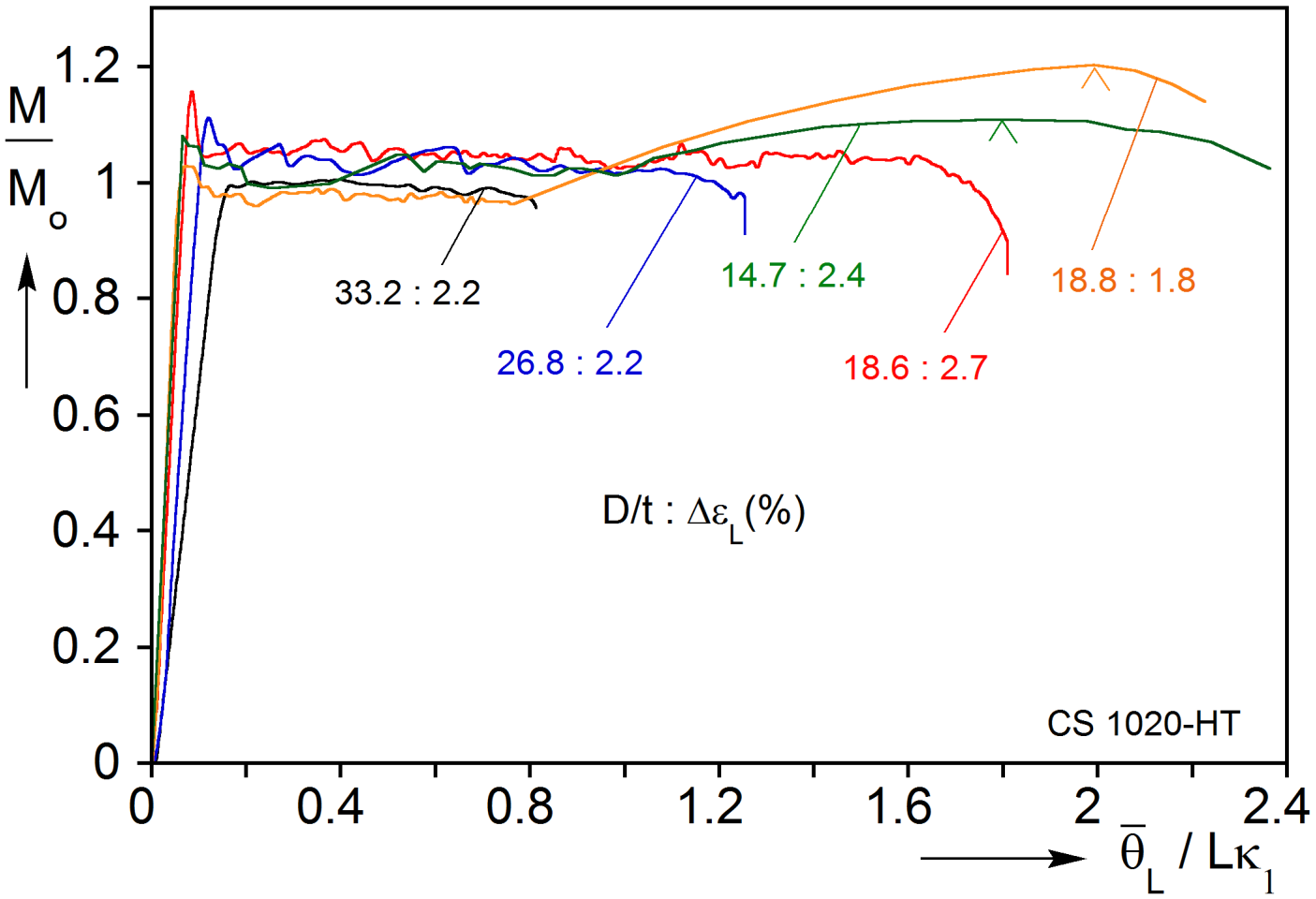

Fig. 3.19 Moment vs. end-rotation responses of a set of tubes of various *D/t* ratios and Lüders strains.

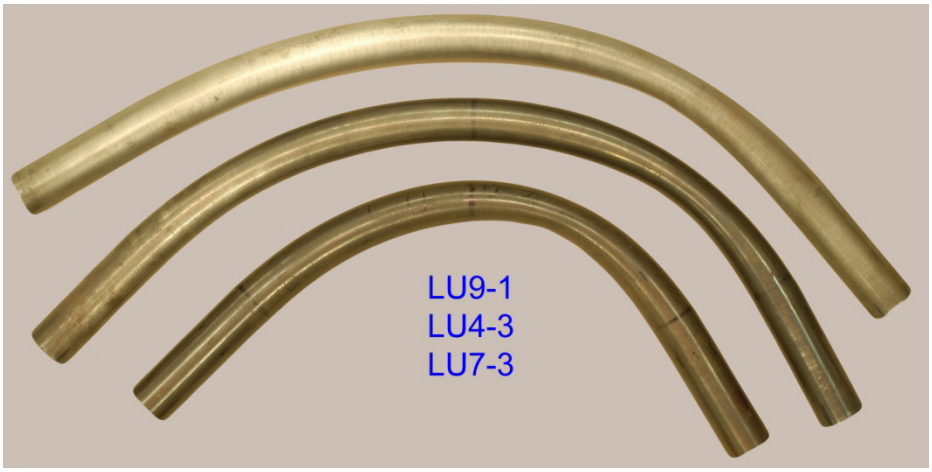

(a)

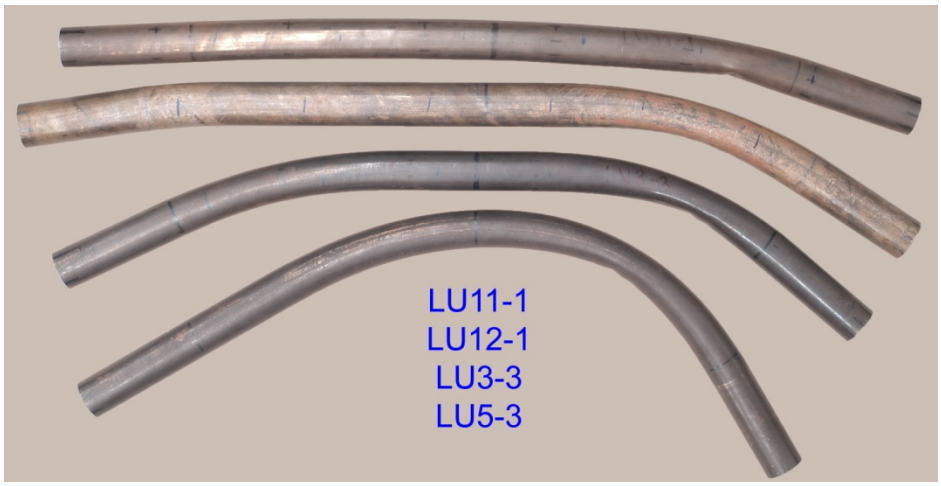

(b)

Fig. 3.20 Photographs of a set of tubes of various *D/t* ratios and Lüders strains. (a) Tubes that survive the inhomogeneous deformation phase and (b) tubes that collapsed before reaching uniform deformation.

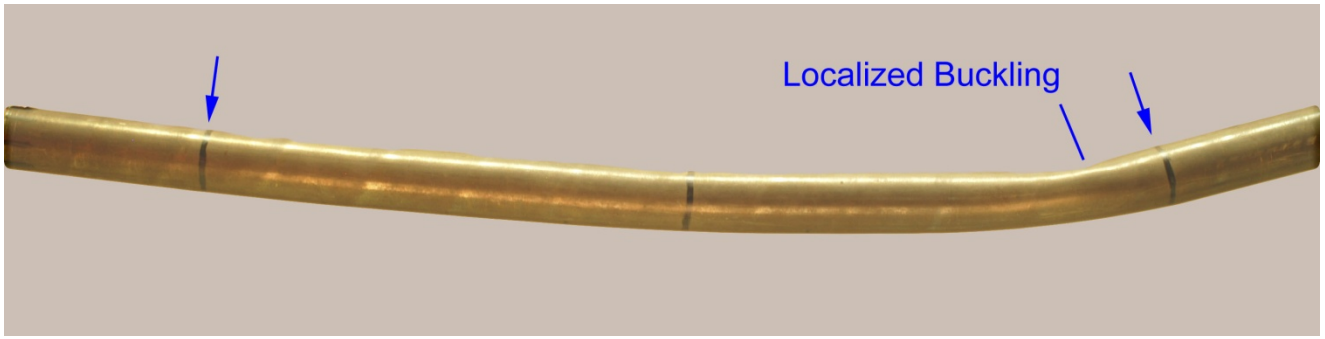

(a)

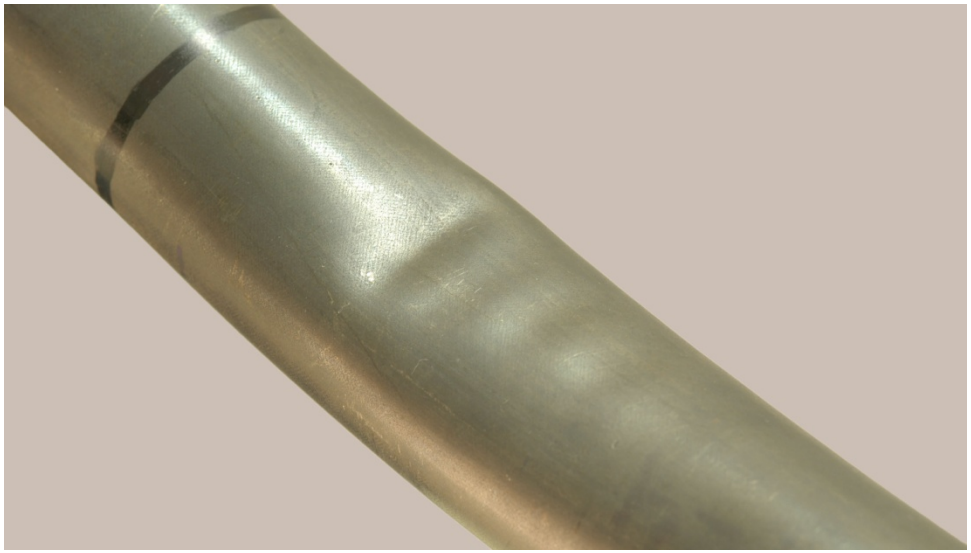

(b)

Fig. 3.21 Photograph of specimen from Exp. LU11-1. (a) Localized buckling and (b) close-up view of wrinkling and buckled region.

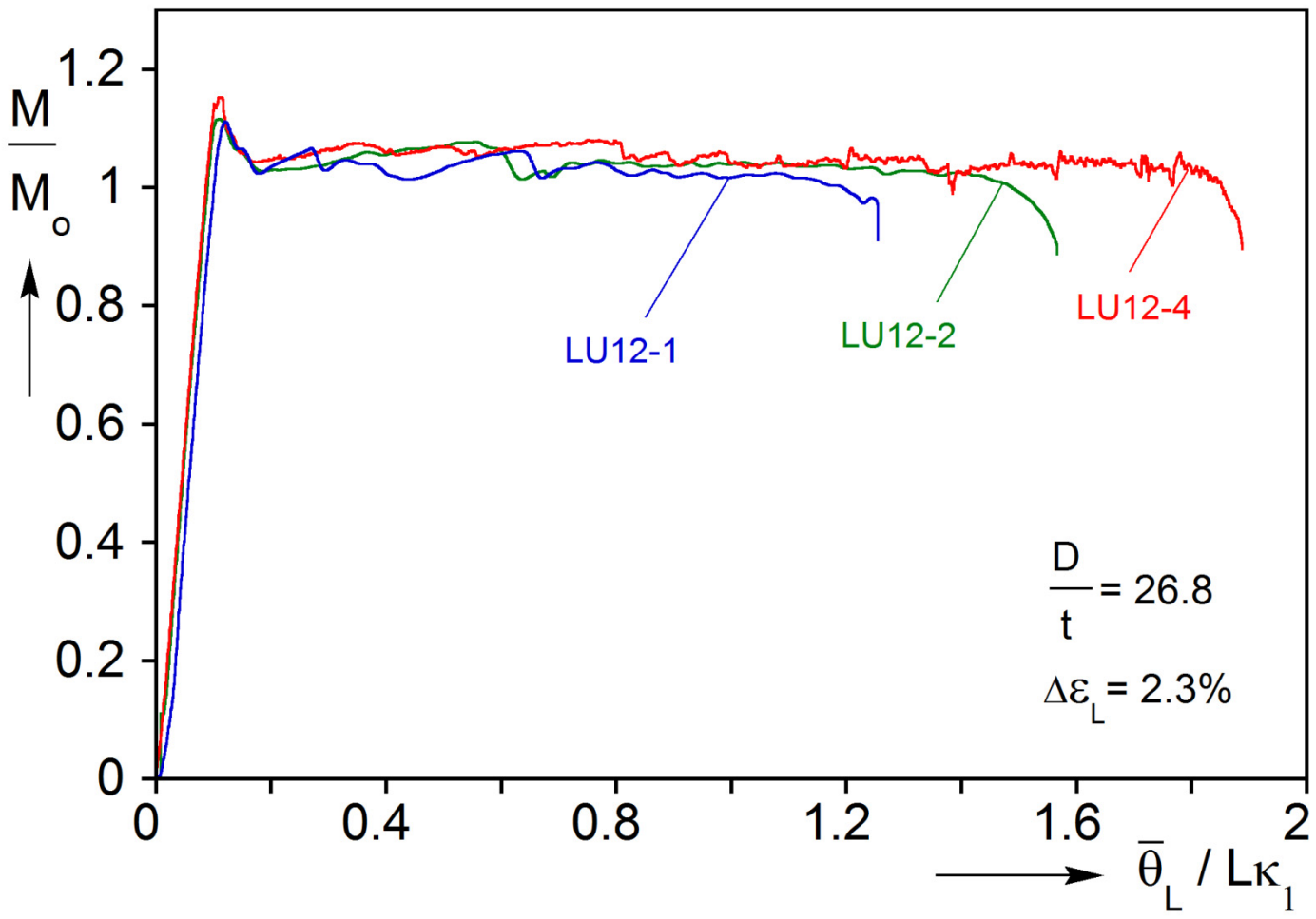

Fig. 3.22 Moment vs. end-rotation responses of experiments from a relatively high *D/t* tube where initial geometric imperfections influence the onset of collapse.

(a)

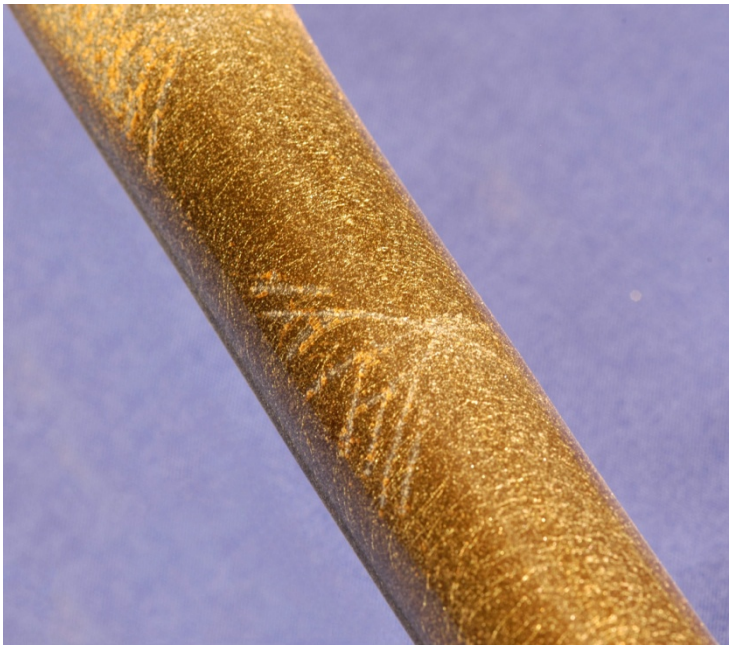

(b)

Fig. 3.23 Photograph of specimen Exp. LU11-5 showing Lüders patterns on compressed side of the tube. (a) Clusters of Lüders bands and (b) close-up of one of the clusters.

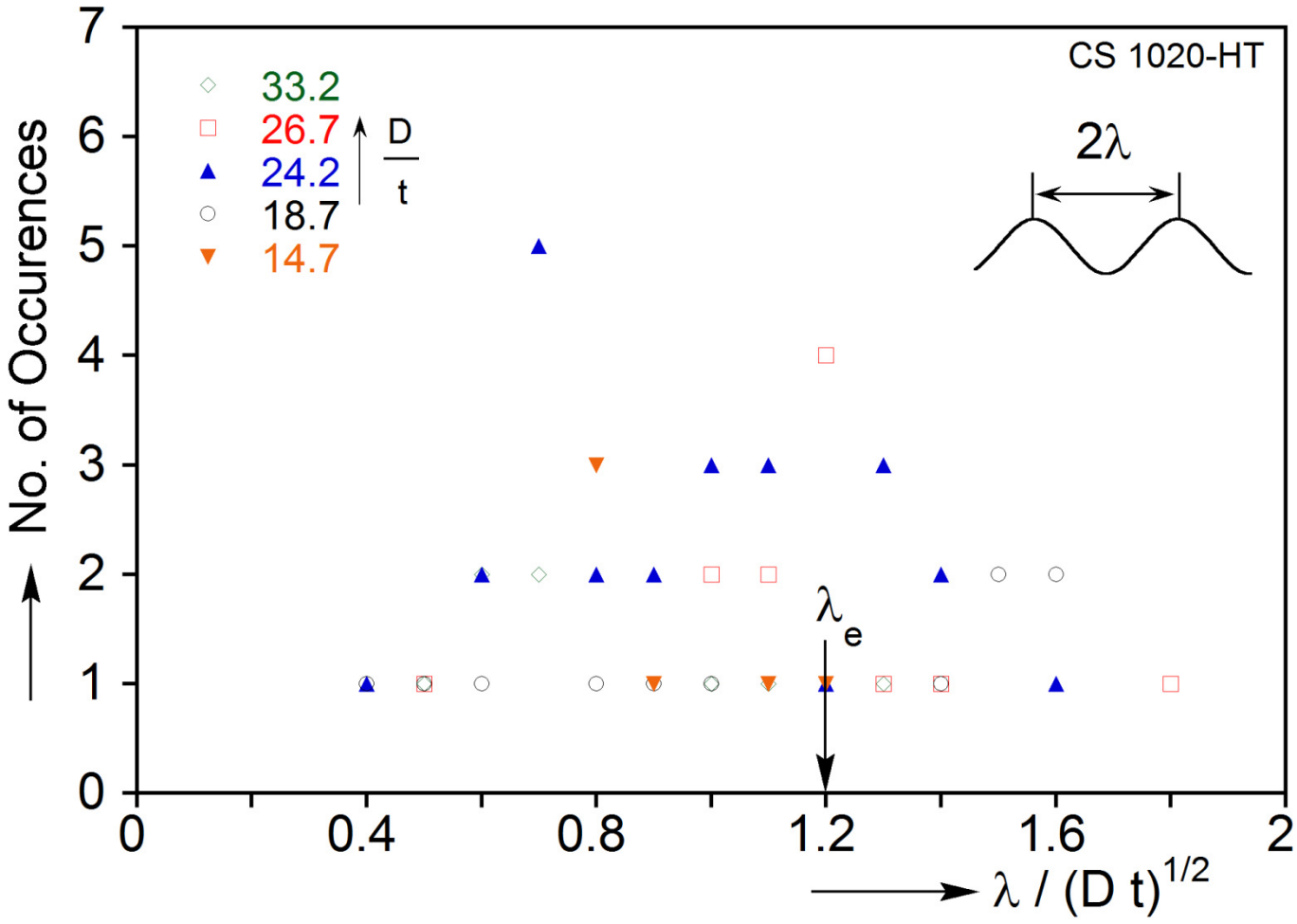

Fig. 3.24 Histogram of wrinkle wavelengths for tubes from five tube *D/t* families tested.

Chapter 4: BENDING SIMULATIONS

The experiments presented in Chapter 3 are now simulated with finite element models, together with the constitutive modeling developed when simulating tensile tests with Lüders bands (Chapter 2). The models used are described in detail, including the geometry and boundary conditions employed, the element type and discretization adopted, initial geometric imperfections and the constitutive model.

4.1 FINITE ELEMENT MODEL

In the experiments, the ends of the test specimens were radially restrained by the solid rod inserts. This constraint was sufficient to cause the initiation of Lüders banding and the associated localized curvature close to the ends of the tubes in all cases. Rather than simulate the experiments exactly, a somewhat idealized model geometry is adopted, that can also be used to study the problem parametrically. Thus, a section of tube of radius R, wall thickness t, and length $2L$ is loaded under pure bending. Symmetry about the mid-span (plane y-z) and about the plane of bending x-z is assumed; therefore, consideration of only one-quarter of the tube suffices (Fig. 4.1). As is customary in plastic bending (Ju and Kyriakides, 1992), the model is assigned a small initial localized axisymmetric geometric imperfection $\overline{w}(x)$ with a wavelength 2λ and amplitude a as follows:

$$\overline{w} = -Ra\cos\frac{\pi x}{\lambda}\exp\left[-\beta\left(\frac{x}{L}\right)^2\right] \tag{4.1}$$

Motivated by the experimental observations, and in the absence of a better alternative, λ is assigned the value of the elastic buckling mode given in Eq. (3.2). In order to encourage the anticipated localization to initiate at mid-span, the imperfection has a bias

that dies exponentially away from $x = 0$ with β controlling the rate of decay. In the results that follow unless otherwise stated $\beta = 100$. Figure 4.2 shows that such a rate of decay translates to an imperfection that affects only 20% of the effective length of the model (3 wavelengths). The amplitude *a* varies slightly from case to case (see Table 4.1).

The tube is bent by prescribing the angle of rotation at $x = L$ (θ_L). This end is constrained to remain plane, while the cross section is free to ovalize by imposing the following multi-point constraint:

$$\tan\theta_L = \frac{x_{ref} - x_i}{z_{ref} - z_i} \tag{4.2}$$

where (x_i, z_i) are the coordinates of the i^{th} node in this plane and (x_{ref}, z_{ref}) are those of a reference node (e.g., the bottom node). The moment is calculated at the plane of symmetry ($x = 0$) from:

$$M = 2\sum_{i=1}^{N} z_i F_i \tag{4.3}$$

where F_i is the axial force acting on the i^{th} node of the cross section and z_i is its distance from the axis of the tube.

The nature of the problem requires the use of solid (3D) elements. Aguirre (2002), in his study of the initiation of Lüders bands in tubes under bending, compared the results obtained from three linear element types: C3D8R (reduced integration), C3D8 (full integration) and C3D8I (incompatible modes). He showed that in the model with the C3D8I type, the banded deformation patterns naturally developed for coarser meshes.

This results from the element formulation, which allows the deformation gradient to vary inside the element. Thus, as in Chapter 2, C3D8I elements are adopted. In order to avoid any directional bias a uniform isotropic mesh is used. The mesh adopted in most of the calculations reported has two elements through the thickness of the tube. Thus, for example, for D/t = 24.3 there are 76 around the half circumference and 362 along the length (L = 7.5D) for a total of 55,024 elements. This density was arrived at from a convergence study where the major characteristics of the predictions were evaluated by comparison to the experimental results. The main parameters of concern were the correct reproduction of the level of the moment plateau and its extent as well as consistency in the calculated banded Lüders deformation patterns. Other isotropic meshes considered had 1, 3 and 4 elements through the thickness with a total of 6,878, 185,706 and 440,192 elements respectively (because the mesh uses the wall thickness as its length-scale the number of elements varies with the D/t).

The same constitutive model used in Chapter 2 is also adopted here. Thus, a measured engineering stress-strain response such as the one drawn in red color in Fig. 4.3 is modified as follows. The initial linear elastic branch with the measured modulus E is adopted. The elastic branch terminates at the upper yield stress that is $\Delta\sigma/2$ higher than the plateau (σ_L) of the measured response. It is followed by a linear softening branch, which is drawn with a blue dashed line in the figure. Its termination point at the end of the Lüders stress plateau is at a level that makes the areas of the two shaded triangles equal. Beyond this point, the fit follows the hardening part of the measured stress-strain response (in piecewise linear manner). As in Chapter 2, rate dependence is introduced by means of a power law with rate exponent $m = 0.001$.

ABAQUS Standard was used with the STATIC card. The CONTROLS option was used with "analysis=discontinuous", that improves efficiency for severely

discontinuous behavior by allowing relatively many iterations prior to beginning any checks on the convergence rate, and with "parameters=line search", that can be viewed as an "insurance policy" for Newton-like methods (Hughes and Ferencz, 1990). The duration of each simulation is the same as in the corresponding experiment (typically 5 to 10 minutes) and a maximum increment of $0.01°$ of rotation at the end of the tube is enforced.

4.2 Simulation of Typical Experiments

The modeling framework summarized above is now used to simulate several representative experiments. Each simulation uses the actual geometric and material parameters of the tube tested (Table 3.1). The results will be used to illustrate the extent to which the phenomenological model adopted reproduces both the structural events associated with inhomogeneous deformation and at a finer scale the Lüders banding.

4.2.1 D/t = 24.31, $\Delta\varepsilon_L$ = 1.89%

We start with Exp. LU9-1 with the parameters given in Table 4.1. Figure 4.4 shows the calculated moment-end rotation response with the moment, M, normalized by the fully plastic moment M_o and the end rotation, θ_L, by $L\kappa_1$. Figure 4.5 shows a set of 11 deformed configurations of the quarter-tube domain analyzed, corresponding to the numbered bullets on the response. The material response adopted in this simulation is the one drawn with a blue dashed line in Fig. 4.3. The $M-\theta_L$ response is seen to generally reproduce the main features of the corresponding measured response drawn in Fig. 4.4 in dashed line; i.e., the initial moment maximum, the level and extent of the moment plateau that follows, the subsequent stable branch, the second moment maximum and the curvature at which it occurs, are all faithfully reproduced. Aguirre et al. (2004) and Kyriakides et al. (2008) have shown that the assumed unstable material response

produces a moment plateau at the correct level. At the same time, the configurations in Fig. 4.5 bring to fore the banded nature of localized deformation that develops. The bands first nucleate near the mid-span and gradually spread to the rest of the domain analyzed (color keys correspond to equivalent plastic strain values). Before discussing the global evolution of these events, it is worth paying special attention to the first initiation phase of the bands.

a. Initiation of Localization Bands

Figure 4.6 shows an expanded view of the initial part of the moment-end rotation response. Marked on it with solid bullets are 8 points that will help follow the events that take place during the initiation of Lüders banding. Figure 4.7 shows plots of the most compressed generator of the tube ($w \equiv$ outward displacement normal to tube surface) for points ① to ④. Included is the equivalent plastic strain along this generator (ε_e^p C) and the corresponding values along the most stretched generator (T) (s is a natural coordinate along the axis of the tube). The response starts to become nonlinear at $M \approx 0.92M_o$ and gradually looses stiffness. This is presumably caused by plastic action in the neighborhood of the imperfection. This is confirmed by the recorded growth in ε_e^p at both generators in the plot corresponding to point ① in Fig. 4.7, just before the moment maximum. However, the plastic deformation is not sufficient yet to support the formation of localized deformation bands. At point ②, at a slightly higher curvature ($0.122L\kappa_1$), the imperfect part of the generator appears more deformed and simultaneously a spike in ε_e^p develops on the tensioned side at the second imperfection peak. This point also happens to correspond to the maximum moment achieved of $1.08M_o$. Beyond this point, the moment drops down to a plateau and simultaneously bands of localized deformation nucleate at this location. At point ③ the generator is seen to be more deformed, the

moment is down to $1.06M_o$ while the local plastic strain (T) has reached a value of nearly 3%. Figure 4.8 shows six sets of images with axial plastic strain contours for points ③ to ⑧ on the response in Fig. 4.6. The images correspond to a length of the tube just under $1.5D$ long on either side of the mid-span (the full tube has been assembled for clarity). The image on the left shows a side view (i.e., in the plane of bending); the middle one is a top view (i.e., the tensioned side) and the one on the right a bottom view (i.e., the compressed side). The color contours show clearly the localized deformation bands that nucleate, grow and multiply as the end rotation (θ_L) is gradually increased. The images for point ③ show two pairs of x-shaped bands on either side of the mid-span on the tensioned side of the tube. The center of the x is located at the second imperfection peak. The bands are orientated at $\pm 55°$ to the axis of the tube and have an angular span of about $\pm 60°$. The strain levels in the bands are of the order of 2.5% at the center but decrease as they go around the circumference, eventually dying out. Simultaneously, weaker bands with the same orientation have also appeared on the compressed side of the tube. These emanate mainly from the first imperfection peak.

By point ④, the compressed generator has deformed further and plastic deformation around the first imperfection peak and valley has increased on the compressed side (Fig. 4.7). The corresponding cluster of bands around mid-span has strengthened and the bands are now clearly discernible in the corresponding image in Fig. 4.8 for both the tensioned and compressed sides.

Figure 4.9 shows an expanded view of one of the x-shaped pairs of T-bands corresponding to point ④. Their features are similar to those reported in Aguirre et al. (2004). That is, the band orientations are very similar to those yielded by Hill's characteristics obtained from simple considerations of admissible strain discontinuities in a biaxially loaded sheet (Hill, 1952; see also Bijlaard, 1940). The bending induced

ovalization introduces a bending type circumferential stress, which varies around the circumference ($\sim\cos 2\phi$). However, its amplitude is small compared to the axial stress. Thus, at the top and bottom the biaxiality ratio is small which results in the nearly perfect agreement with the $\pm 55.7°$ inclination of strain discontinuities in a uniaxially loaded sheet. For $0 \le |\phi| \le 45°$, the circumferential stress decreases and so the bands stay straight. The bands affect zones that are about 3 elements wide with the center being more deformed. Furthermore, as might be expected, the deformation penetrates the whole wall thickness while the material on either side of a band remains essentially elastic.

It is interesting to examine if the width of the band is influenced by the mesh used. To this end the same calculation was performed with four nearly isotropic meshes defined by the number of elements through the thickness. Figure 4.10 shows plots of the plastic equivalent strain along an axial line $\pm 33.2°$ from the plane of bending (line drawn in Fig. 4.9) for the four meshes. The bands look very similar for the three finer meshes with a maximum width of about $3t$ and a maximum plastic strain of about 2.5%. The results for the mesh with one element through the thickness are slightly different but this appears to be more due to the scarcity of integration points than anything else. Therefore, similarly to what was observed in the simulation of tensile tests (Chapter 2), no pathological mesh dependence is detected during the simulation of bending with Lüders bands by means of an up-down-up constitutive model.

With further rotation of the ends, the strengthening of the bands of the compressed side continues while their number increases. So in image ⑤ (Fig. 4.8), at $\theta_L = 0.138 L\kappa_1$, two pairs of C bands have fully developed reaching a strain in the range of 2-3%. As θ_L is increased further the number of both the T and C bands multiples which can be clearly seen in the images ⑥ to ⑧.

b. Propagation of Localization

It is interesting to return now to Figs. 4.4 and 4.5 in order to examine the effect of the banded localizations on the overall response of the structure. Configuration ①, corresponding to $\theta_L = 0.084L\kappa_1$ close to the first visible nonlinearity on the initial stable response, is free of Lüders bands and has a uniform curvature. The latter point is better illustrated in Fig. 4.11, which shows the slope of the mid-surface of the tube, $\theta(s)$, plotted against the natural coordinate s along the axis of the tube. The plane $s = 0$ is a plane of symmetry and thus $\theta(0) = 0$. The free end of the tube, at $s = L$, undergoes the maximum rotation $\theta(L) = \theta_L$. Thus, when the tube deforms uniformly $\theta(s)$ grows linearly between 0 and θ_L. This indeed is the case for configuration ①.

By configuration ② at $\theta_L = 0.40L\kappa_1$ the Lüders bands have propagated from the symmetry plane to the right and cover a length about $2D$ of the tube. A higher curvature zone has developed in this domain while the rest of the tube remains at the original curvature. The localization of curvature is visible in configuration ② and better quantified in the corresponding slope trajectory ($\theta_L = 0.40L\kappa_1$) in Fig. 4.11. Here two linear trajectories with different slopes are joined by a transition region extending over a length of approximately $0.5D$. The section with the larger slope has developed a curvature of $1.36\kappa_1$, while the section unaffected by Lüders bands remains at the curvature that corresponds to the first moment maximum.

As pointed out is Section 3.4.2b, the ovalization induced to the cross section differs in sites with different curvatures. Accordingly, Fig. 4.12 shows axial profiles of the calculated ovalization [$\Delta = (D_{\max} - D_{\min})/(D_{\max} + D_{\min})$] at different values of θ_L (included are also profiles for several of the configurations in Fig. 4.5 — circled numbers). In configuration ① at $\theta_L = 0.084L\kappa_1$, the tube is linearly elastic and the ovalization is small and uniform along the length. In the next two profiles at $0.15L\kappa_1$ and

$0.30L\kappa_1$ respectively, the ovalization is seen to grow locally around the mid-span because of the increasing localized deformation at this site. By configuration ②, localization of Δ now affects a length of about $2D$ while reaching a value of about 2% at mid-span.

As the end rotation increases, the inclined Lüders bands are seen in Fig. 4.5 to propagate away from mid-span into the hitherto intact part of the tube in a nearly steady-state manner (see configurations ③ to ⑥). Simultaneously, a gradual growth of the higher curvature domain takes place at the expense of the lower curvature (see Fig. 4.11). Indeed, the same can be observed in the corresponding ovalization profiles in Fig. 4.12, where a transition front that joins the high and low ovalization regimes, about one tube diameter long, is seen to propagate away from $s = 0$. We take note of the wavy nature of these profiles and observe that although the waves close to mid-span may be related to the initial geometric imperfection we introduced to the structure (Eq. (4.1)), beyond $s \approx 1.6D$ the tube is initially essentially perfect due to the exponential multiplier of the sinusoidal axisymmetric imperfection (see Fig. 4.2).

To help us further navigate through the events associated with the steady-state propagation of Lüders banding a sequence of deformed configurations with amplified normal displacement (w x 8) has been generated between $0.88 \le \theta_L / L\kappa_1 \le 0.93$ (Fig. 4.13). The sequence shows the initiation and development of a pair of new pockets of bands, one on the tension and one on the compression side. The amplification of w reveals that both the compression (C) and tension (T) sides of the Lüders deformed section of the tube are wrinkled. Furthermore, the wrinkles develop simultaneously with the nucleation of each pocket of bands. Interestingly, for C the center of each pocket of bands coincides with a wrinkle peak and for T with a valley. It appears that as Lüders banding plastically deforms the tube, uniform bending yields to a wrinkled state. This

happens even though the local moment is essentially constant. In other words, *wrinkles form when a certain plastic deformation develops rather than because the critical load is reached as is the case in traditional plastic buckling situations*.

A more quantitative view of the C and T wrinkles and their relationship is shown in Fig. 4.14. Here the normal displacements of the two most deformed generators corresponding to the last image in Fig. 4.13 are plotted against the longitudinal position (undeformed). Following an initial transient at mid-span that is influenced by the initial imperfections in the structure, the two generators are seen to have wrinkled at well-defined wavelength and amplitudes. The half-wavelength is $\lambda = 1.44\sqrt{Dt}$, a value 1.2 times the elastic one for axisymmetric buckling (Eq. (3.2)). The mode is such that the C valleys coincide with T peaks. Furthermore, the C amplitude of $0.076t$ is nearly 2.5 times higher than the T amplitude, something that could be expected due to the opposite signs of the stresses and deformations on the two sides. As in Fig. 4.13, the wrinkling stops at the interface of the Lüders deformed and undeformed zones. We thus conclude that despite their relatively small amplitude the Lüders induced wrinkles result in the waviness of the $\Delta - s$ profiles in Fig. 4.12.

Before leaving this subject it is worth pointing out that the wavelength of these wrinkles was found to be influenced to some degree by the mesh used. Although the other performance criteria were met, switching from two to three elements through the thickness (55,024 vs. 185,706 elements) was found to increase the wavelength by about 5% and remained the same when an even finer mesh of four elements was used.

Returning to Figs. 4.4 and 4.5, the nucleation of new pockets of Lüders bands and wrinkles continues until the whole length of the tube has been deformed to the curvature of $1.36L\kappa_1$. This corresponds to the end of the moment plateau in Fig. 4.4, which interestingly terminates with a small moment dip (probably due to the interaction of the

bands with the free end of the tube). As can be seen in Fig. 4.4, the end of the moment plateau compares very well with the corresponding event in the experimental response. The completion of the propagation phase of the process is also depicted in the $\theta(s)$ and $\Delta(s)$ trajectories in Figs. 4.11 and 4.12.

Subsequently, the moment starts to increase monotonically again and the tube deforms uniformly. Thus, in configuration ⑦ in Fig. 4.5 at $\kappa = 1.40\kappa_1$ the tube is seen to be uniformly bent and to have a linear $\theta(s)$ trajectory in Fig. 4.11. The same can be said for configurations ⑧ and ⑨ at curvatures of $1.60\kappa_1$ and $\kappa = 1.80\kappa_1$ respectively. The ovalization in turn becomes nearly uniform (see ⑦ in Fig. 4.12). The additional ovalization that is induced during this second stable part of the bending history gradually reduces its bending rigidity leading to the attainment of a limit moment at a curvature of $1.91\kappa_1$. Beyond this point, deformation localizes at mid-span by diffuse ovalization, which under persistent bending turns into an increasingly sharper local inwards kink.

4.2.2 D/t = 24.26, $\Delta\varepsilon_L$ = 2.55%

It is now interesting to contrast the results above with results for LU3-3 with approximately the same geometry but with a longer Lüders strain of 2.55% (see Table 4.1). The stress-strain response adopted is shown in Fig. 4.15 along with the measured response. The calculated moment-end rotation response is shown in Fig. 4.16 and a sequence of deformed configurations in Fig. 4.17. The slope profiles $(\theta - s)$ of the chosen configurations are shown in Fig. 4.18 and the ovalization profiles $(\Delta - s)$ in Fig. 4.19. The initial part of the response is similar to that of the previous case. Configuration ①, just before the moment maximum, is uniformly deformed and this is reflected in the $\theta(s)$ and $\Delta(s)$ profiles. A moment maximum of $1.09M_o$ develops following which Lüders banding nucleates again at mid-span due to the local imperfection introduced to the

model. The subsequent moment plateau again hovers around M_o as indeed is the level of the experimental response. The inclined banded nature of the Lüders deformation appears similar to that in Fig. 4.5. Curvature localizes and so does the ovalization as evidenced by the $\theta(s)$ and $\Delta(s)$ profiles in Figs. 4.18 and 4.19. The low curvature regime is at $0.15\kappa_1$ while the higher curvature does not quite stabilize, instead increasing from $1.66\kappa_1$ to $2.04\kappa_1$. Clearly, however, the longer $\Delta\varepsilon_L$ induces a significantly larger curvature to the Lüders deformed part of the tube than in the previous case. The plastic deformation promotes ovalization as clearly seen in Fig. 4.19 where the ovalization in the neighborhood of the mid-span is seen to grow to much higher values than those of the previous case in Fig. 4.12. Signs of spreading of ovalization along the length can be seen in the profiles of points ③ to ⑦. However, unlike the previous case, Δ at mid-span never stops growing.

Lüders banding also induces wrinkling in the same general fashion as described for LU9-1 (see Fig. 4.20). The wrinkle half-wavelength is now $1.27\sqrt{Dt}$ that is 13% shorter than the previous case while the amplitudes of the C wrinkles are larger, presumably because of the larger curvature induced by the longer $\Delta\varepsilon_L$. Once again, this wavelength was found to grow slightly when a finer mesh with 3 elements through the thickness was used instead.

By configuration ⑦ approximately two-thirds of the tube have been Lüders deformed. This section is bent to the higher curvature, is ovalized but not so uniformly, and is wrinkled. Soon thereafter, the moment takes a downward trajectory and the tube starts to collapse. The collapse is associated with diffuse localized ovalization affecting a zone $(5-6)D$ long at mid-span as can be seen in configurations ⑧ and ⑨ in Fig. 4.17 and in the corresponding $\Delta(s)$ profiles in Fig. 4.19. The collapsing zone develops an even higher curvature that is depicted in Fig. 4.18. Clearly, the combination of higher

curvature and the continued growth of ovalization induced to this section cannot be sustained and this leads to collapse. It also appears that collapse takes place when a certain critical length of the structure is affected by the higher curvature and ovalization. Here collapse occurred at $\theta_L / L\kappa_1$ of approximately 1.47, which compares with the value of 2.04 that would have been achieved if the whole length could have been Lüders deformed. In summary, the simulation replicates the behavior observed in the experiment and explains the reasons behind the premature collapse. Apparently, the longer Lüders strain has lead to the premature collapse of the structure. Figure 4.21 shows an image of the localized mode at collapse that develops. A sharp inwards kink is seen at mid-span (plane of symmetry) and small amplitude wrinkles on either side of it.

4.3 Summary of Results of Simulations of Additional Experiments

The material parameters, the mesh and rate exponent found to reproduce with accuracy the behavior observed in the two bending experiments analyzed this far were adopted to numerically simulate the rest of the experiments presented in Chapter 3 (individual parameters listed in Table 4.1). The amplitude of the imperfection, *a*, was individually selected guided by measured variations in the diameter of each tube (see Table 4.1). To avoid repetition, here we will show only the calculated moment-rotation responses. The results for the five additional cases are compared to the corresponding experimental ones in Figs. 4.22.

The calculated response for the highest *D/t* of 33.19 shown in Fig. 4.22a is seen to agree well with the experimental one. This includes the level of the moment plateau and the point at which the tube collapsed. The same is true for *D/t* = 26.72 (Fig. 4.22b) in which the larger curvature regime spread much further before the tube collapsed. As will be demonstrated in the parametric study that follows in Chapter 5, both of these tubes are

relatively thin and would have collapsed before a second stable branch is reached even if the Lüders strain was shorter.

Figures 4.22c and 4.22d show results from tubes with *D/t* of about 18.6. LU5-3 with $\Delta\varepsilon_L = 2.71\%$ did not survive the inhomogeneous phase of bending while LU4-3 with a shorter Lüders strain of 1.78% did. The simulations reproduce these behaviors in all aspects.

The thickest tube tested with *D/t* = 14.68 and $\Delta\varepsilon_L = 2.43\%$ (Fig. 4.22e) survived the inhomogeneous phase of bending and was bent uniformly to a large curvature of about $2\kappa_1$. Again, all aspects of the response were captured by the simulation. For such a low value of *D/t*, the tube would survive even if the Lüders strain was longer.

The tubes developed wrinkles for all seven simulations. In the experiments, we reported a significant variation in the measured wavelengths with the most commonly occurring values being close to λ_e given in Eq. (3.2). In the simulations, the wavelength varied somewhat from case to case. Interestingly, for all but the thickest tube, the calculated half wavelengths were close to λ_e (varied between $1.0\lambda_e$ and $1.2\lambda_e$). In other words, we did not detect any strong influence on the wavelength from $\Delta\varepsilon_L$. For *D/t* = 14.7 the value was $0.8\lambda_e$. On the other hand, for a given *D/t*, longer Lüders strain results in higher localization curvature, which in turn, increases the amplitude of the induced wrinkles (compare C wrinkles in Figs. 4.14 and 4.20). Finally, the regularization was instrumental in producing the steady-state propagation of curvature, which is also responsible for the periodicity described here.

4.4 Tubes with a Monotonic Stress-Strain Response

For comparison purposes the bending response of a tube with the same geometry as those considered in section 4.2, but with a monotonic stress-strain response, was

calculated. The stress-strain response used was generated by simply eliminating the Lüders plateau from the response in Fig. 4.3. In practice, this might be achieved by cold working the pipe (e.g., cold rolling). The resultant stress-strain response is shown in Fig. 4.23. The calculated moment-curvature response for the tube with D/t = 24.31 is shown in Fig. 4.24. The monotonicity of the stress-strain response results in an initially monotonic $M-\kappa$ response and a corresponding monotonically growing and uniform curvature as shown in configurations ① to ④ in Fig. 4.25. The induced ovality gradually reduces the bending stiffness and leads to a limit moment at $\kappa = 1.69\kappa_1$, after which the tube collapses (conf. ⑤ in Fig. 4.25) in the manner shown earlier in Fig. 4.21. Included in the figure is the $M-\kappa$ response for LU9-1 whose material exhibited a Lüders strain of 1.89%. Interestingly, following the initial inhomogeneous bending phase, this tube was bent uniformly up to a curvature of $1.91\kappa_1$. This implies that the Lüders banding did not influence adversely the extent to which the pipe could be bent.

Exp. No.	D in (mm)	t in (mm)	$\frac{D}{t}$	E Msi (GPa)	σ_L ksi (MPa)	$\frac{\Delta\sigma}{\sigma_L}$	$\frac{-E'}{E}$	$\Delta\varepsilon_L$ %	a %
LU11-1	1.255 (31.88)	0.0378 (0.961)	33.19	30.5 (210)	51.98 (358.5)	0.275	0.022	2.16	0.04
LU12-1	1.378 (35.01)	0.0516 (1.310)	26.72	29.8 (205)	38.47 (265.3)	0.275	0.016	2.21	0.13
LU3-3	1.253 (31.83)	0.0517 (1.312)	24.26	28.5 (196)	37.28 (257.1)	0.275	0.013	2.55	0.08
LU9-1	1.254 (31.84)	0.0516 (1.311)	24.31	29.9 (206)	36.91 (254.5)	0.306	0.020	1.89	0.15
LU5-3	1.252 (31.81)	0.0674 (1.711)	18.59	29.4 (203)	42.91 (295.9)	0.275	0.015	2.71	0.22
LU4-3	1.252 (31.80)	0.0666 (1.692)	18.80	29.7 (205)	31.85 (219.6)	0.275	0.017	1.78	0.20
LU7-3	1.252 (31.80)	0.0853 (2.166)	14.68	30.6 (211)	44.15 (304.5)	0.275	0.017	2.43	0.10

Table 4.1 Major geometric and material parameters used in the models.

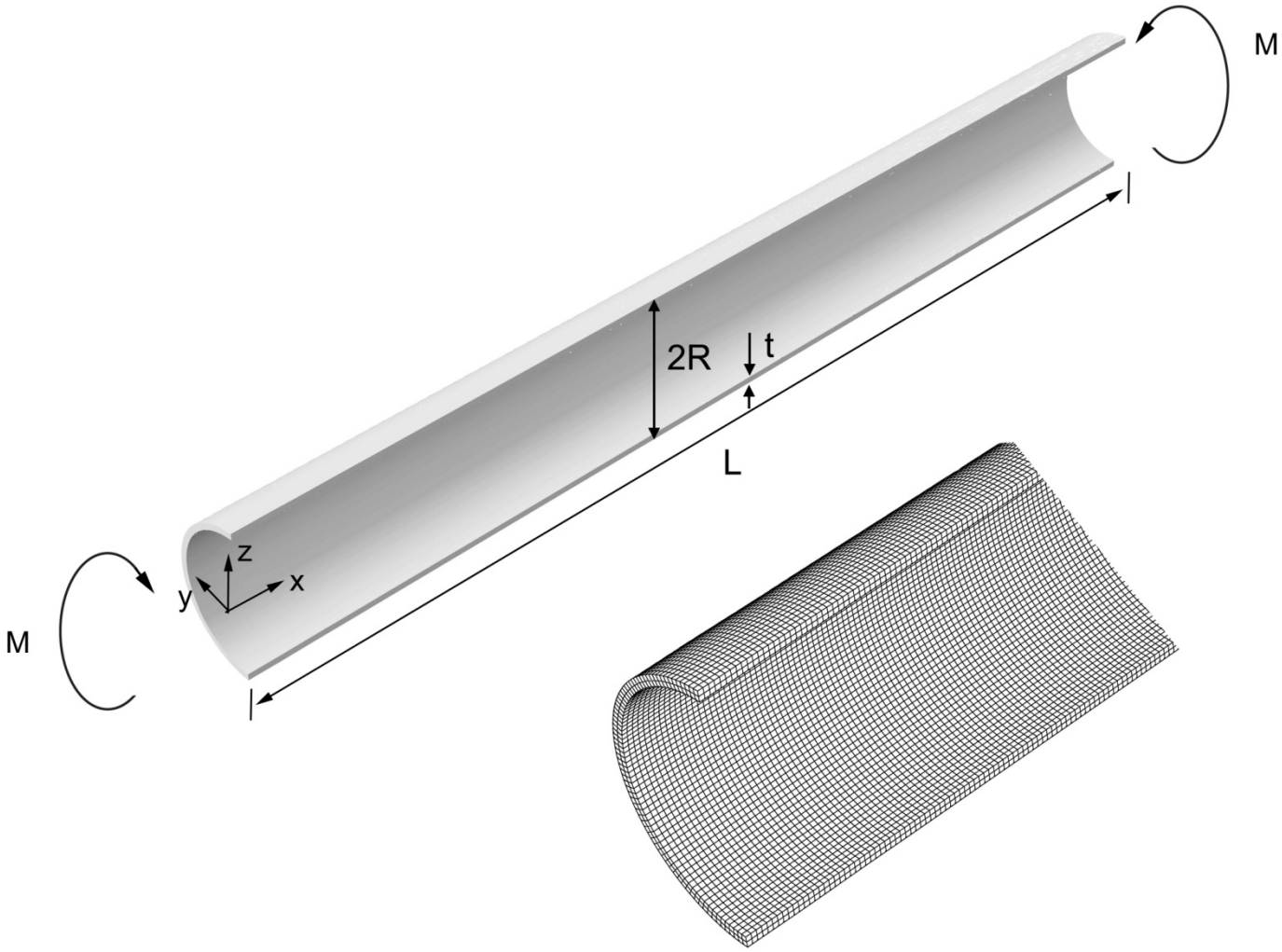

Fig. 4.1 Geometry and mesh of finite element model.

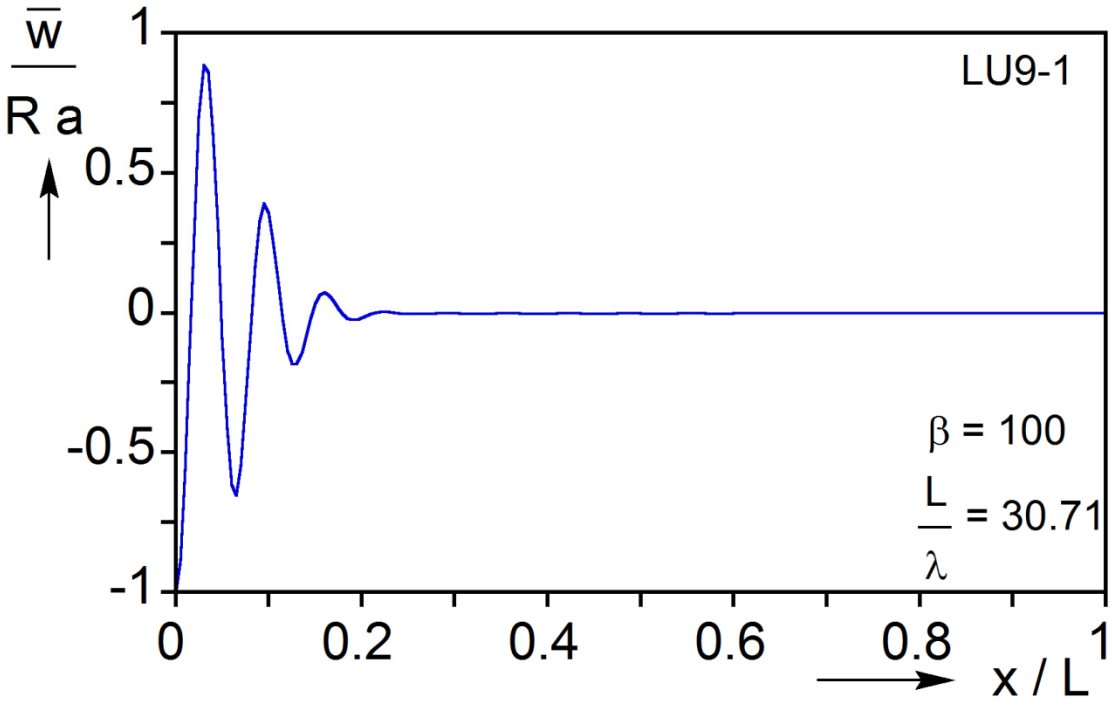

Fig. 4.2 Initial geometric imperfection used (Eq. 4.1). The imperfection affects only 20% of the effective length of the model.

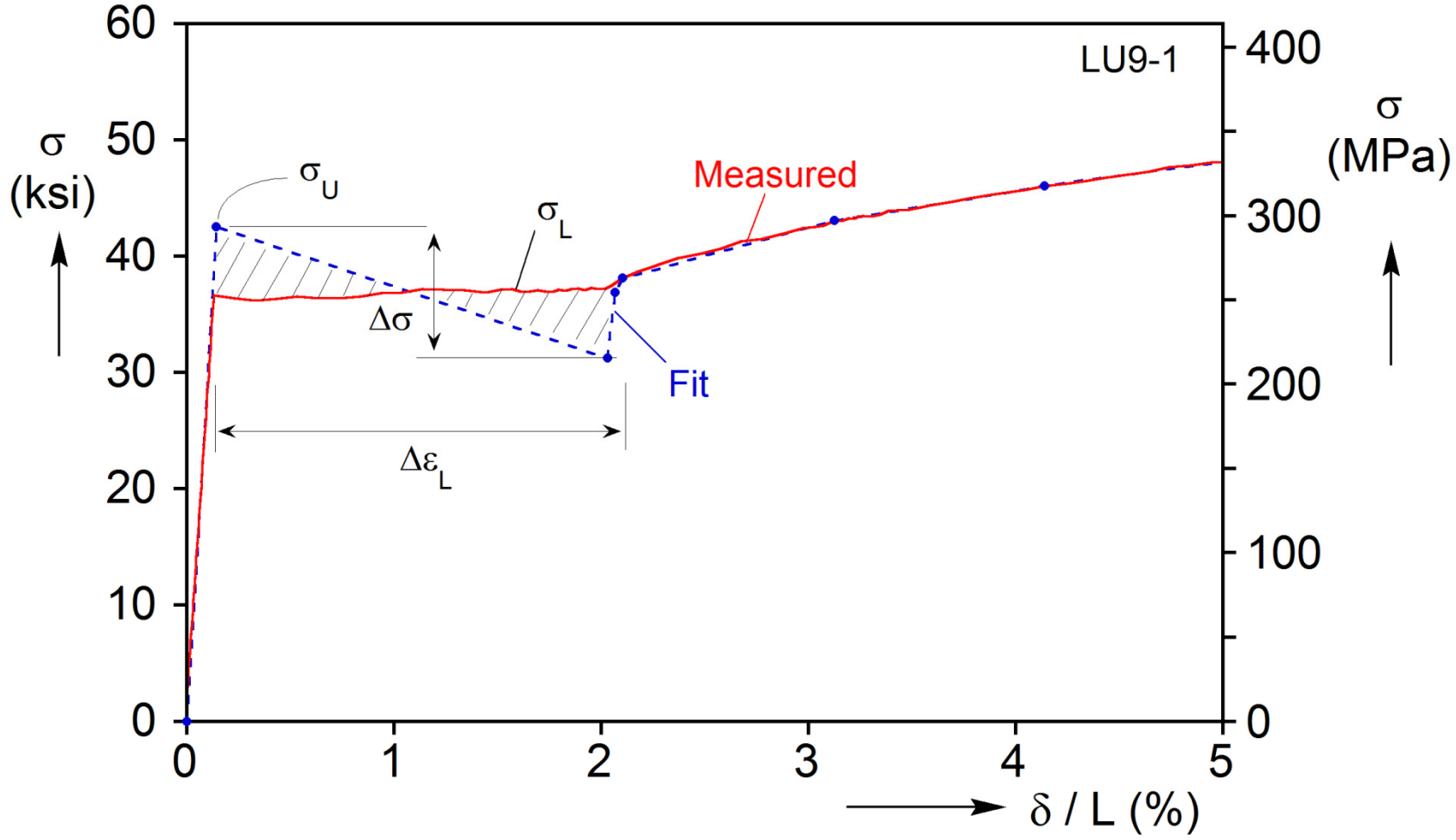

Fig. 4.3 Measured material response and stress-strain response adopted for Exp. LU9-1.

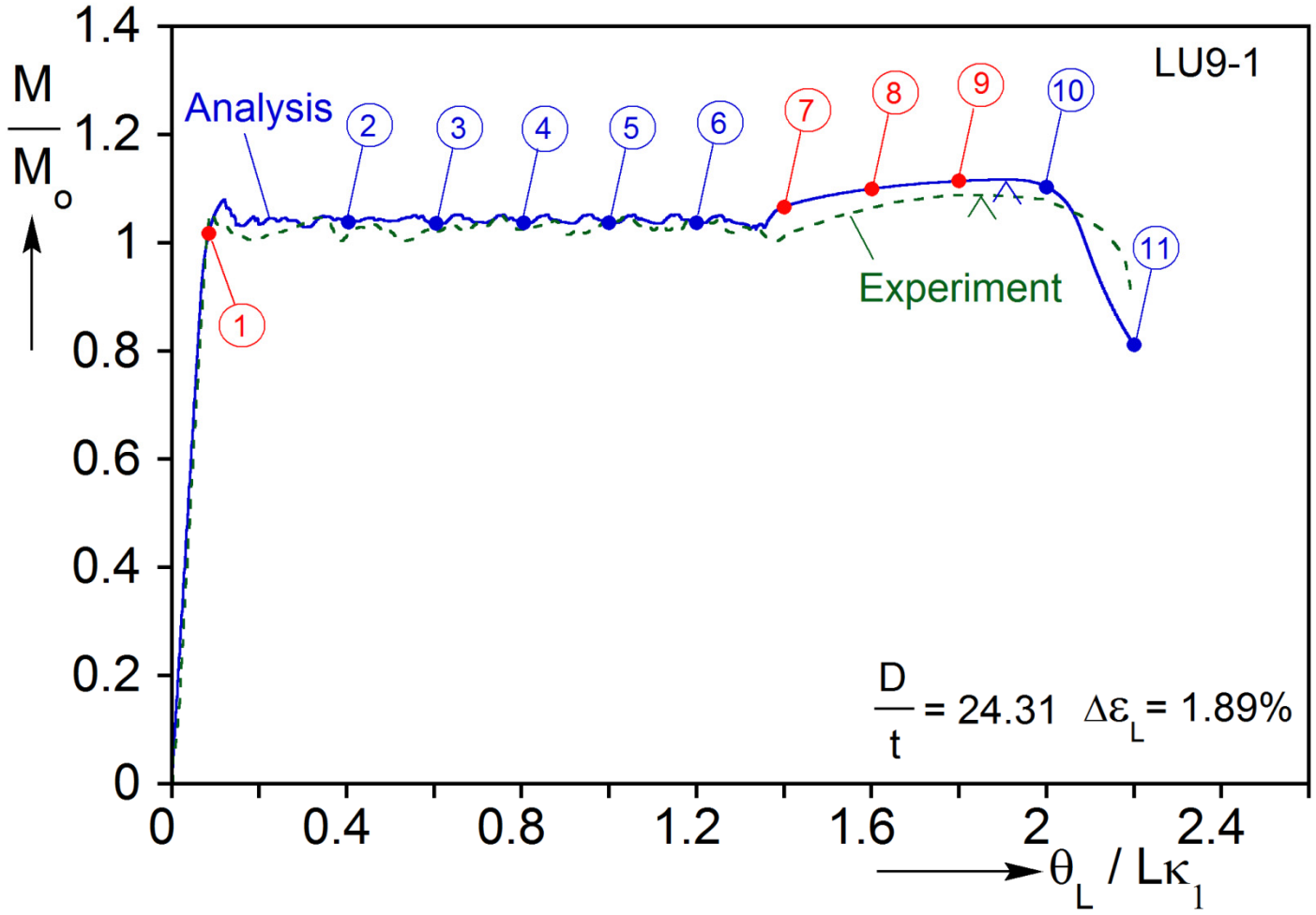

Fig. 4.4 Comparison of measured and calculated moment - end rotation response for Exp. LU9-1.

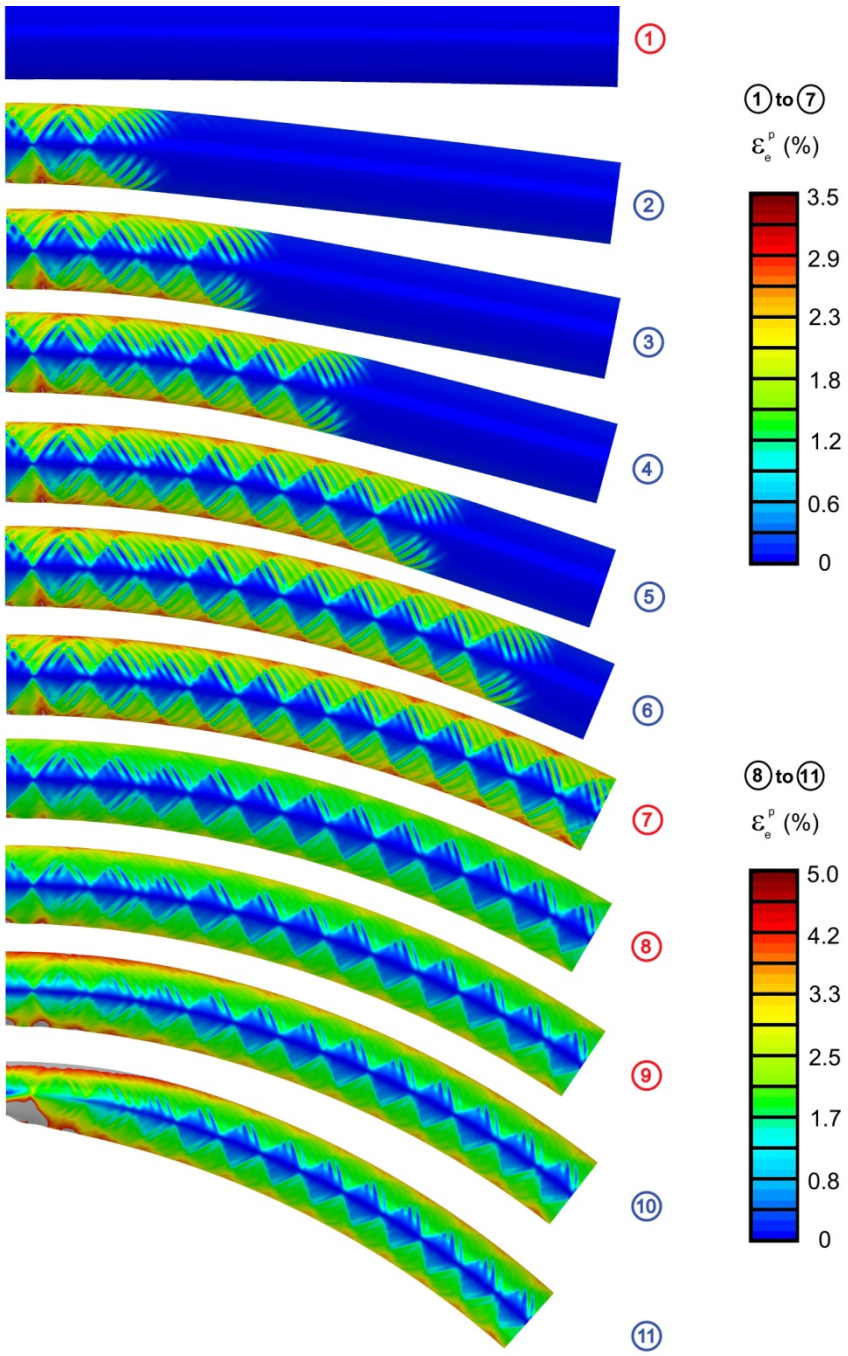

Fig. 4.5 Calculated deformed configurations corresponding to response in Fig. 4.4. Color keys represent the equivalent plastic strain.

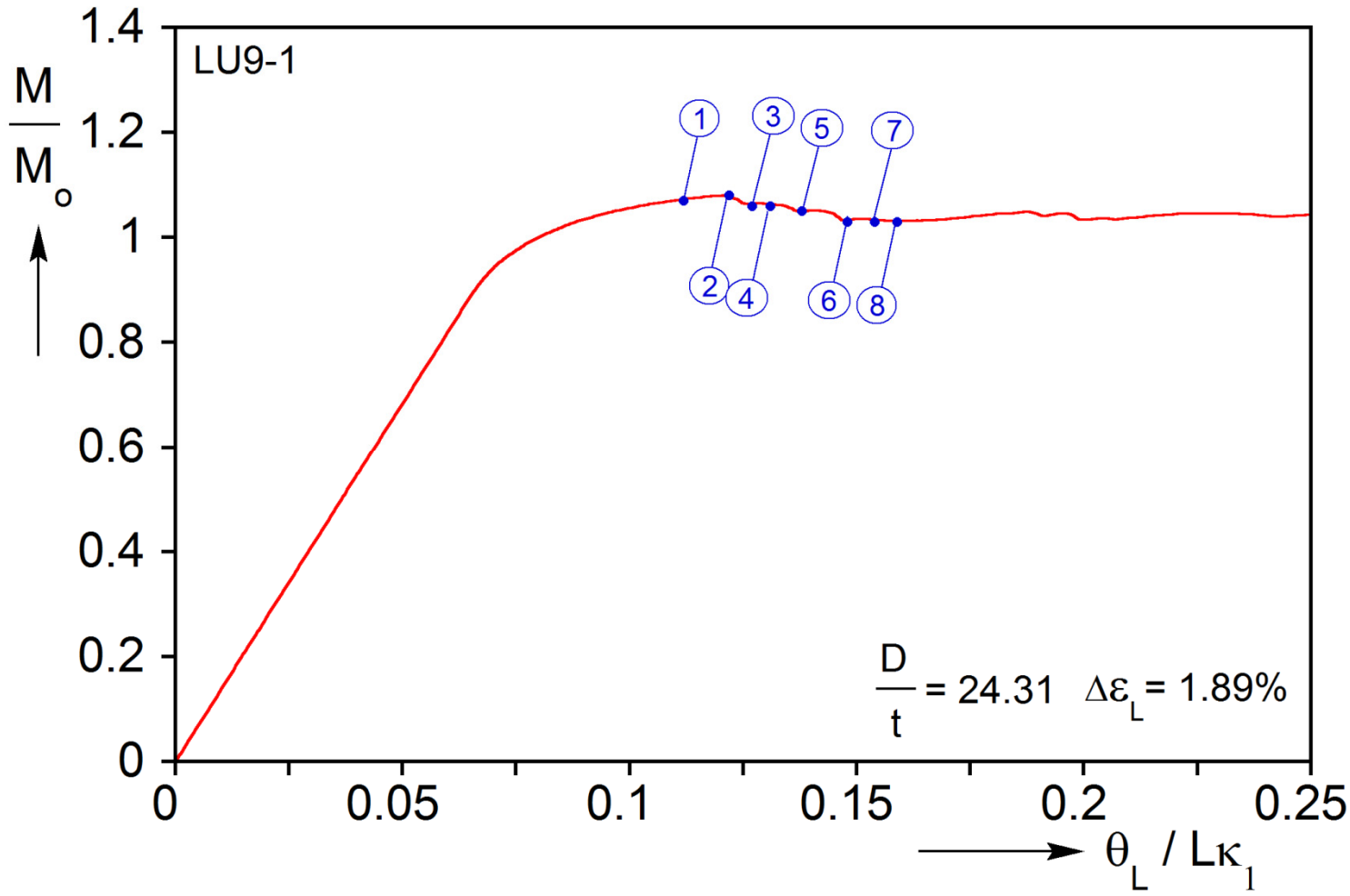

Fig. 4.6 Expanded view of the initial part of the moment - end-rotation response for Exp. LU9-1.

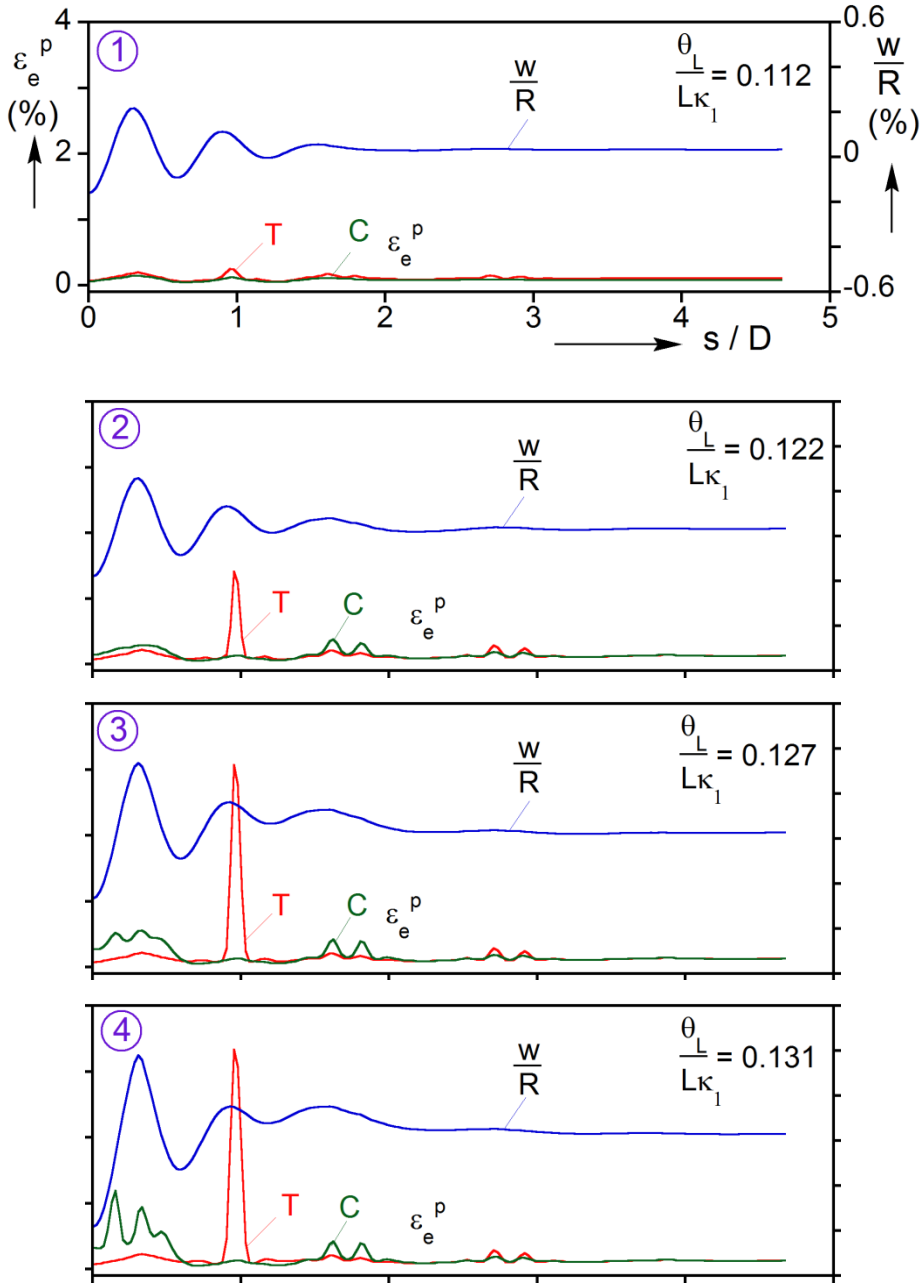

Fig. 4.7 Normal displacement along the most compressed generator of the tube for four points marked on the response in Fig. 4.6. Included are the plastic equivalent strains along the most compressed (C) and tensioned (T) generators.

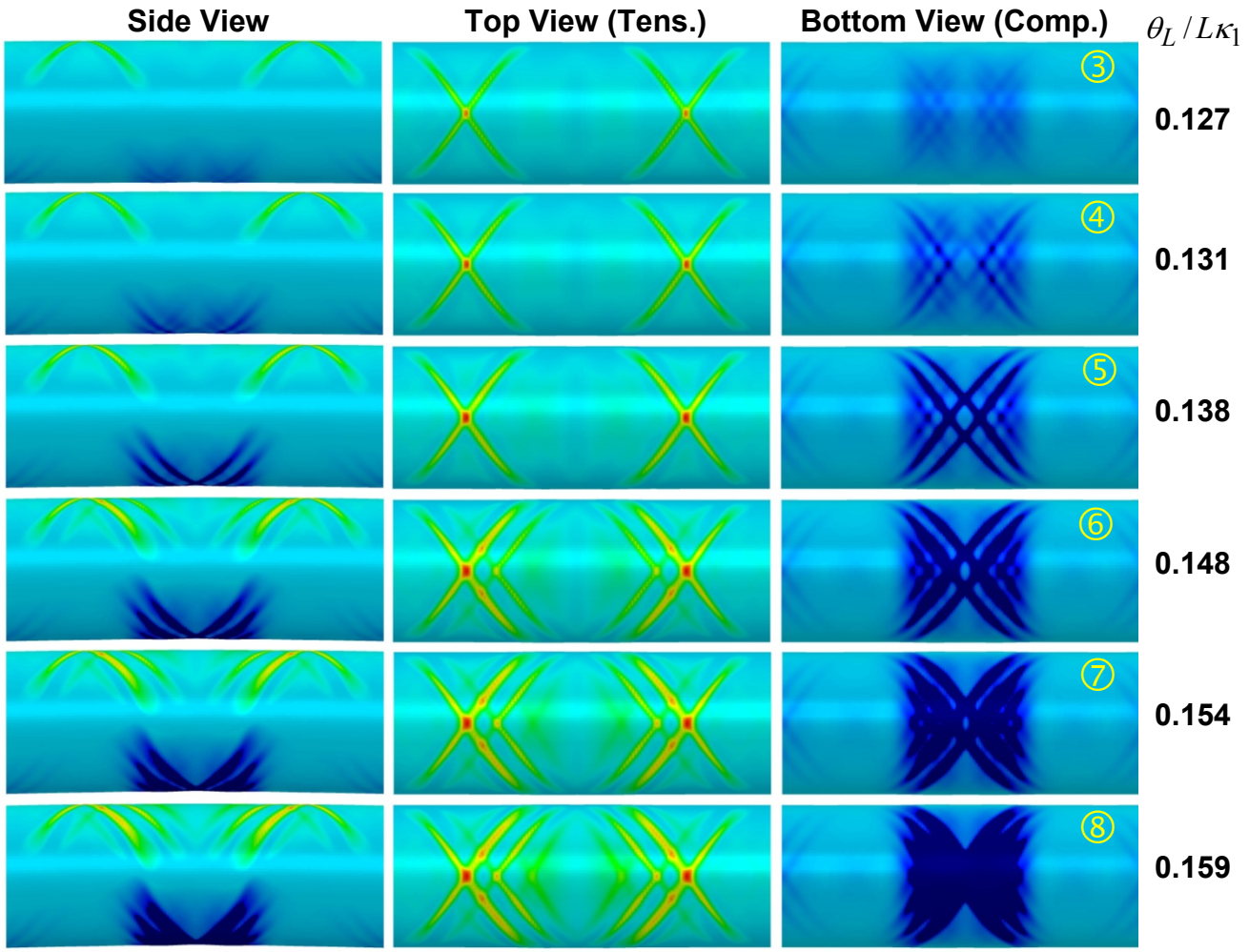

Fig. 4.8 Three views of contours of axial plastic strain for points ③ to ⑧ marked on the response in Fig. 4.6.

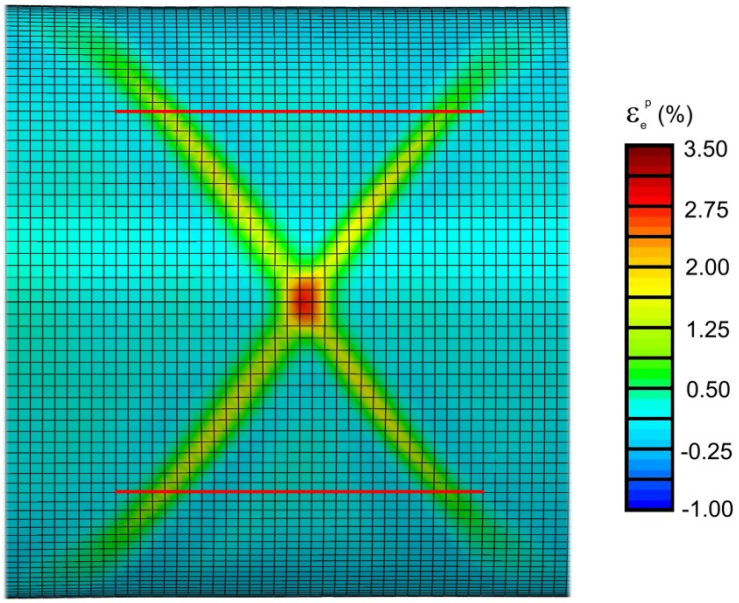

Fig. 4.9 Expanded view of a pair of bands on the tensioned side of the tube corresponding to point ④ on the response in Fig. 4.6.

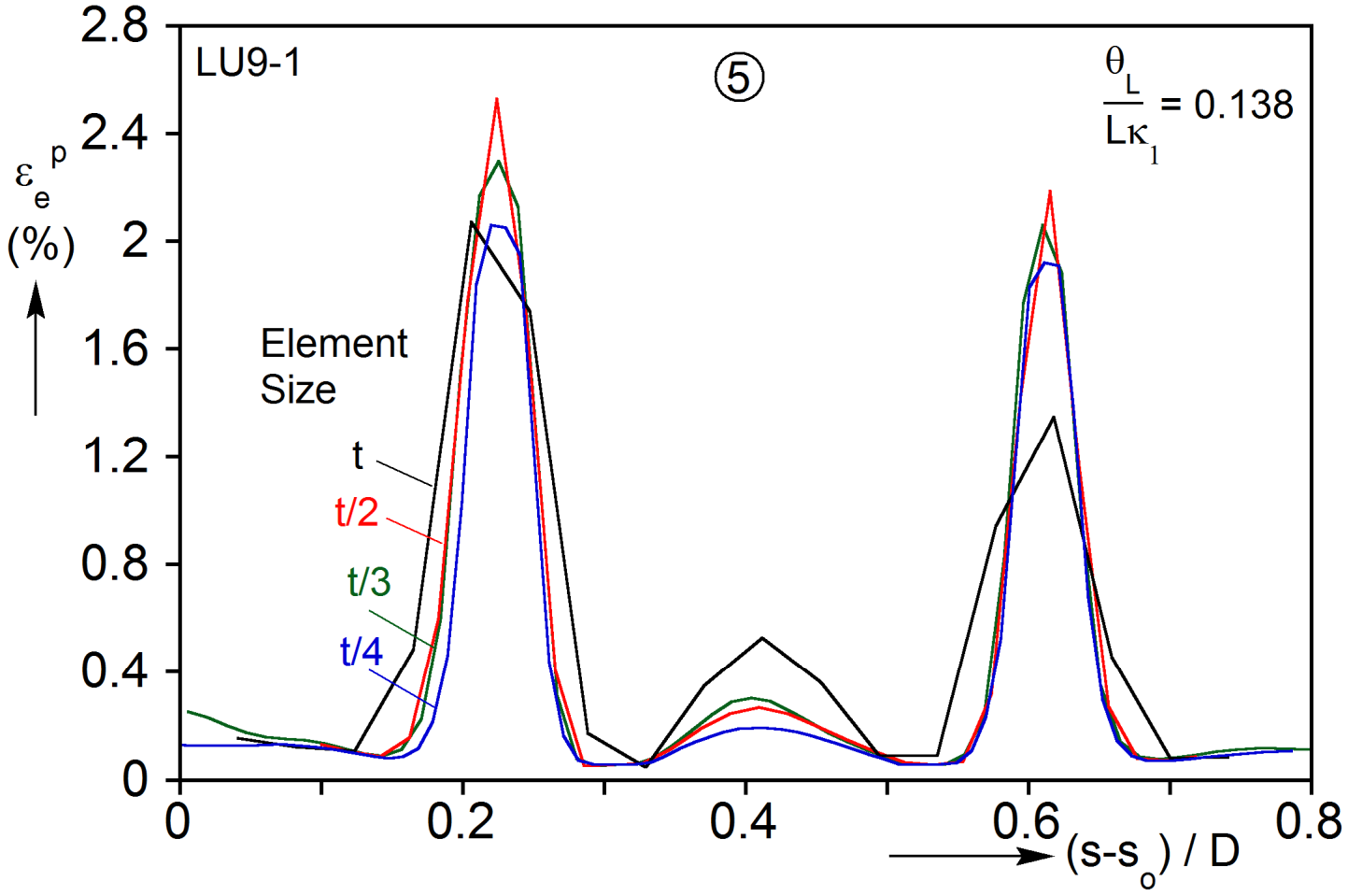

Fig. 4.10 Plots of equivalent plastic strain along the length of the tube corresponding to point ⑤ on the response in Fig. 4.6 for four mesh sizes (strain is along a line 33.2° from the most tensioned generator marked in Fig. 4.9).

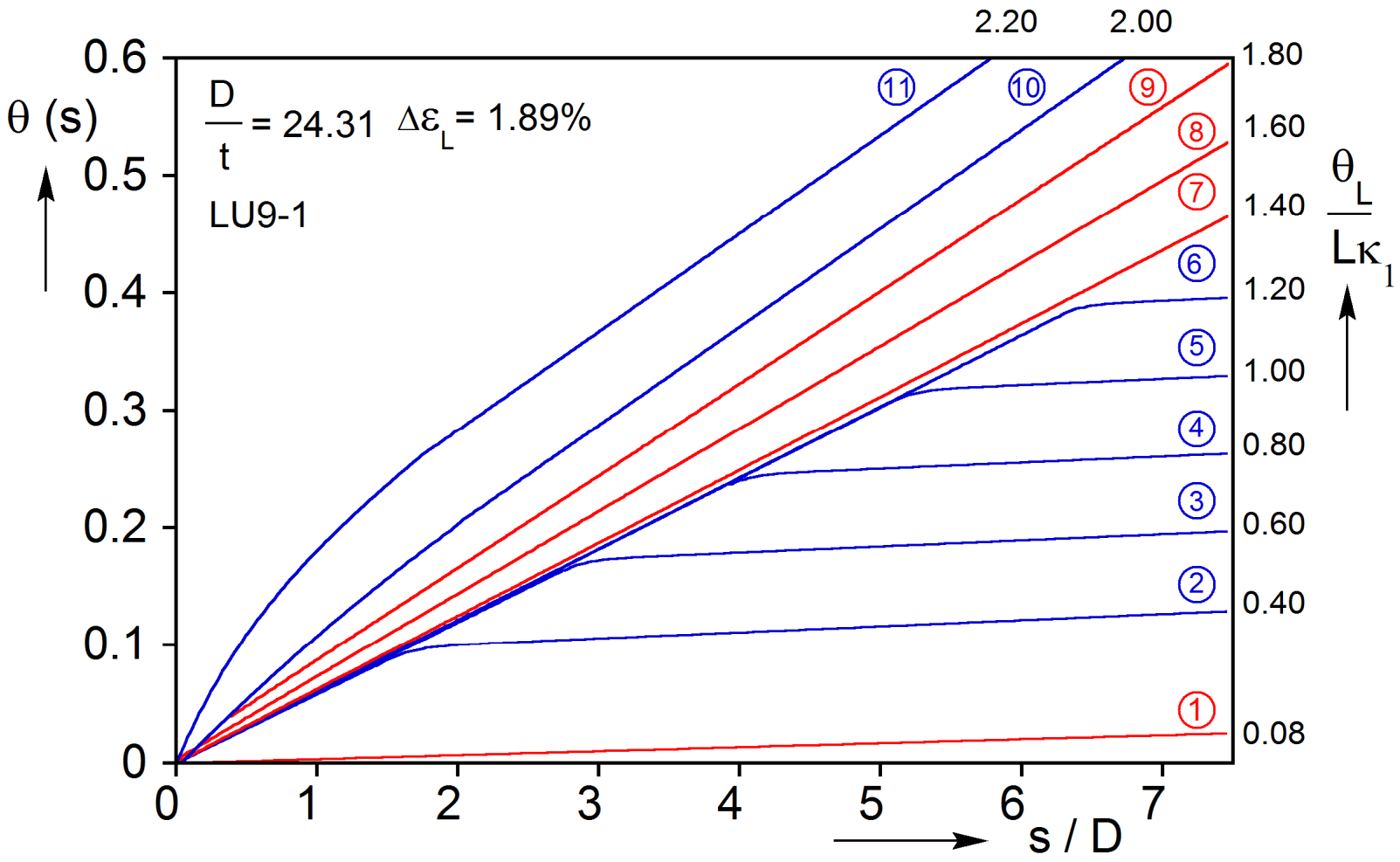

Fig. 4.11 Calculated local tube slope $\theta(s)$ along the length at different end-rotations for LU9-1. Circled numbers correspond to bullets marked on response in Fig. 4.4.

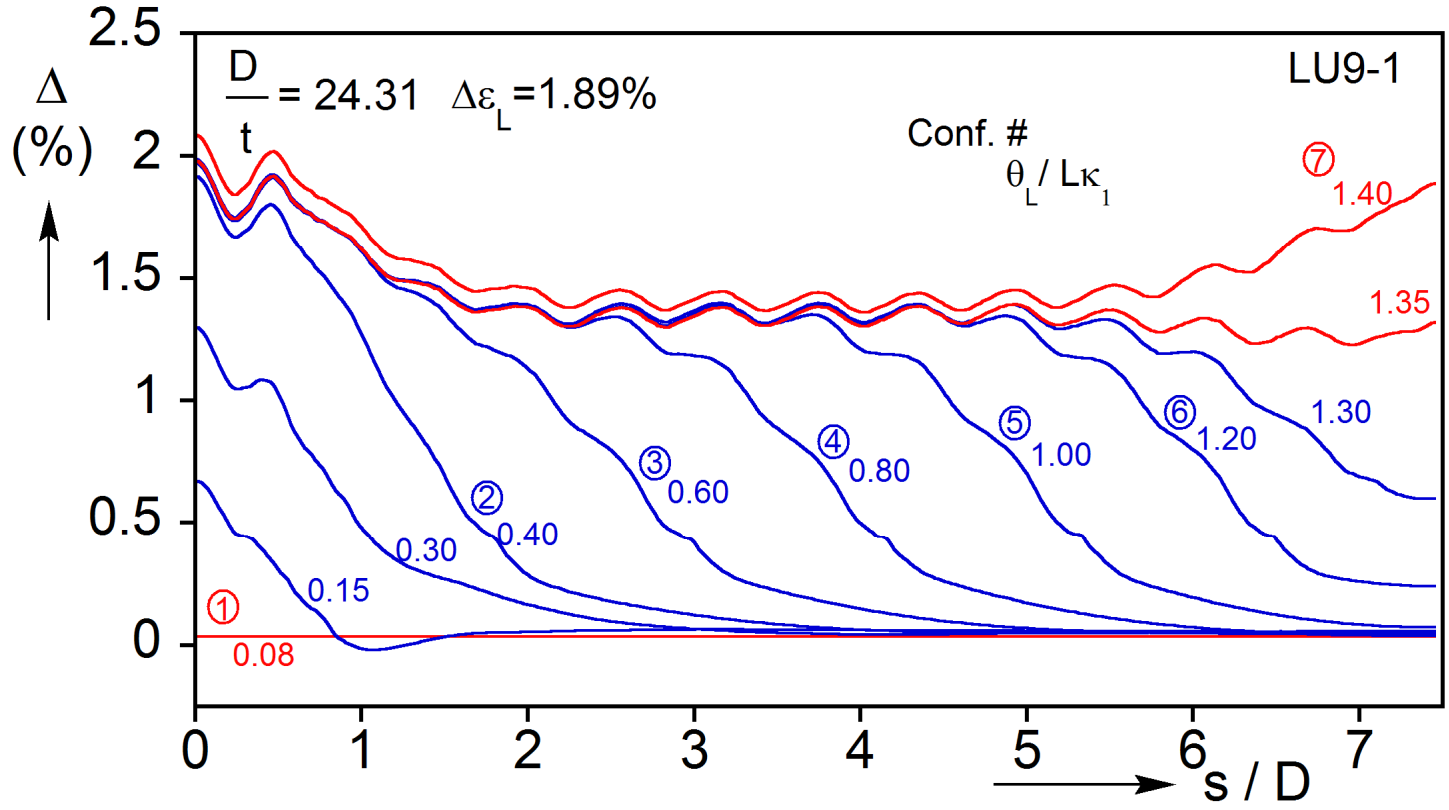

Fig. 4.12 Calculated ovalization along the length of the tube at different end-rotations for LU9-1. Circled numbers correspond to bullets marked on response in Fig. 4.4.

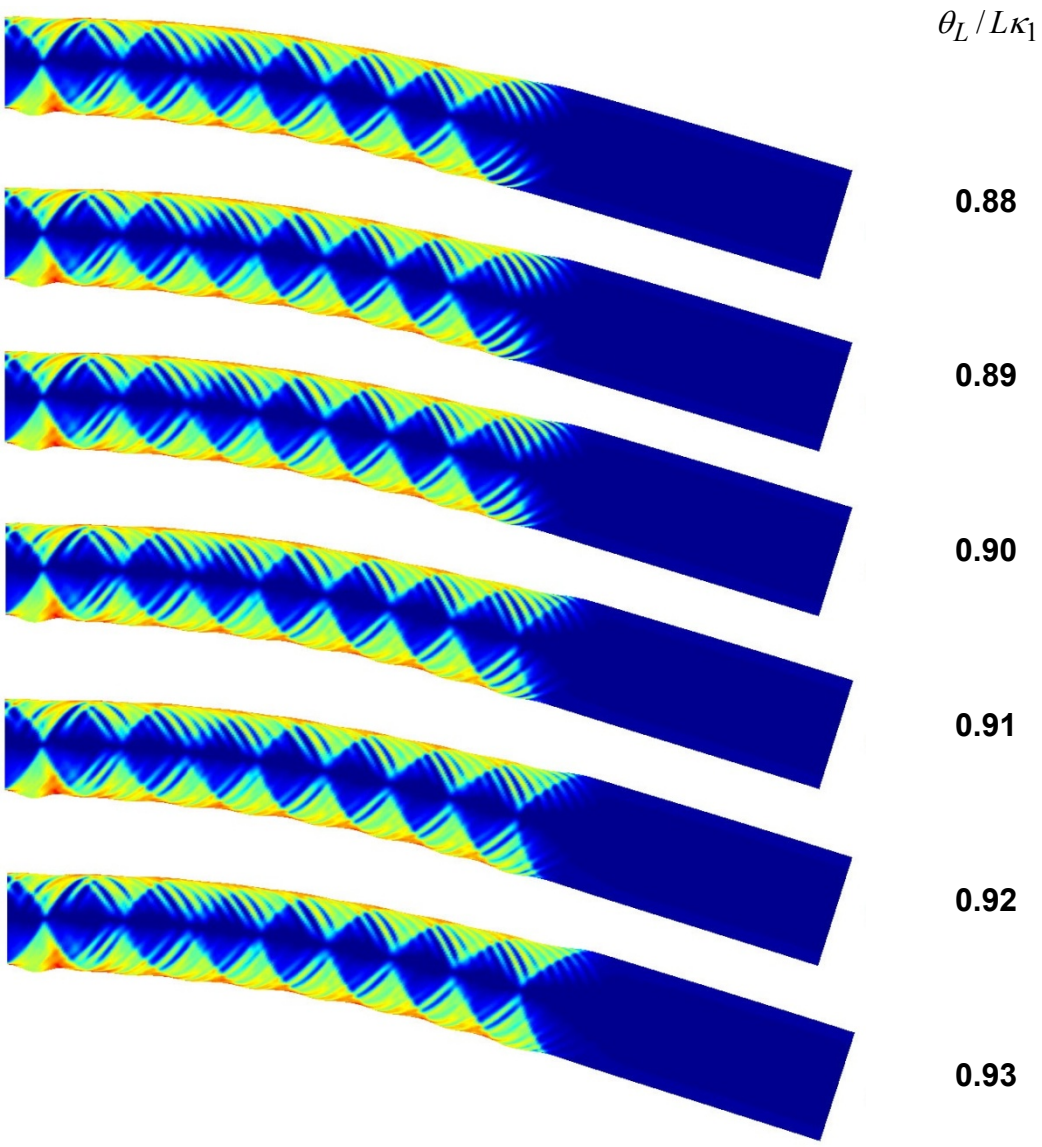

Fig. 4.13 Sequence of deformed configurations with amplified normal displacement for LU9-1.

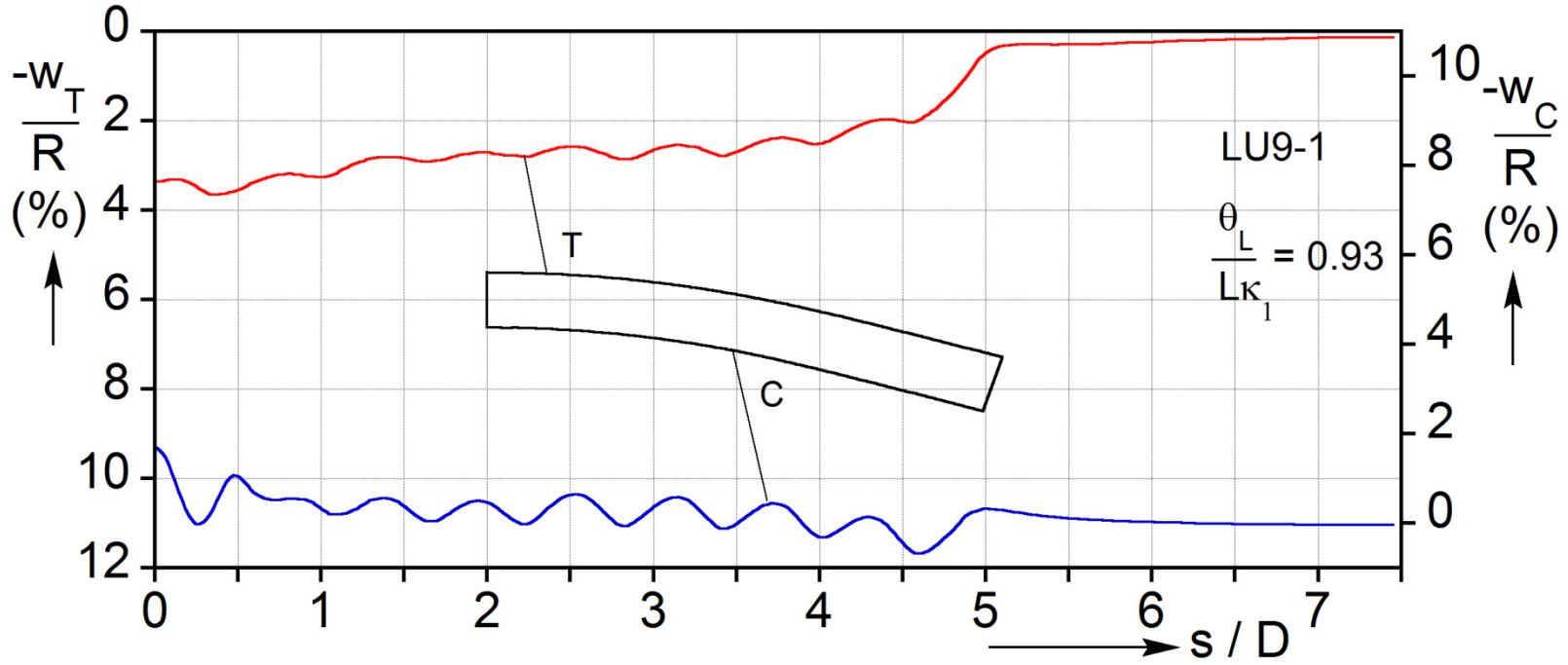

Fig. 4.14 Normal displacements of the two most deformed generators corresponding to the last configuration in Fig. 4.13.

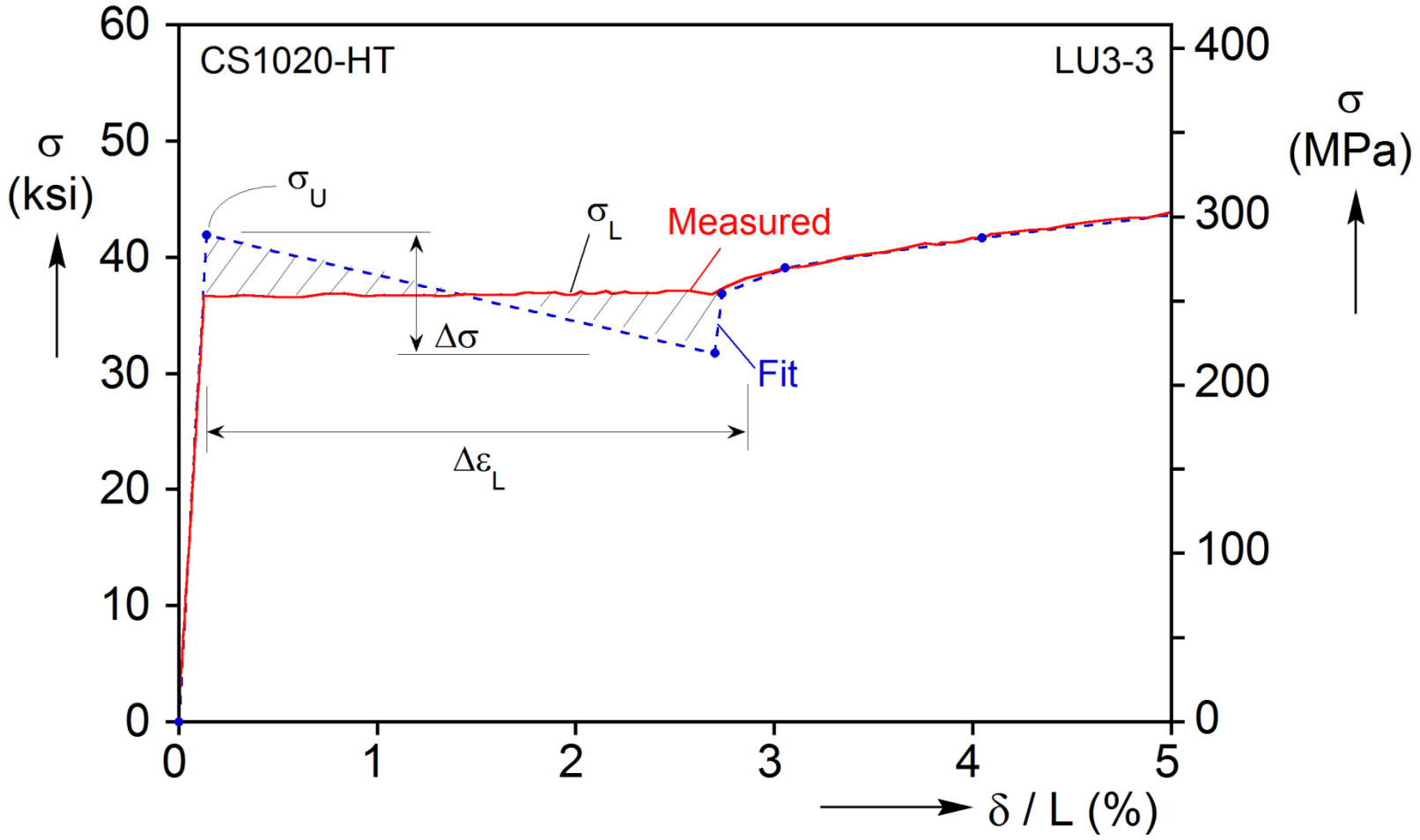

Fig. 4.15 Measured material response and stress-strain response adopted for Exp. LU3-3.

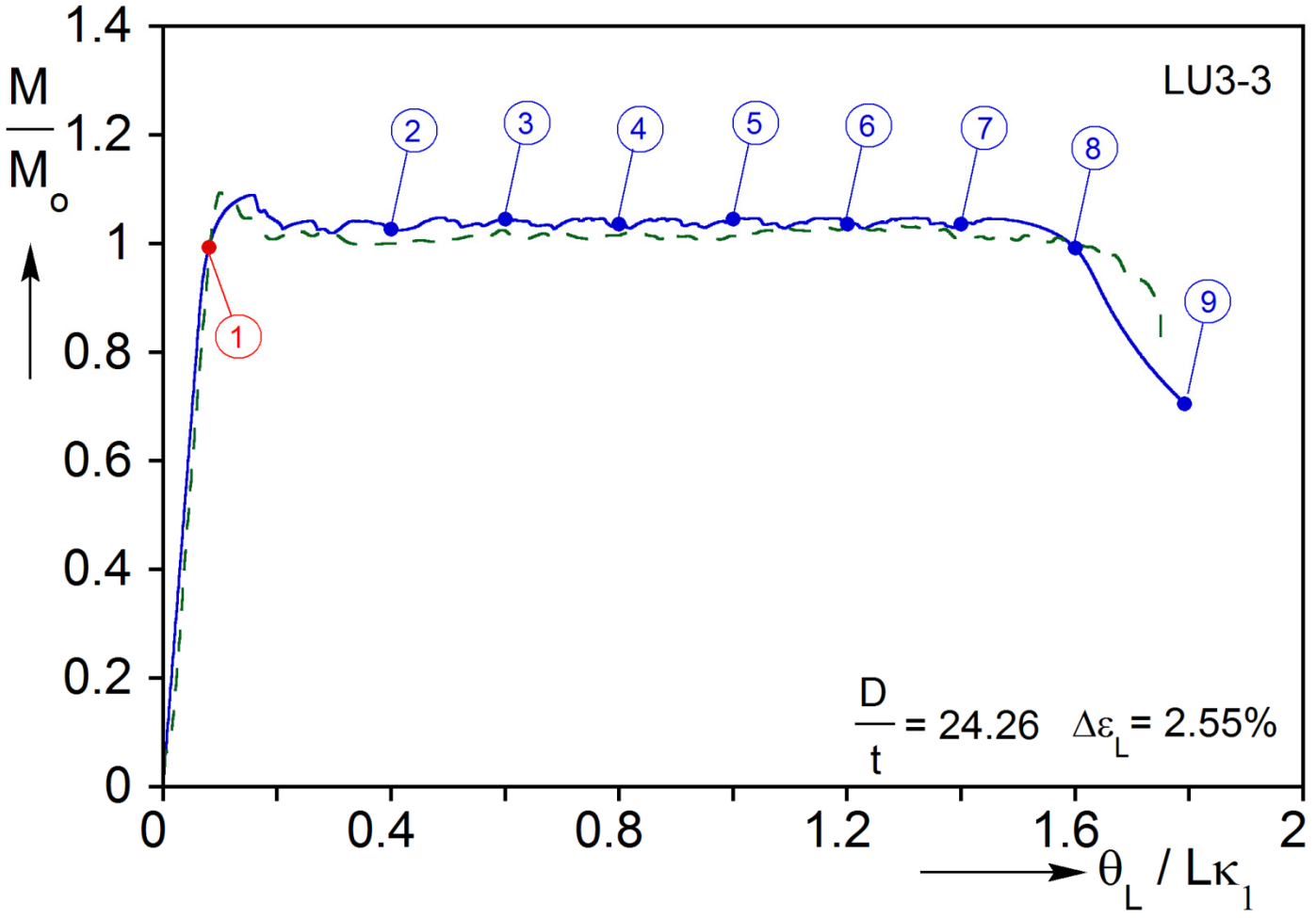

Fig. 4.16 Comparison of measured and calculated moment - end-rotation response for Exp. LU3-3.

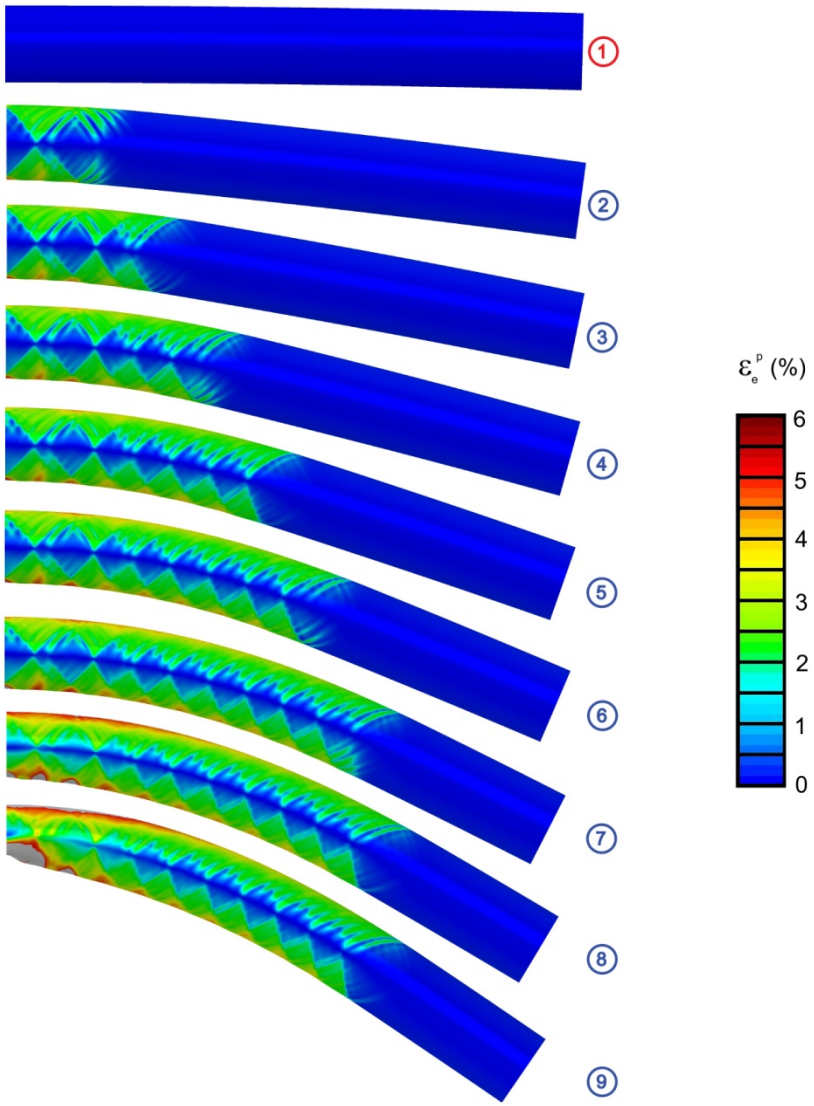

Fig. 4.17 Calculated deformed configurations corresponding to response in Fig. 4.16.

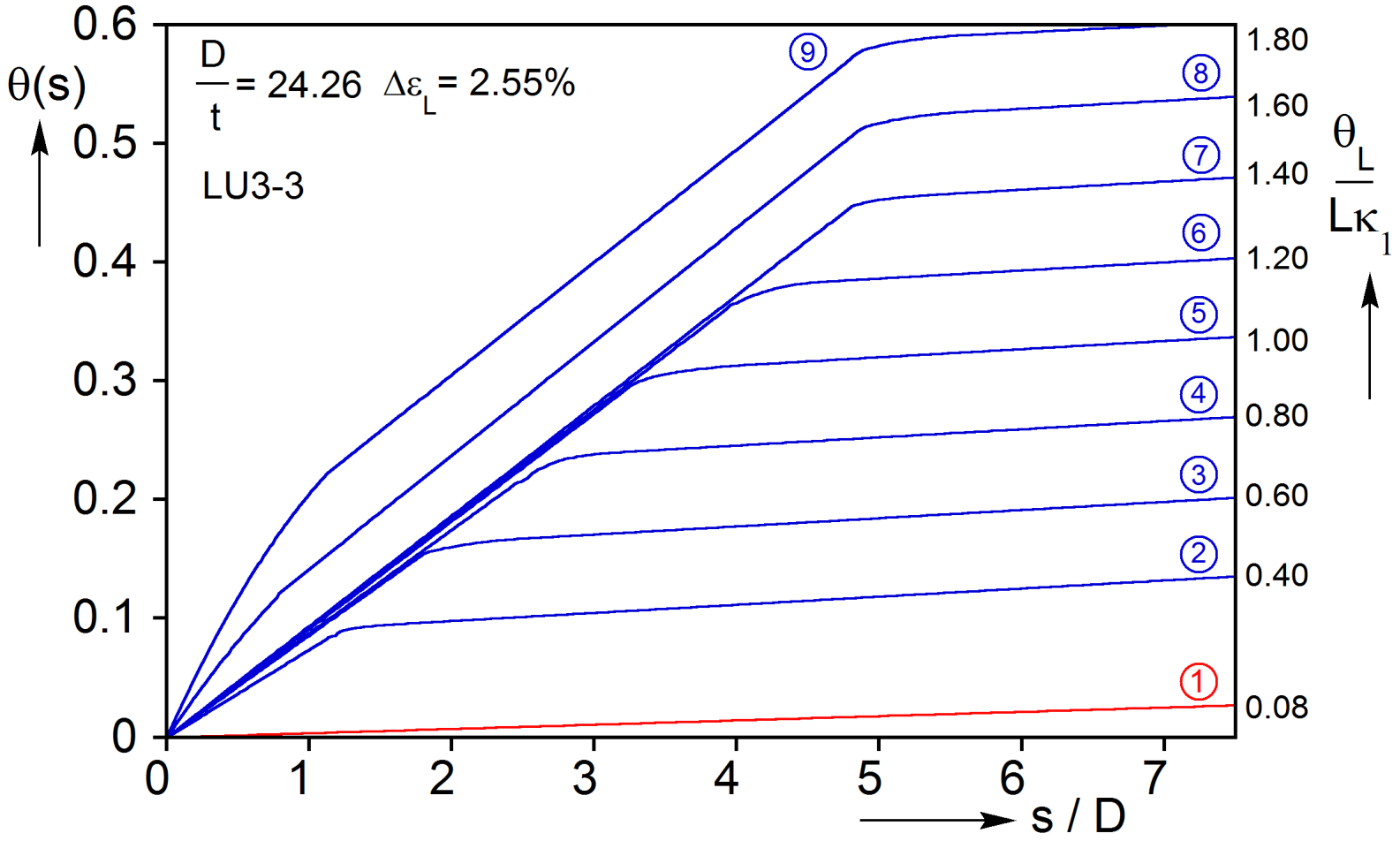

Fig. 4.18 Calculated local tube slope $\theta(s)$ along the length at different end-rotations for LU3-3. Circled numbers correspond to bullets marked on response in Fig. 4.16.

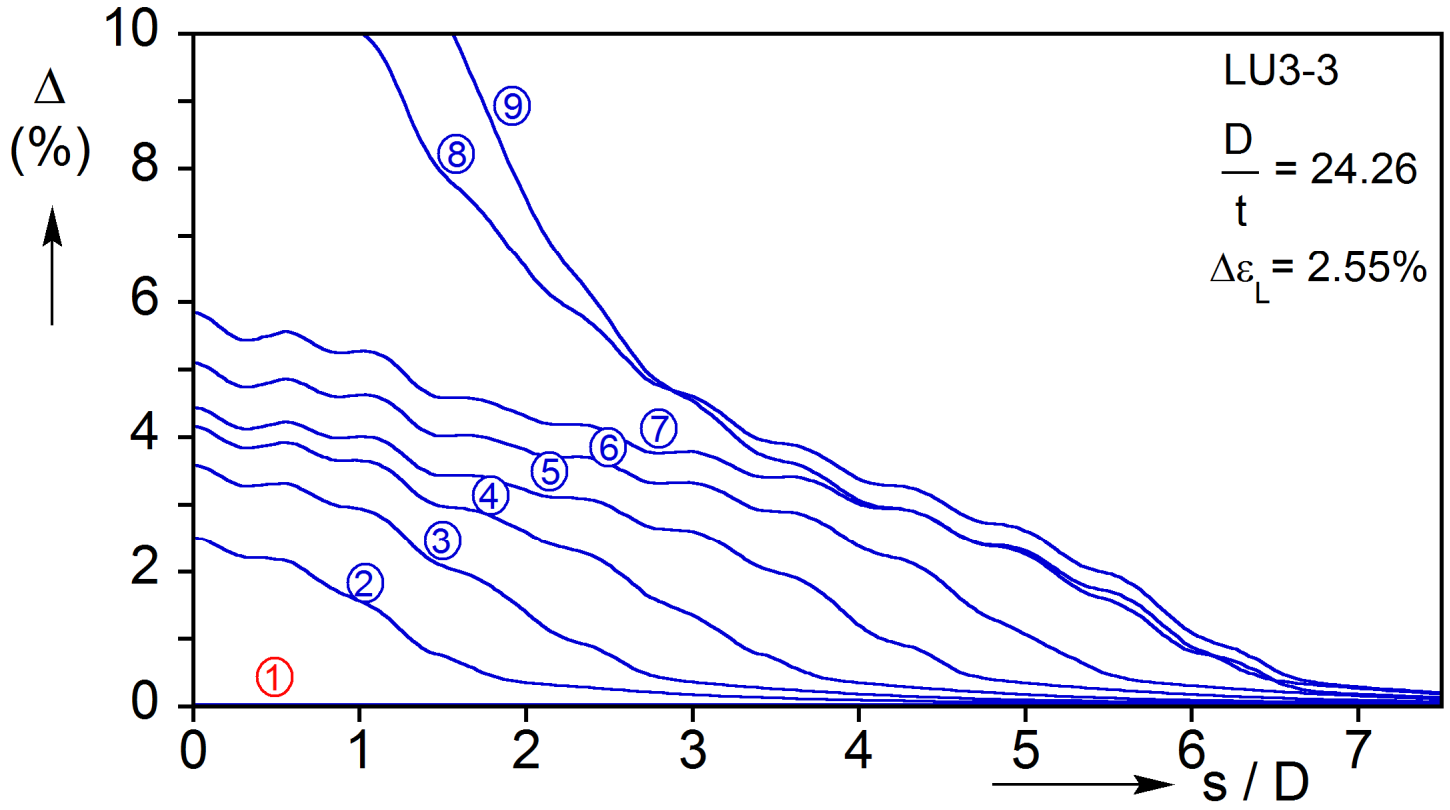

Fig. 4.19 Calculated ovalization along the length of the tube at different end-rotations for LU3-3. Circled numbers correspond to bullets marked on response in Fig. 4.16.

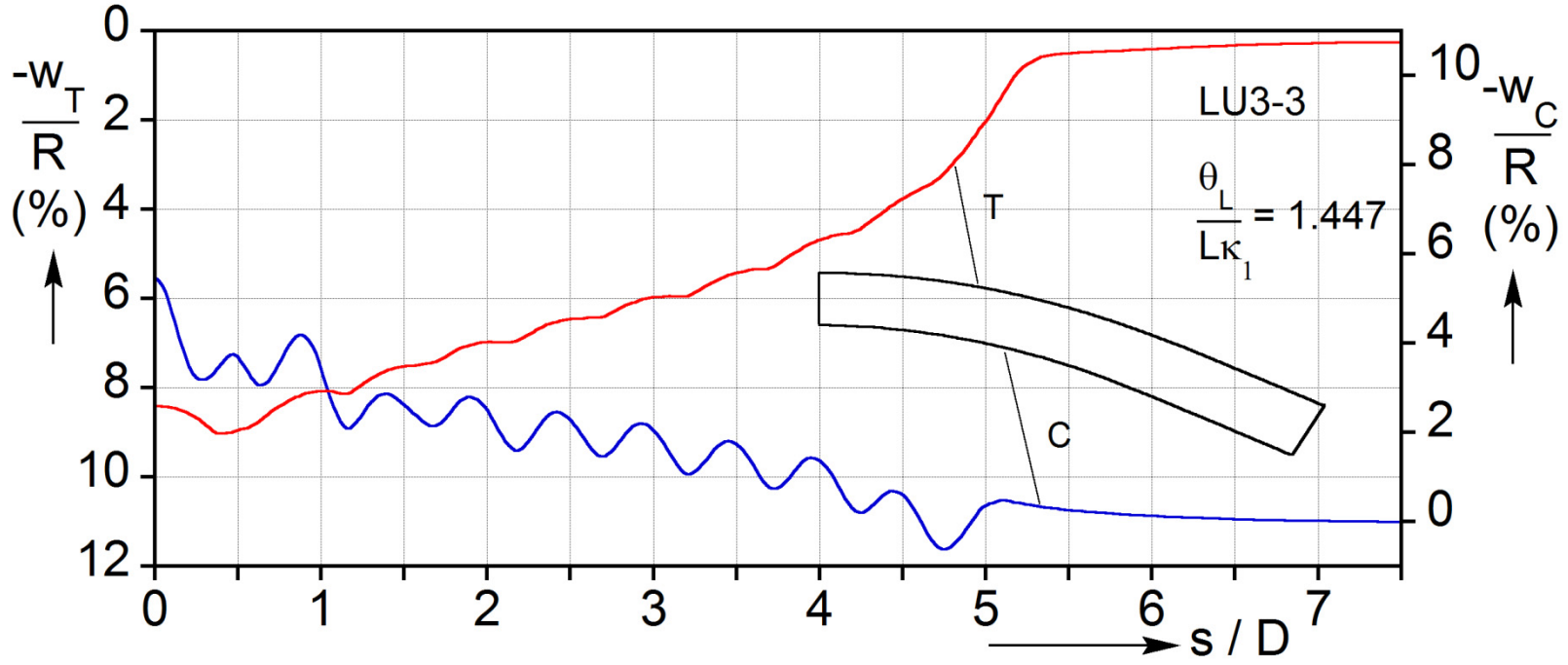

Fig. 4.20 Normal displacements of the two most deformed generators for LU3-3 for $\theta_L = 1.447 L\kappa_1$.

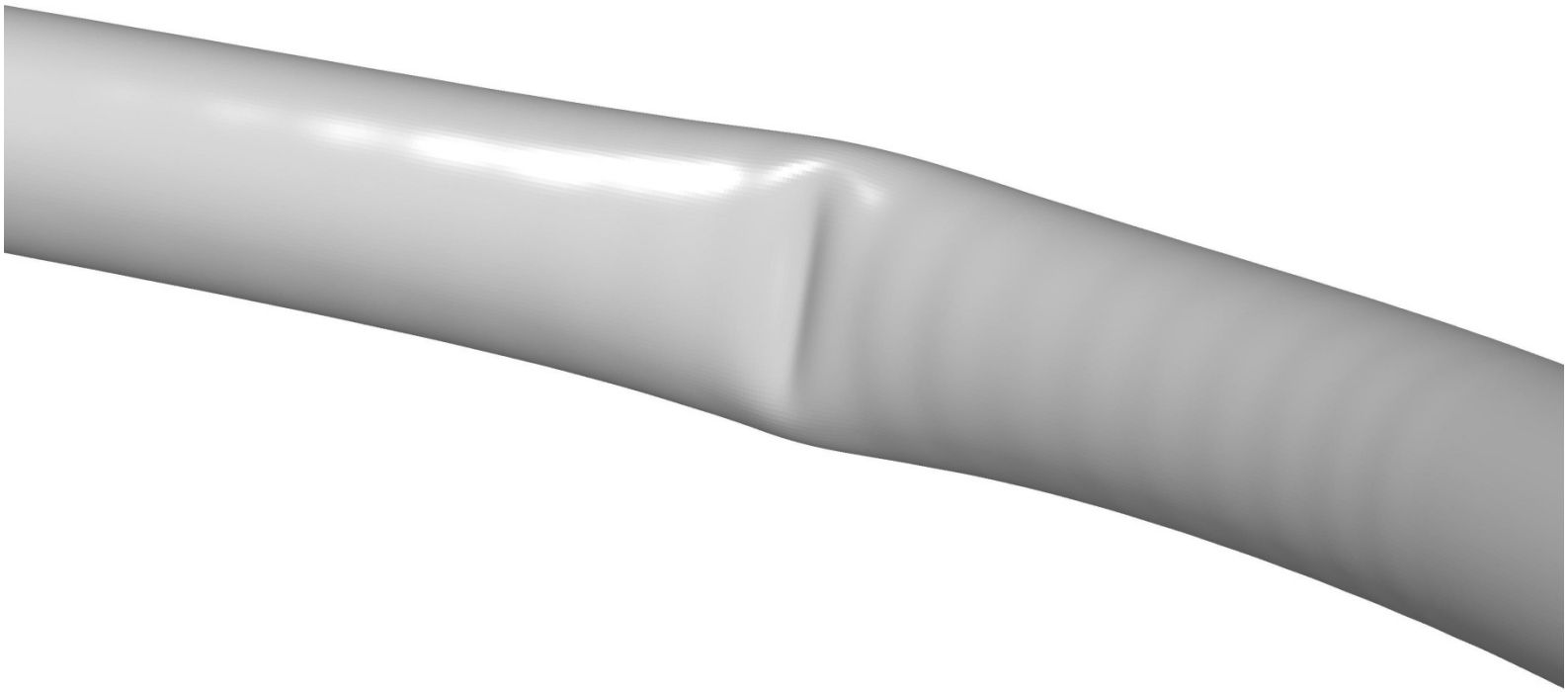

Fig. 4.21 Close-up view of wrinkling and buckled region for LU3-3.

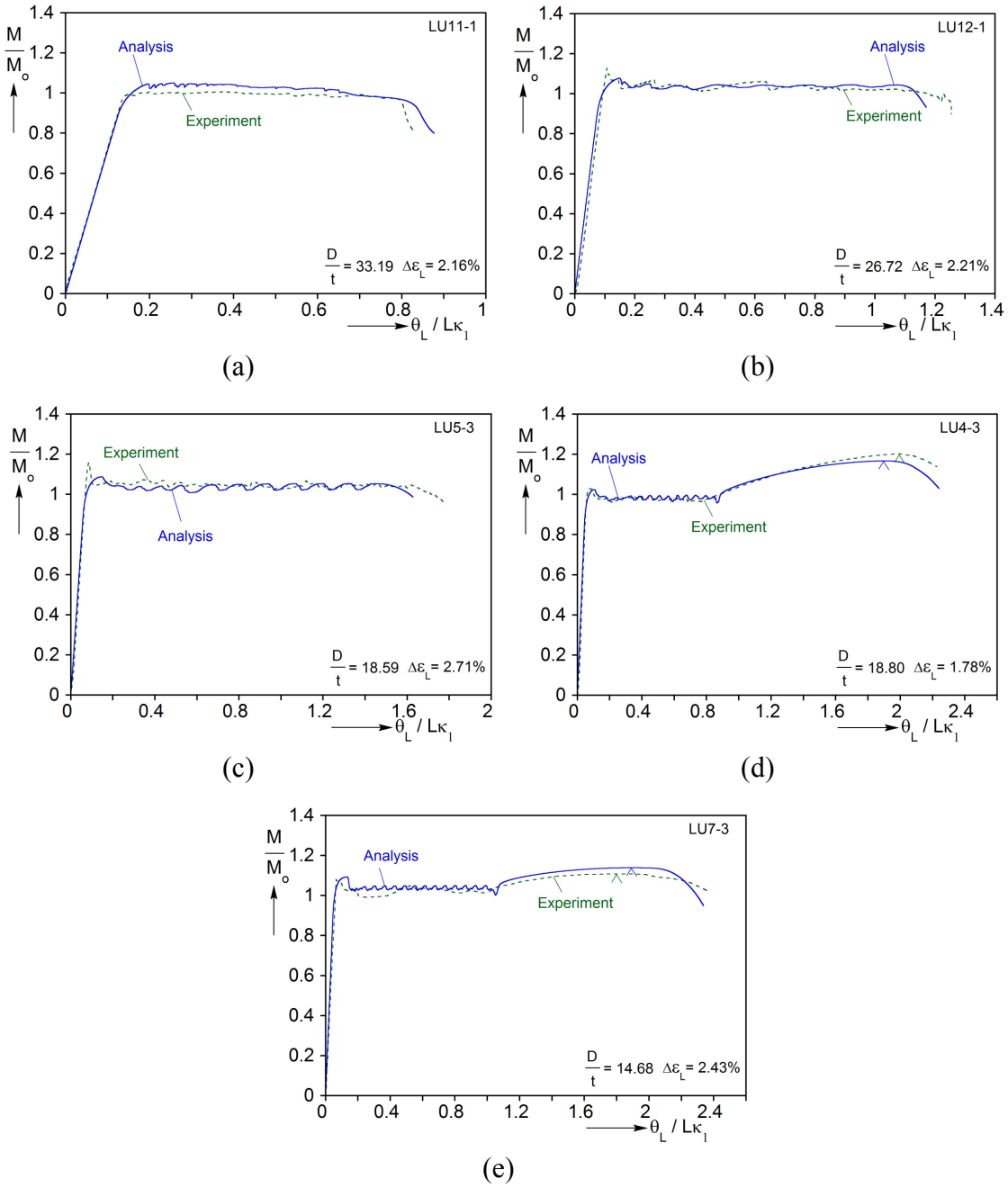

Fig. 4.22 Comparison of measured and calculated moment - end-rotation response for tubes of various D/ts and Lüders strains: (a) LU11-1, (b) LU12-1, (c) LU5-3, (d) LU4-3 and (e) LU7-3.

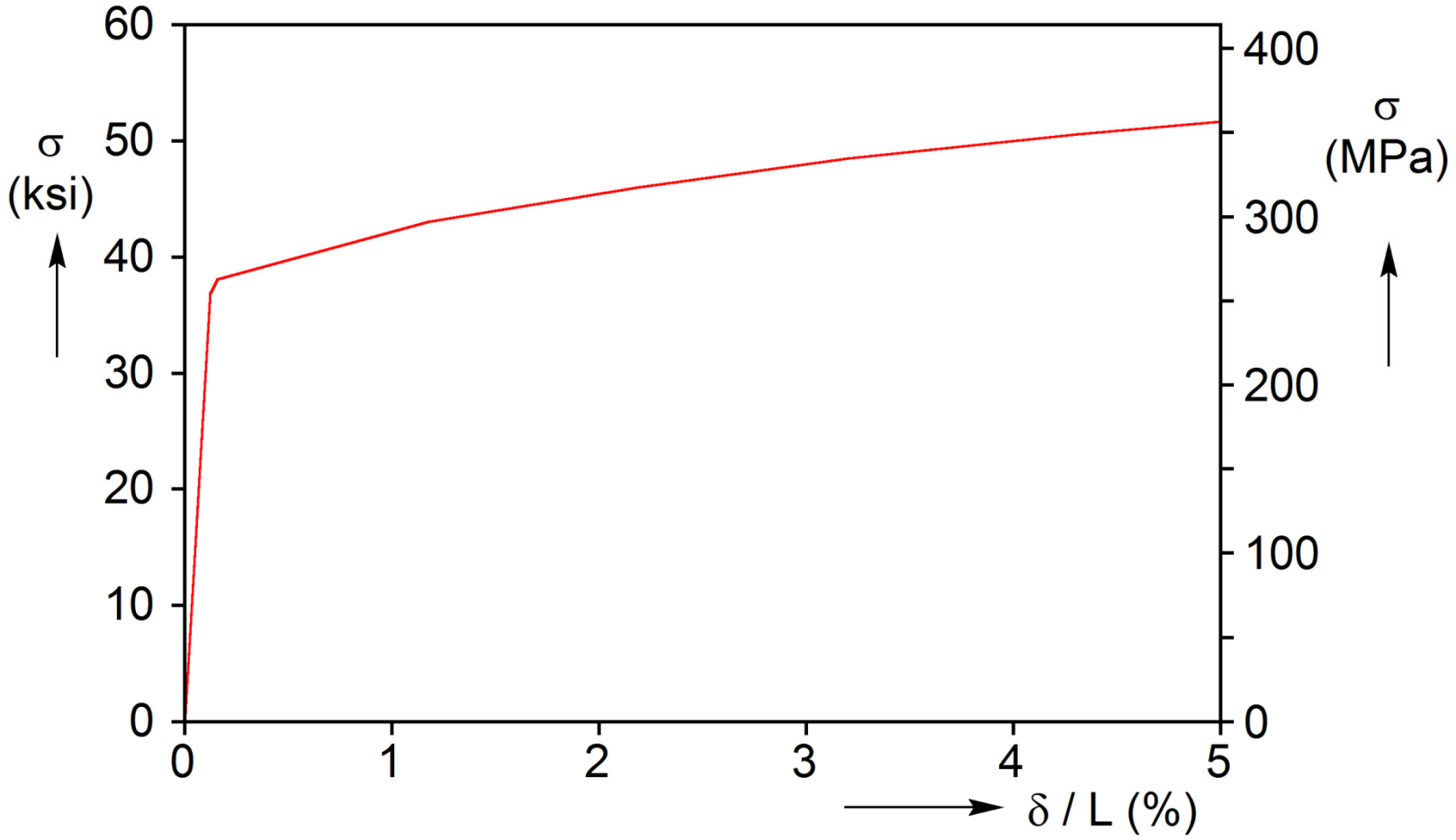

Figure 4.23: Monotonic stress-strain response obtained removing the Lüders plateau in Fig. 4.3.

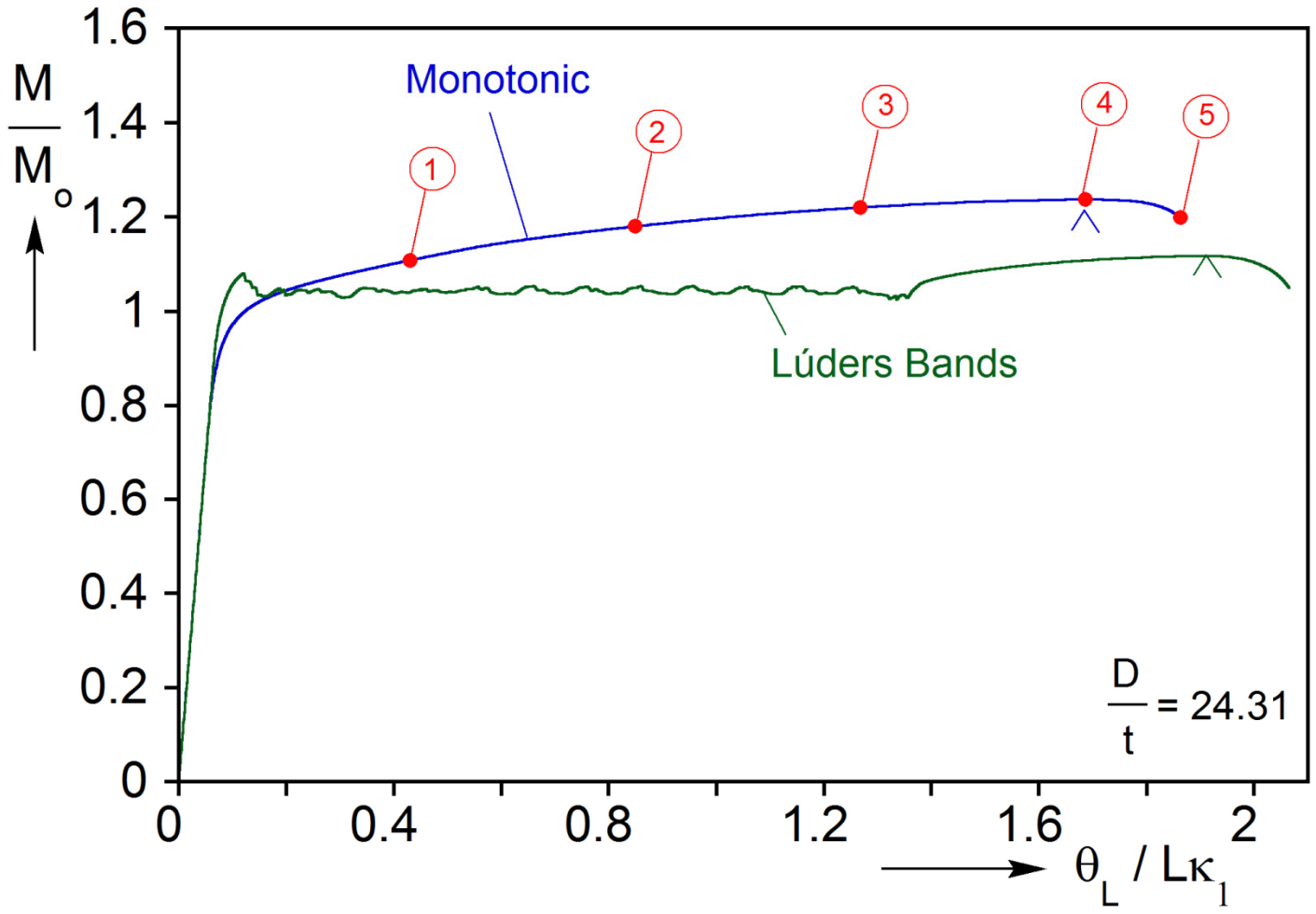

Figure 4.24: Calculated moment - end rotation response for a tube with monotonic stress-strain response.

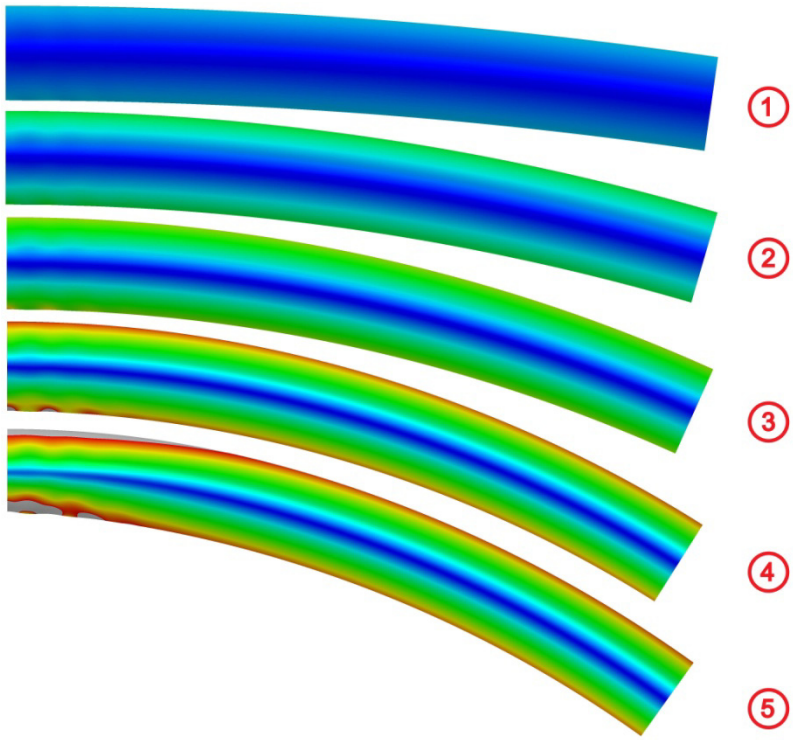

Figure 4.25: Deformed configurations corresponding to the response in Fig. 4.24.

Chapter 5: PARAMETRIC STUDY

In the previous chapter, the numerical framework developed for analyzing the response and assessing the stability of steel tubes with Lüders bands under bending was shown to be capable of reproducing all aspects of the behavior observed in the experiments. In this chapter, some of the key variables of the model are varied in order to demonstrate their effect on the calculated response. In addition, the boundaries of stable bending are established for a range of pipe *D/t* and material properties.

5.1 STRENGTH OF INSTABILITY

Aguirre et al. (2004) pointed out that the slope of the softening part of the assumed response, or alternatively the assumed $\Delta\sigma/\sigma_L$, must be within a certain range for the patterns and sequence of events presented to take place. If $\Delta\sigma/\sigma_L$ is too small, the banded patterns do not develop; if it is too large then there is a tendency for the deformation to "jump" to the hardening part of the response producing a longer and higher moment plateau.

In the present study, this sensitivity was further investigated by varying the $\Delta\sigma/\sigma_L$ (or negative slope) in the assumed stress-strain response. Thus Fig. 5.1 compares bent configurations for models with various values of $\Delta\sigma/\sigma_L$ and $(-E'/E)$. The four cases on the left column have Lüders strain of 1.0% and the ones on the column on the right have 2.0%. Each row has the same value of $\Delta\sigma/\sigma_L$ given in Table 5.1. The configurations correspond to the curvatures at the end of the plateau of the corresponding moment - end rotation response. Interestingly, the Lüders banded patterns for each row are very similar but differ from row to row. However, in the first row with $\Delta\sigma/\sigma_L = 0.081$, the patterns are weak and not fully developed (patterns represent contours of equivalent plastic strain). In the second row, with $\Delta\sigma/\sigma_L = 0.162$, the

patterns are somewhat stronger but still not fully developed. The patterns appear fully developed in rows 3 and 4 with stress amplitudes of 0.243 and 0.324. This trend indicates first that $\Delta\sigma/\sigma_L$ is a viable parameter for defining the strength of the material instability and second that a threshold value must be exceeded before the expected Lüders banding is fully developed.

A second parameter that influences Lüders banding in the bending of tubes is the level of the stress plateau, σ_L. Figure 5.2 shows comparisons of results with two different values of σ_L, 36.9 ksi (254 MPa), for the three cases on the left column and 73.8 ksi (509 MPa) for the three cases on the right. In all cases $\Delta\varepsilon_L = 1.0\%$ and each row has the same $\Delta\sigma/\sigma_L$ given in Table 5.2. Again, the deformation patterns for each row are similar but differ from row to row. Furthermore, similar values of $\Delta\sigma/\sigma_L$ to the ones used for the models in Fig. 5.1 result in the desired Lüders bands pattern. This confirms that $\Delta\sigma/\sigma_L$ is a good choice for characterizing the material instability. The choice of an appropriate range of values of $\Delta\sigma/\sigma_L$ for the simulation of tubes with Lüders bands under bending is discussed in the sensitivity study presented next.

5.2 Sensitivity Study

The success of the modeling framework presented in Chapter 4 in reproducing the experiments is influenced by several model parameters. The parameters used in the simulations were chosen following an extensive sensitivity study the results of which will be summarized here. Figures 5.3 illustrate the effect of $\Delta\sigma/\sigma_L$ on the calculated responses for LU9-1 and LU3-3. For both cases, increasing $\Delta\sigma/\sigma_L$ leads to a higher initiation moment and sharper transition from elastic to plastic deformation and a more ragged moment plateau. In addition, the moment plateau becomes longer, higher, and the larger curvature that develops as it is traversed increases. The lengthening of the plateau

with $\Delta\sigma/\sigma_L$ and the increased raggedness can be seen in Fig. 5.3a for LU9-1. The effects of $\Delta\sigma/\sigma_L$ are more drastic for LU3-1 shown in Fig. 5.3b. Here assigning a small value of $\Delta\sigma/\sigma_L$ shortens the plateau, the associated curvature is smaller and, as a consequence, the whole length is Lüders deformed and the structure returns to uniform deformation; this of course is in conflict with the experiment. If $\Delta\sigma/\sigma_L$ is larger than the optimum value then the plateau is higher and collapse occurs earlier.

The initial geometric imperfection amplitude assumed influences the results to a certain degree also. For LU9-1 shown in Fig. 5.4a increasing the imperfection causes a reduction in the curvature at collapse, which in this case occurs during the second stable branch of the moment-rotation response. In the case of LU3-1 however (Fig. 5.4b), increasing the imperfection causes collapse at a smaller rotation and decreasing it allows the plateau to be completed so that the tube returns to uniform curvature before collapsing. In the simulations, the choice of this variable was guided by the measured variation in diameter of each specimen.

The imperfection parameter β controls the rate of decay or how much of the model is affected by the imperfection. This parameter was instrumental in guaranteeing that the localization started at the symmetry plane and localization propagated from the symmetry plane to the end of the tube. $\beta = 100$ best reproduced the experiments simultaneously enforcing localization at the symmetry plane. Figures 5.5 show the influence of β on the bending response for the same cases studied above. For LU9-1, the more localized the imperfection is, the larger the collapse curvature (see Fig. 5.5a). In the case of LU3-1 (Fig. 5.5b), there is no clear trend when β is increased or decreased.

A rate exponent $m = 0.001$ was found to be optimal in that it made the solution more robust. Figure 5.6 compares the moment-rotation response calculated for LU9-1 for this value of m and one 10 times larger. For the larger value the first moment peak is

more pronounced, the plateau is more ragged and its extent is longer. In addition, the limit moment in the second stable branch is delayed. Even larger values of *m* cause the solution to increasingly deviate from the experimental behavior.

The FE mesh used in the simulations must be fine enough for the banded Lüders patterns to develop properly. Four nearly isotropic meshes were considered with 1, 2, 3 and 4 elements through the thickness. The effect of this mesh refinement on the width of the bands was shown in Fig. 4.10 to be minimal. Figure 5.7 shows that these mesh densities do not influence the plateau in any significant manner but finer mesh delays slightly the onset of collapse. It is also observed that the response of the two most refined meshes are essentially identical. The fine details of the banded patterns are also identical for these most refined meshes (Fig. 5.8).

5.3 PARAMETRIC STUDY

Having established optimal values of the various parameters of the numerical model, a parametric study of the problem is now performed. The objective here is to establish the sensitivity of the boundary between "stable" bending and "unstable" bending to the key problem parameters. In the present context *stable* implies that the structure survives localized bending induced by Lüders banding and *unstable* implies that it collapses because of Lüders banding. The main parameters of interest are the tube *D/t*, the extent of the Lüders strain $(\Delta\varepsilon_L)$, the strength of the instability represented by $\Delta\sigma/\sigma_L$, and the amplitude of the geometric imperfection (a). An additional parameter shown earlier to affect the results, the yield or Lüders stress of the material (σ_L) was also varied. Other parameters like the rate exponent and imperfection parameter β were kept at the values found to produce good agreement between the experiments and the simulations (i.e., $m = 0.001$, $\beta = 100$). The imperfection wavelength was chosen

according to Eq. (3.2). The hardening part of the material response was kept the same as that of the measured stress-strain responses (e.g., see Fig. 3.18). For numerical expediency, in this study the nearly isotropic mesh adopted involved one element through the thickness, which is considered adequate.

Figure 5.9 shows a set of results from this parametric study for a material with a yield stress of 55.4 ksi (382 MPa). Tubes with *D/t* between 18 and 28 were analyzed. For a chosen *D/t*, a trial value of $\Delta\varepsilon_L$ is selected and a bending calculation is performed using the other problem parameters included in the figure. If the tube is successfully bent past the inhomogeneous deformation regime, $\Delta\varepsilon_L$ is increased by 0.25% and the calculation is repeated. The incrementing of $\Delta\varepsilon_L$ is repeated until a value is reached for which the tube collapses due to Lüders banding. In case the tube buckles for the first trial value of $\Delta\varepsilon_L$, its value is decreased by 0.25% and the calculation is repeated. This continues until a value is found for which the tube survives the Lüders banding. The average of the Lüders strains of the last two cases is taken as the *bounding* Lüders strain for this *D/t*, $\Delta\varepsilon_{LB}$.

Similar sets of calculations were performed for other *D/t* values and the calculated $\Delta\varepsilon_{LB}$ are plotted against *D/t* in Fig. 5.9 with solid bullets. Because of the finite size of the increment of $\Delta\varepsilon_L$ used, the final answers have error bounds as marked in the figure. Thus, for $\Delta\varepsilon_L$ values above the drawn boundary the structures will collapse during Lüders banding, and for values below the boundary they will survive Lüders banding and enter the stable, hardening deformation regime. As expected, the critical Lüders strain is strongly dependent on *D/t*. Tubes with relatively high *D/t* values do not survive Lüders banding even for small values of $\Delta\varepsilon_L$ while for the lowest *D/t* analyzed the bounding value exceeds 3%.

The bounding value of $\Delta\varepsilon_L$ is influenced by the Lüders stress in the manner shown in Fig. 5.10a. Here $\Delta\varepsilon_{LB} - D/t$ bounds are generated for three material yield stresses: $\sigma_L = 36.9$, 55.4 and 73.8 ksi (254, 382 and 509 MPa) with the rest of the model parameters kept constant. Interestingly, the higher the material yield stress the lower the bounding Lüders strain. This is partly related to the fact that higher yield stress induces higher ovality making the structure less stiff and more susceptible to collapse.

The imperfection used influences $\Delta\varepsilon_{LB}$ to some degree also. Figure 5.10b shows $\Delta\varepsilon_{LB} - D/t$ plots for three imperfection amplitudes a for a material with $\sigma_L = 36.9$ ksi (254 MPa). Reducing a tends to increase the bounding values of Lüders strain a relatively modest amount. Interestingly the effect of a becomes even smaller for higher values of σ_L.

In summary, the bounding value of Lüders strain that separates stable and unstable bending as defined above is a strong function of *D/t*. Increasing the material yield stress tends to reduce its value while increasing the imperfection amplitude used in such calculations reduces it but less drastically than the other two parameters.

Fig. No.	$\Delta\varepsilon_L$ %	$-E'/E$ %	$\frac{\Delta\sigma}{\sigma_L}$
5.1a	1	1.0	0.081
5.1b	2	0.5	0.081
5.1c	1	2.0	0.162
5.1d	2	1.0	0.162
5.1e	1	3.0	0.243
5.1f	2	1.5	0.243
5.1g	1	4.0	0.324
5.1h	2	2.0	0.324

Table 5.1 Sensitivity study with $D/t = 24$.

Fig. No.	σ_L ksi (MPa)	$\frac{\Delta\sigma}{\sigma_L}$
5.2a	36.9 (254)	0.162
5.2b	73.8 (509)	0.162
5.2c	36.9 (254)	0.203
5.2d	73.8 (509)	0.203
5.2e	36.9 (254)	0.243
5.2f	73.8 (509)	0.243

Table 5.2 Sensitivity study with $D/t = 24$ and $\Delta\varepsilon_L = 1\%$.

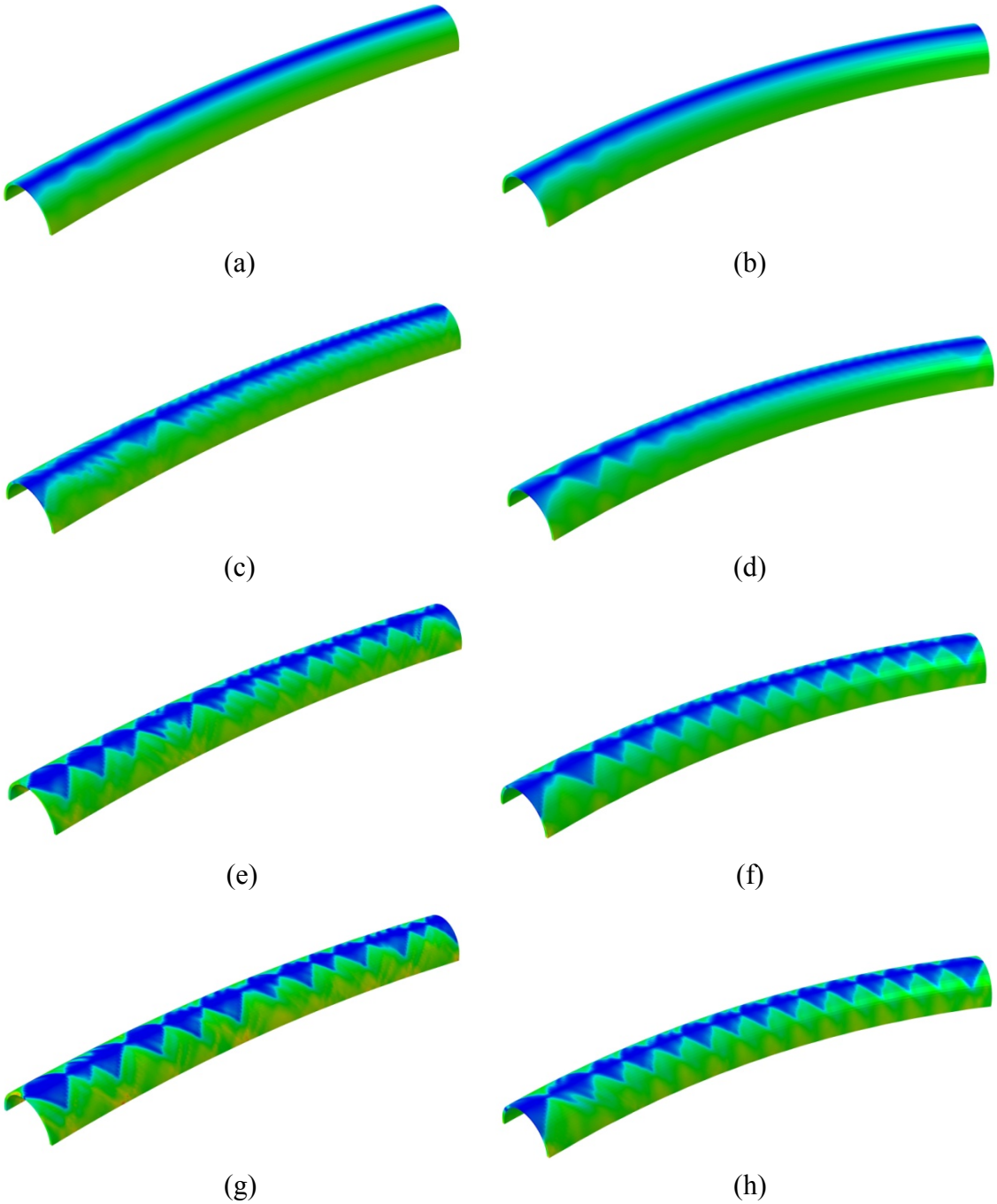

Fig. 5.1 Sensitivity study for $D/t = 24$ (see parameters in Table 5.1).

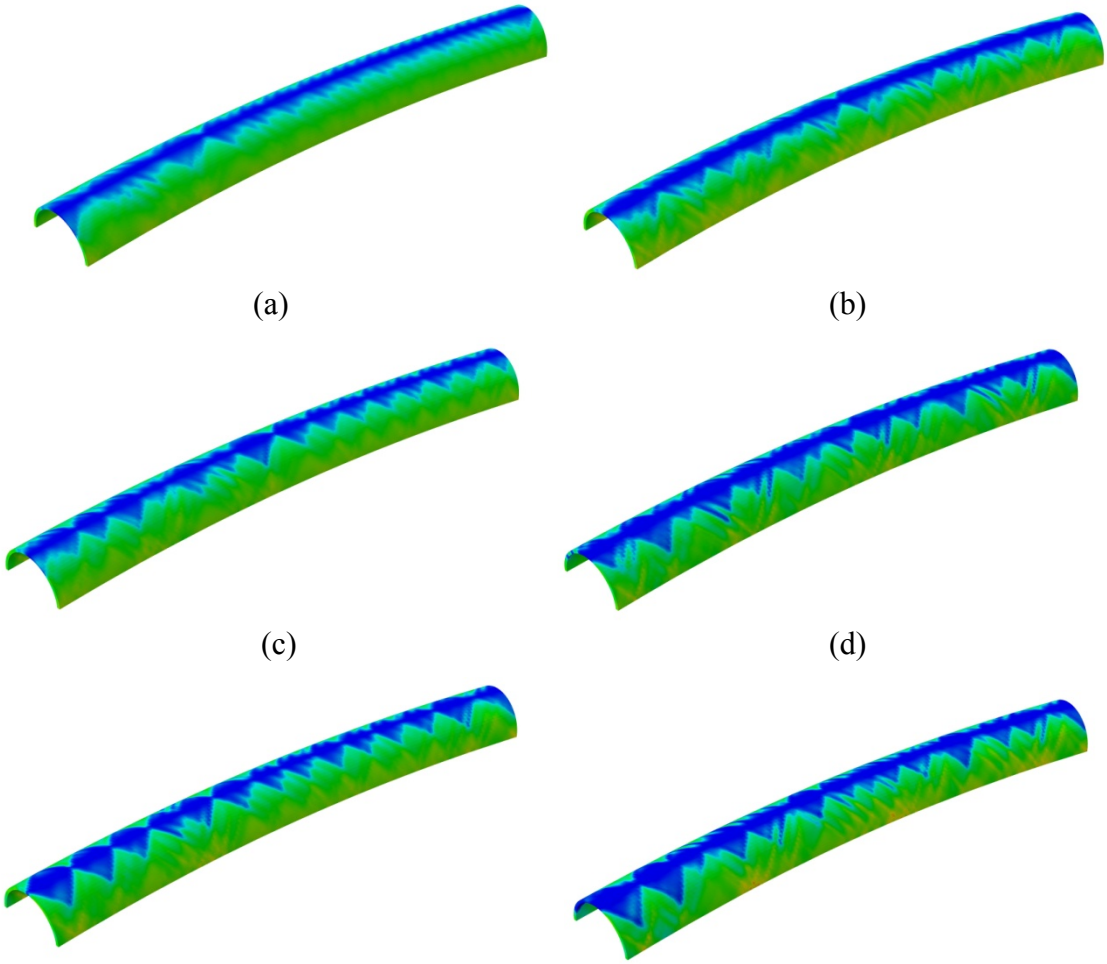

Fig. 5.2 Sensitivity study for $D/t = 24$ and $\Delta\varepsilon_L = 1\%$ (see parameters in Table 5.2).

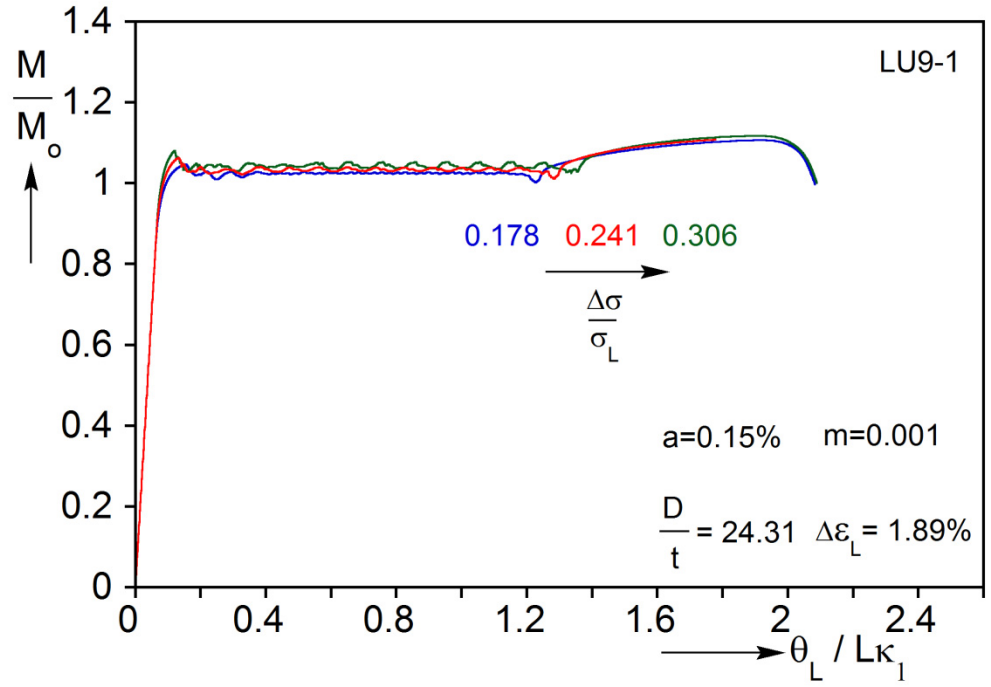

(a)

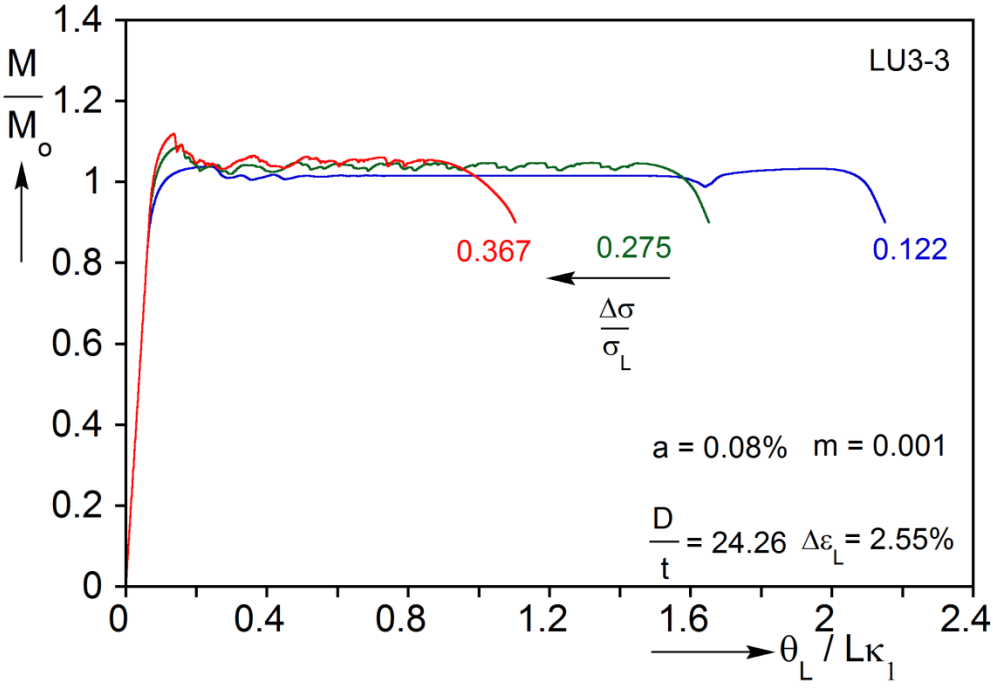

(b)

Fig. 5.3 Influence of the unstable part of the stress-strain response adopted on the calculated moment - end-rotation response for (a) LU9-1 and (b) LU3-3.

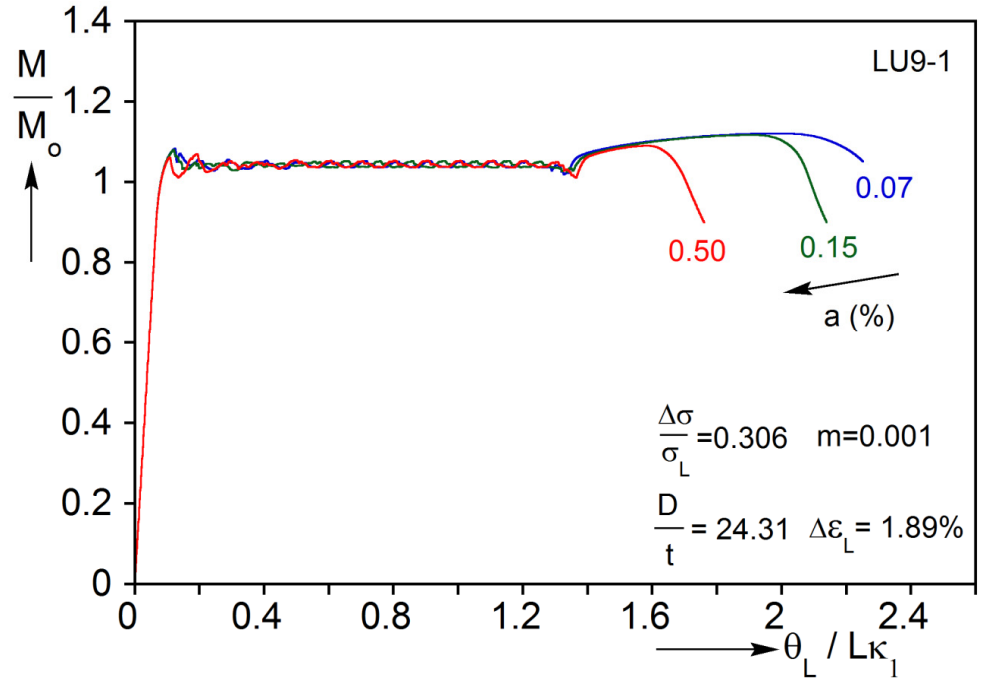

(a)

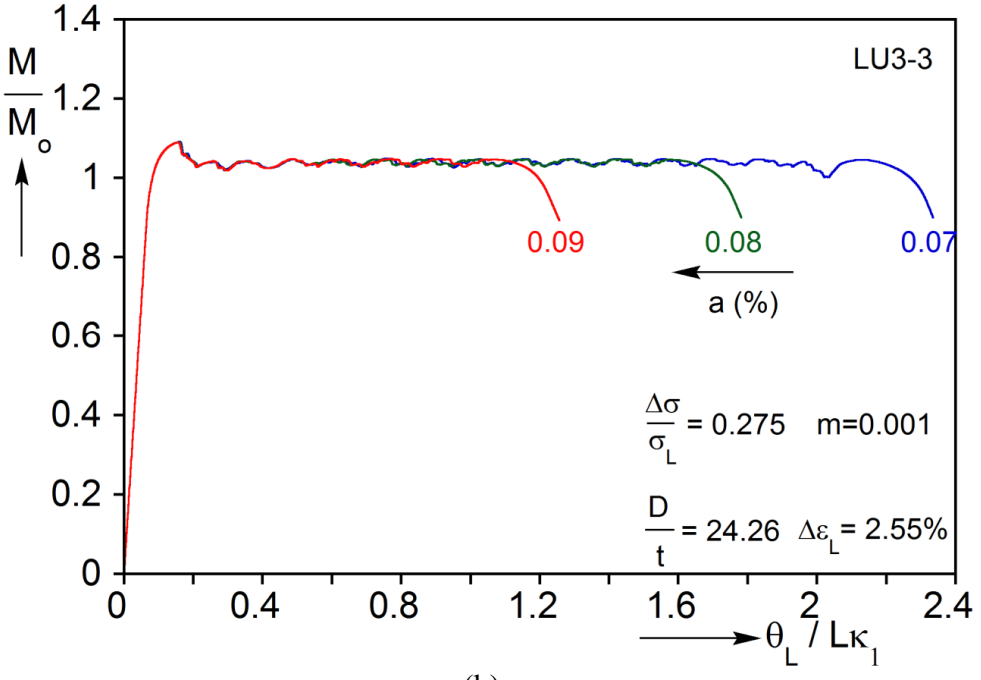

(b)

Fig. 5.4 Influence of the initial imperfection amplitude on the calculated moment - end-rotation response for (a) LU9-1 and (b) LU3-3

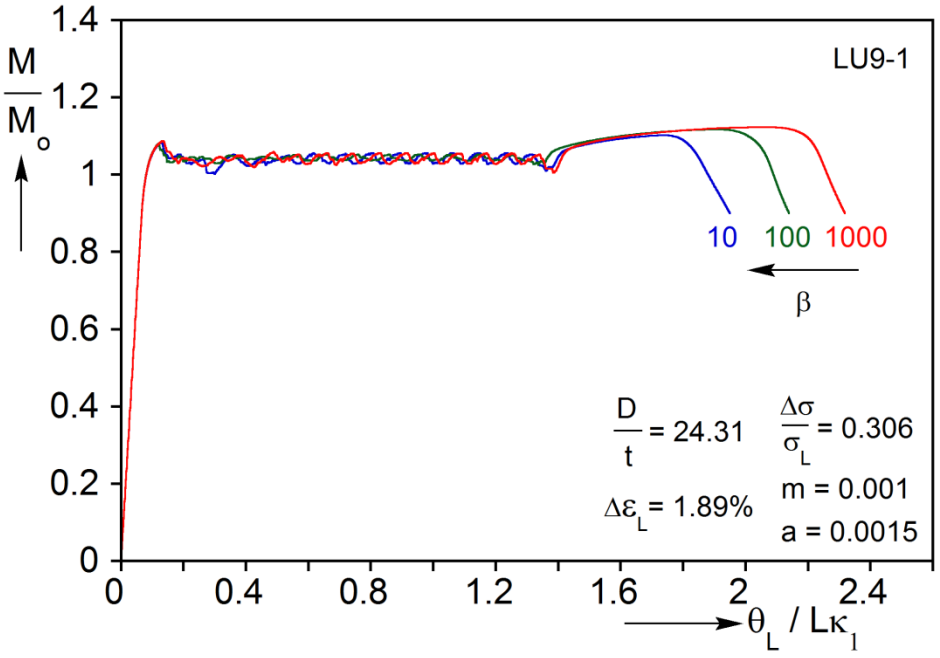

(a)

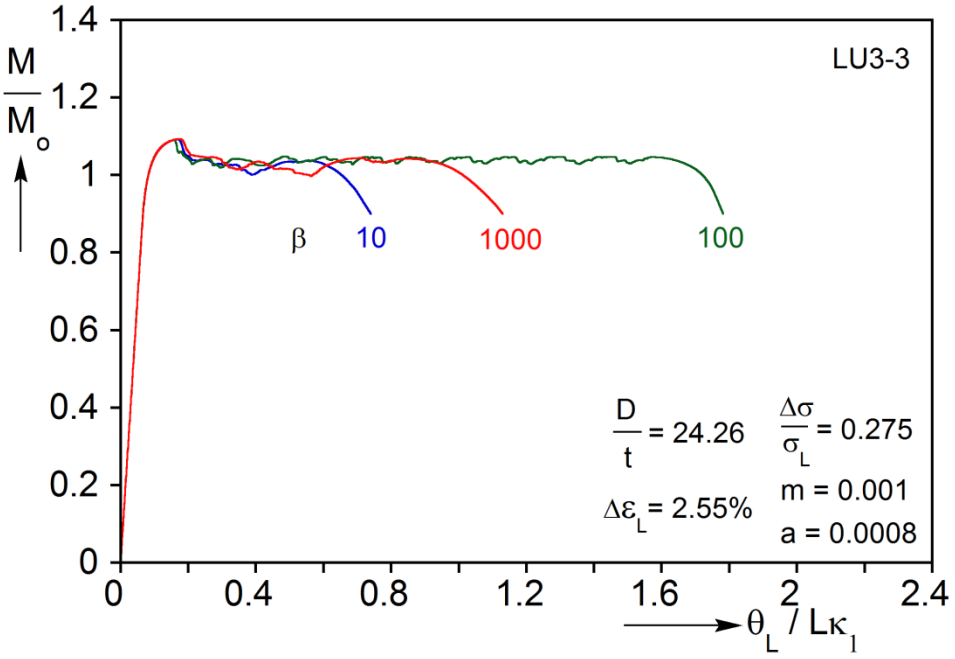

(b)

Fig. 5.5 Influence of the initial imperfection rate of decay on the calculated moment - end-rotation response for (a) LU9-1 and (b) LU3-3.

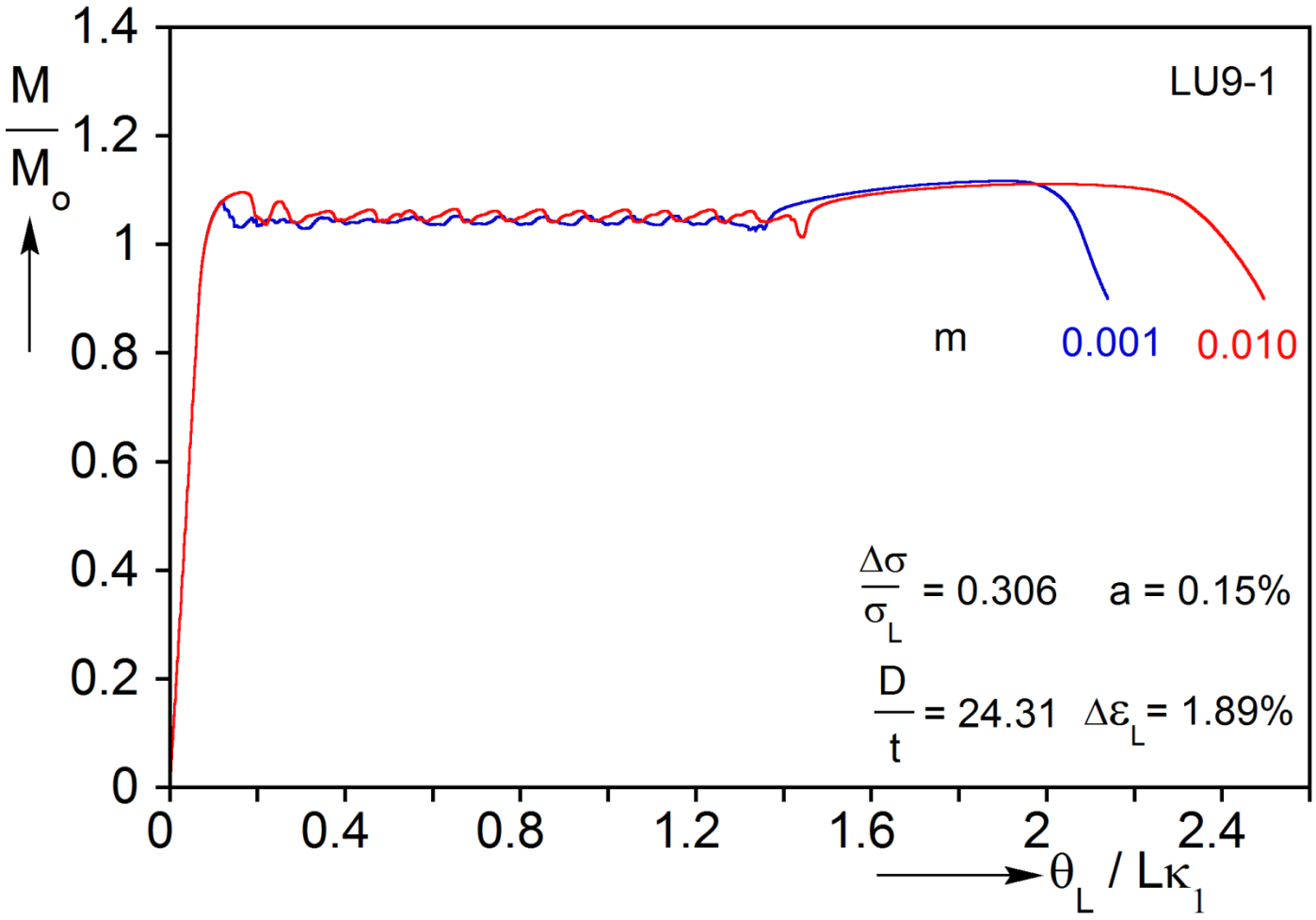

Fig. 5.6 Influence of the rate dependence exponent

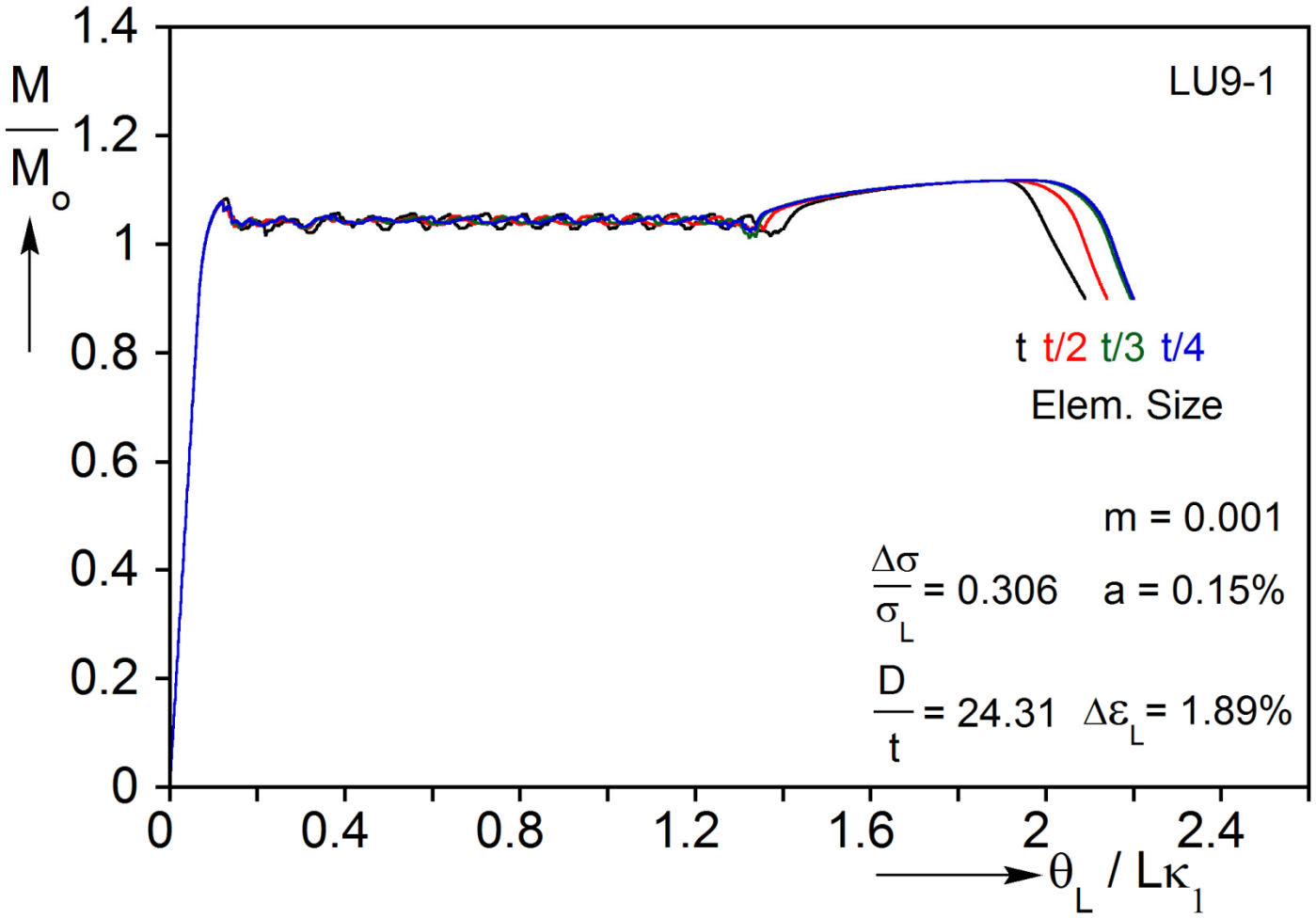

Fig. 5.7 Influence of the size of elements used to discretize the model on the calculated moment - end-rotation response for LU9-1

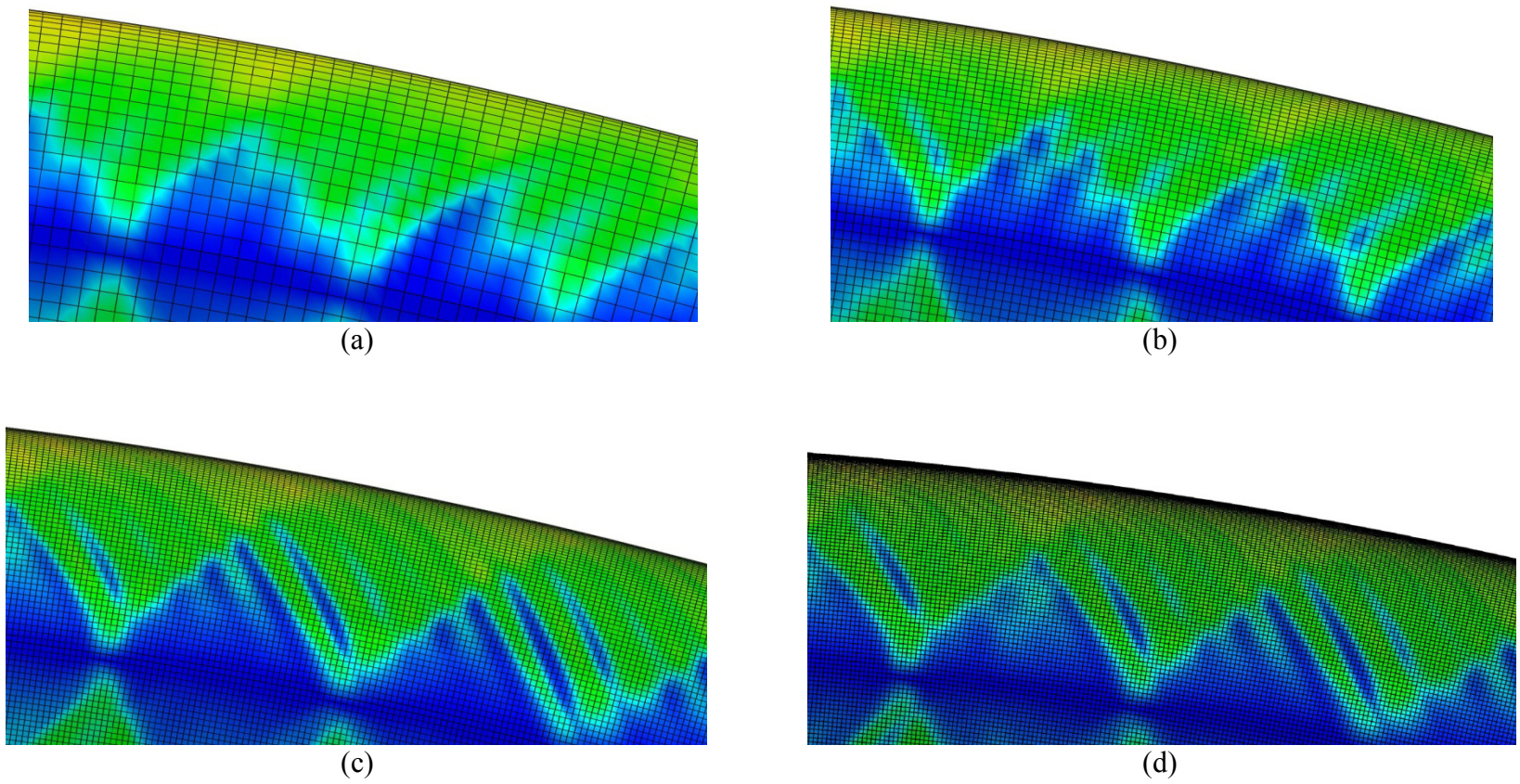

Fig. 5.8 Influence of the size of elements used to discretize the model on the calculated banded patterns. (a) element size t, (b) $t/2$, (c) $t/3$ and (d) $t/4$.

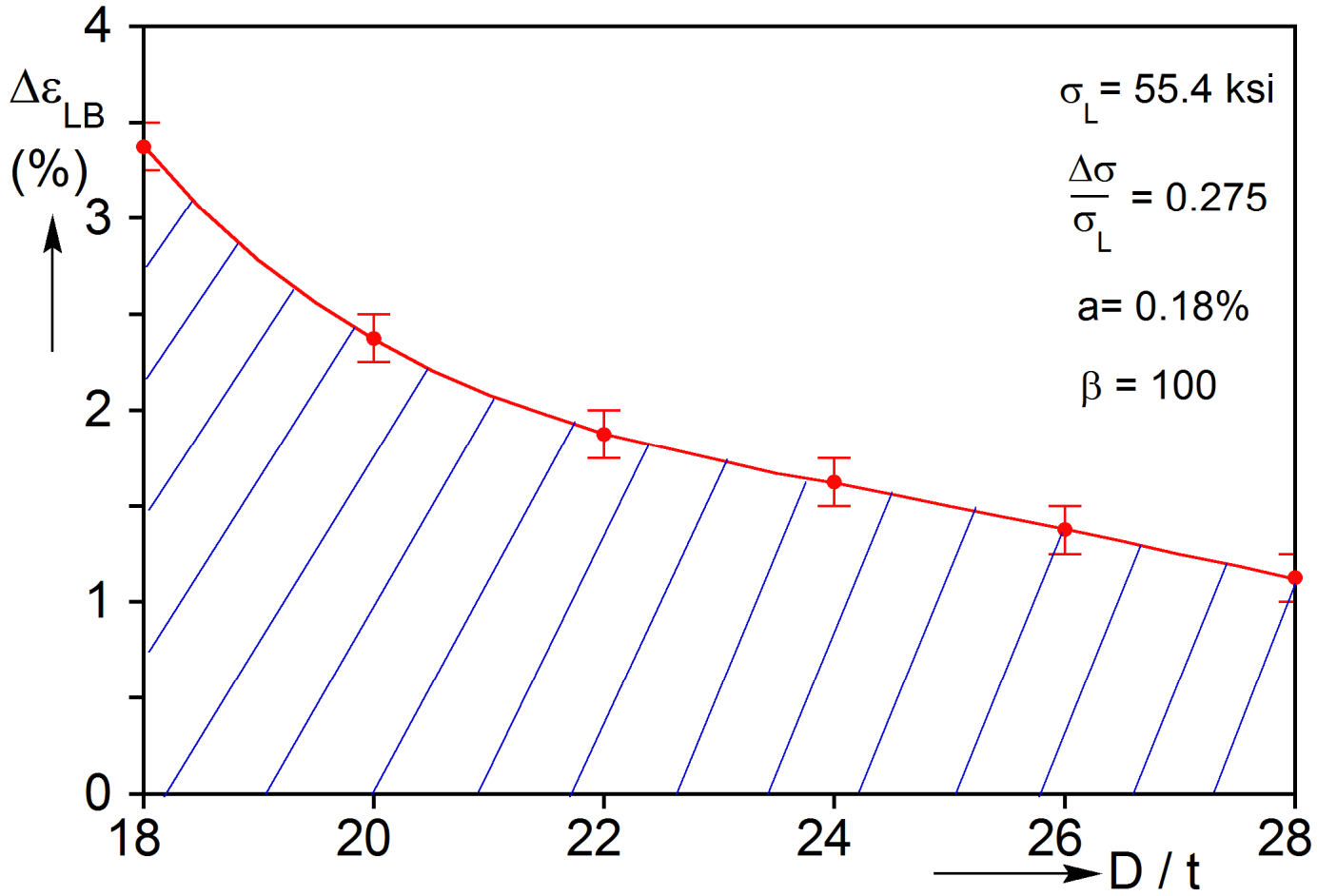

Fig. 5.9 Bounding value of Lüders strain for pure bending as a function of *D/t* for a fixed set of problem parameters.

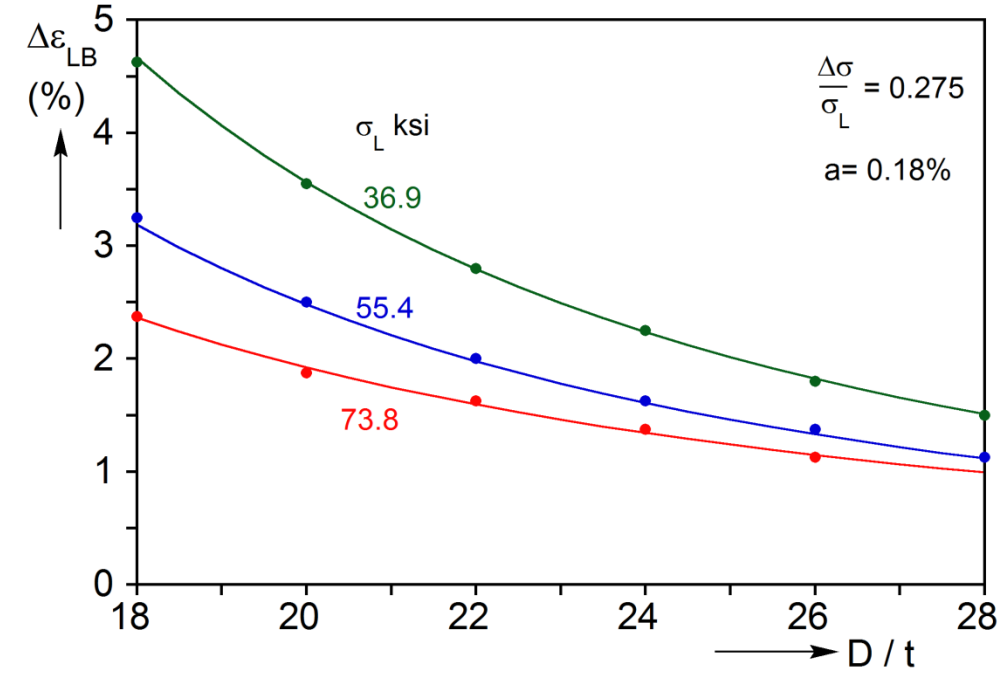

(a)

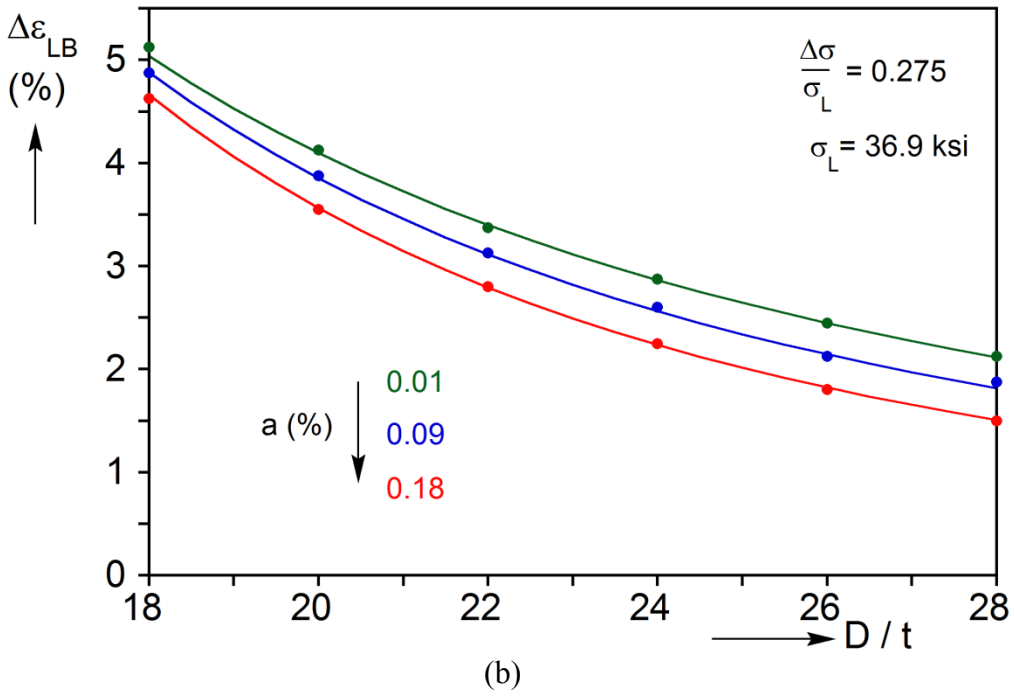

(b)

Fig. 5.10 Bounding value of Lüders strain for pure bending as a function of *D/t* for
(a) three values of material yield stress and
(b) for three imperfection amplitudes.

Chapter 6: CONCLUSIONS

Lüders banding is a dislocation driven phenomenon whose macroscopic effect is inhomogeneous deformation in the early stages of plastic deformation. Thus, for example, in a uniaxial test conducted under displacement control localized deformation of 1-3% nucleates locally and gradually propagates in the rest of the specimen that is still elastic. As this steady state propagation of inclined bands of plastic deformation takes place, the stress traces a nearly constant plateau. When the whole specimen is thus deformed the material returns to stable hardening behavior. This study examined how the localized deformation associated with Lüders banding affects the response of tubes bent into the plastic range as well as the extent to which they can be so bent. The problem has been investigated using a combination of experiments and analysis.

a. Uniaxial Tests

In the way of connecting with past investigations of Lüders banding, the investigation started with experiments and finite element simulation of strips in uniaxial tension. Experiments in which the evolution of localized deformation was monitored with DIC confirmed previously observed steady-state propagation of deformation fronts that separate Lüders deformed and undeformed zones. The tension tests were reproduced using the numerical and constitutive models that were adopted in the more complex problem of bending of tubes.

b. Bending Experiments

Pure bending experiments were conducted on tubes with *D/t* values ranging from 33.2 to 14.7 each with a different value of Lüders strain ($\Delta\varepsilon_L \in 1.8-2.7\%$). Under

rotation controlled bending, the initial elastic regime terminates into a local moment maximum that is followed by nucleation of narrow angled bands of localized deformation on the tension and compression sides of the tubes. As the rotation of the ends increases, the number of bands multiplies and new ones start to spread to the hitherto intact part of the tube while the moment remains relatively constant. The Lüders affected zone develops a significantly larger strain, which translates into localization of curvature. Thus, two curvature regimes co-exist at the same moment level: a larger curvature associated with the end of the moment plateau and a smaller one that corresponds to the beginning of the plateau. How far along the tube the larger curvature propagates depends on the *D/t* and $\Delta\varepsilon_L$.

(a) For tubes with lower *D/t* values and/or shorter Lüders strain the whole structure becomes Lüders deformed, the material enters the hardening regime and continues to deform uniformly until excessive ovalization leads to a limit load instability.

(b) For higher *D/t* tubes and/or longer Lüders strain, the propagation of the larger curvature is interrupted by collapse when a critical length is Lüders deformed leaving behind part of the structure essentially undeformed. The higher the *D/t* and/or the longer the Lüders strain is, the shorter the critical length.

The bending behavior and the stability of such structures are further complicated by the inherent nonlinearities of ovalization of the cross section and by wrinkling. The localization of curvature leads also to locally higher ovalization and the local formation of wrinkles on the compressed side of the tube. The more ovalized higher curvature regime propagates in the manner described above. All tubes tested developed wrinkles but in the case of thicker tubes, the amplitude of the wrinkles was small for most of the bending history becoming more pronounced in the final collapsed zone. The half-wavelengths of the wrinkles, varied between $(0.4-2.0)\sqrt{Dt}$, a result that is in variance

with similar measurements in tubes with a monotonic material response where the variation is only a few percent.

c. Numerical Simulations

A modeling framework was developed for systematically treating the phenomena-rich inhomogeneous bending of tubes associated with Lüders banding. The structure was discretized with incompatible solid elements using a nearly isotropic mesh that is fine enough to allow Lüders bands to develop and evolve. Symmetries in the experimental setup were exploited to reduce the size of the domain analyzed to one fourth of the actual one. A local initial axisymmetric imperfection was introduced about the plane of symmetry of the model. The tube is bent by prescribing the rotation of the ends. Furthermore, without loss of the generality of the results, the free end is required to remain plane but is free to deform in the plane (ovalize). The material was modeled as a finitely deforming, J_2 type, elastic-plastic solid undergoing isotropic hardening/softening, while over the extent of the Lüders deformation an up-down-up stress-strain response was assumed. The introduction of a mild powerlaw rate dependence was found to make the solution more robust, reducing numerical instabilities and facilitating the convergence of the simulation.

This modeling framework was used to simulate successfully the bending experiments for the whole range of D/t and Lüders strains considered. This includes the reproduction of the inhomogeneous bending phase and the associated moment plateau including its extent and, when it occurs, the second homogeneous bending phase associated with hardening material behavior. The following observations can be made from the solutions presented:

(a) The initial elastic regime terminates into a local moment maximum associated with the nucleation of Lüders deformation at the site of the initial imperfections. Initially this is in the form of narrow deformation bands inclined at about 55° to the axis of the tube that appear on the tension and compression sides. The width of the bands was found to be insensitive to the mesh for the meshes considered.

(b) As the tube end rotation increases the bands broaden, they locally multiply in number and new ones start to nucleate next to them. The bands form pockets with a characteristic periodicity. As bands evolve, the local curvature increases to a value that corresponds to that of the eventual end of the moment plateau. Simultaneously, the part of the tube unaffected by Lüders bands remains essentially elastic at a curvature that corresponds to the yield moment. Further rotation of the ends spreads Lüders banding and the high curvature/ovalization zone to the hitherto elastic part of the tube.

(c) The zone of higher curvature experiences also higher ovalization and wrinkles. The higher ovalization provides another way of tracking the evolution of inhomogeneous deformation in the tube. The induced wrinkles have a characteristic wavelength that is close to that of calculated elastic wrinkles. The periodicity of the band pockets is related to that of wrinkles. On the compressed side, the centers of the pockets coincide with the peaks of the wrinkles and on the tension side to the valleys. Wrinkles developed for all tubes analyzed.

(d) Thus, as the higher deformation zone propagates, the local curvature and ovalization increase, wrinkles develop from which bands emanate. The numerical results indicate that all of these develop in a synergistic manner.

(e) As in the experiments, for lower tube D/t and/or shorter Lüders strain, the higher curvature/ovality zone propagates in a steady-state manner to the end of the tube. The

material enters the hardening regime, the moment plateau terminates and the tube deforms uniformly again. This second stable bending regime is terminated when the ovality induced natural limit load instability is reached at which point the tube collapses by diffuse ovalization.

(e) For tubes with higher *D/t* and/or longer Lüders strain, the structure collapses before all of it is Lüders deformed leaving behind a section that is essentially undeformed. Longer Lüders bands induce a higher curvature in the localizing zone. The associated ovalization does not stop growing in the center of the tube and never reaches steady state propagation. Instead, it continually grows in the zone where the Lüders deformation first initiated leading to local collapse. For the highest *D/t* tubes considered (*D/t* >28) the collapse is influenced more by local imperfections and it tends to be more localized.

d. Parametric Study

The sensitivity of such solutions to the problem parameters was studied and ranges for values that lead to optimal performance have been established. In particular, it was shown that the slope of the descending branch of the assumed stress-strain response (or alternatively $\Delta\sigma$) must be within a certain range for the experimental phenomena to be reproduced. If the negative slope is too low, the Lüders patterns and the other associated deformation features do not develop as reported. If the slope is too high, the Maxwell plateau occurs at the wrong level and the numerical stability is adversely affected.

It was observed that cases that survive the inhomogeneous deformation stage exhibit low sensitivity to the mesh density, slope of the unstable part of the stress-strain material response, rate dependence exponent or initial imperfection amplitude. By

contrast, cases that collapse due to inhomogeneous bending are more sensitive to these parameters.

The boundary between stable and unstable bending was established in terms of *D/t* and Lüders strain using selected fixed values of $\Delta\sigma/\sigma_L$, of the rate exponent *m* and the same mesh. The bounding value of Lüders strain was shown to be a strong function of *D/t*. Increasing the material yield stress tends to reduce its value while increasing the imperfection amplitude reduces it but less drastically than the other two parameters.

Appendix A: MOMENT-ROTATION CORRECTION

In Chapter 3 the measured curvature of a tube bent in the bending machine shown in Fig. 3.4, was calculated using the measured sprocket rotations and the *effective* length of the specimen, Eq. (3.1). The effective length can only be estimated within a certain tolerance. Small amount of deformation of the extension rods and, more importantly, deformation of a transition length of the test specimen at the interface with the inserted rods (see Fig. 3.4b) tend to change the effective length by a small amount. Thus, measured curvatures are typically corrected as follows:

$$\kappa = \frac{EI_{measured}}{EI_{theoretical}}\left(\frac{\theta_1 + \theta_2}{2L}\right). \qquad \text{(A.1)}$$

The deformation of all tubes tested was recorded on video so the corrected curvature was checked against the calculated curvature obtained from the video.

The bending moment was also corrected according to Vaze and Corona (1995). The correction addresses the effect of the weight of the solid rod extensions and the small amount of friction in the sprocket assembly rollers on the measured bending moment. The weight correction increases with the angle of rotation at the sprockets and the friction correction increases with the bending moment. In the experiments reported here, the weight correction was usually the dominant component especially so for tubes bent to very high curvatures, which require long extension rods. Thus, for example, for a tube with D/t = 24 the correction is of the order of 5%. Lower D/ts, like the case shown in Fig. A.1 required a larger correction. The moment correction is proportional to $\theta(1-\cos\theta)$ in this case.

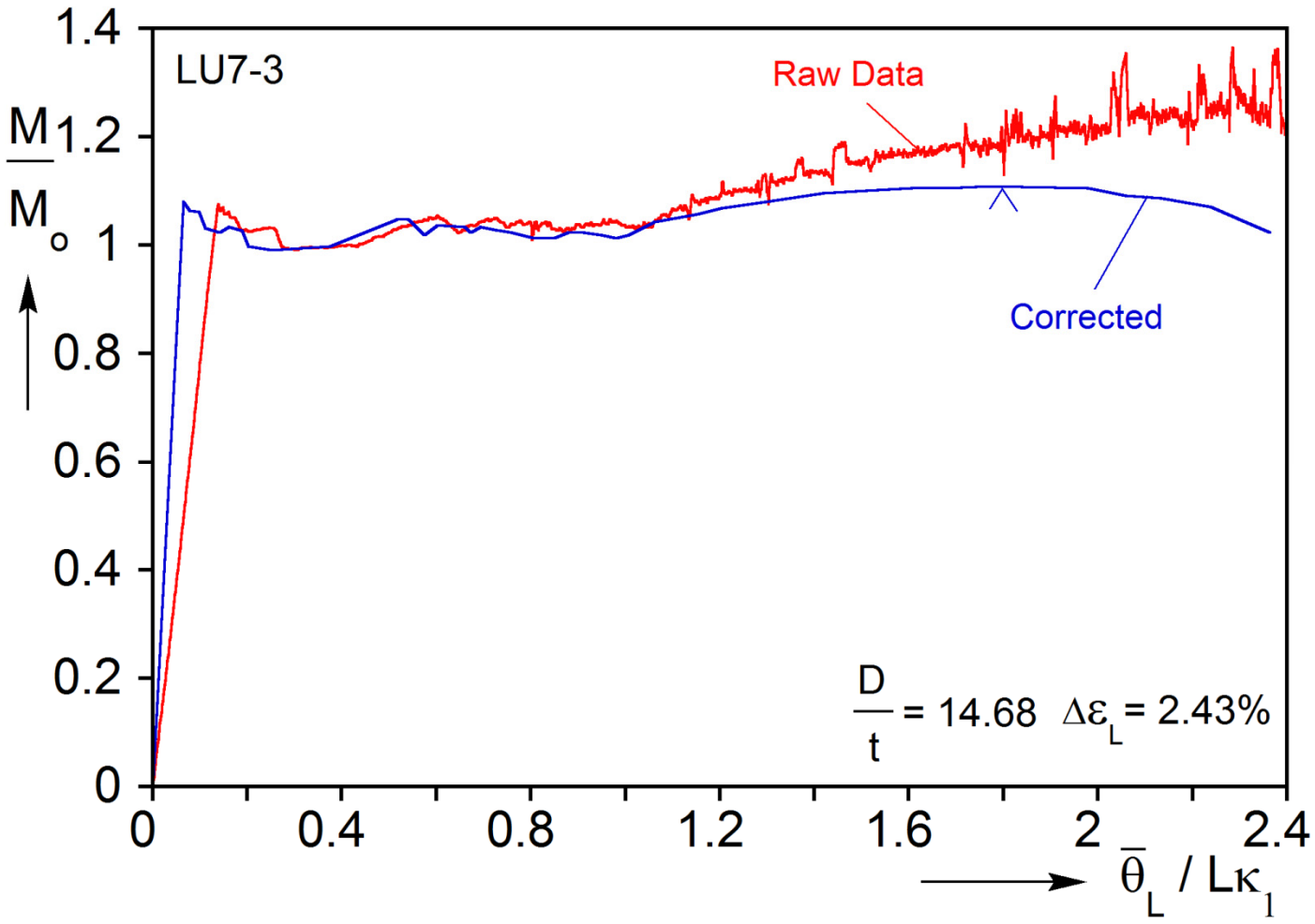

Fig. A.1 Curvature and moment correction.

References

Abeyaratne, R. and Knowles, J.K. (2006). *Evolution of Phase Transitions*. Cambridge University Press, New York.

Aguirre, F. (2002). Bending of tubes with Lüders deformation. MS thesis, Department of Aerospace Engineering and Engineering Mechanics, The University f Texas at Austin

Aguirre, F., Kyriakides, S. and Yun, H.D. (2004). Bending of steel tubes with Lüders bands. *International Journal of Plasticity* **20**, 1199-1225.

Ananthan, V.S. and Hall, E.O. (1991). Macroscopic aspects of Lüders band deformation in mild steel. *Acta Metallurgica et Materialia* **39**, 3153-3160.

Ballarin, V., Soler, M., Perlade, A., Lemoine, X. and Forest, S. (2009). Mechanisms and modelling of bake-hardening steels: Part I. Uniaxial tension. *Metallurgical and Materials Transactions* **40A**, 1367-1374.

Baren, M.R. and Nelson, P.G. (1970). How a fabricator views strain aging of low-carbon sheet steel. *Metal Progress* **98**, 87-95.

Bijlaard, P.P. (1940). Theory of local plastic deformations. *Publication of the International Association of Bridge and Structural Engineers* **6**, 27–44.

Brazier, L.G. (1927). On the flexure of thin cylindrical shells and other thin sections. *Proceedings of the Royal Society of London* **A116**, 104-114.

Bruton, D., Carr, M., Crawford, M. and Poiate, E. (2005). The safe design of hot on-bottom pipelines with lateral buckling using the design guideline developed by the SAFEBUCK joint industry project. *Deep Offshore Technology Conference*.

Carr, M., MacRae, I. and Bruton, D. (2009). Local buckling of pressurized seamless linepipe: results of the SAFEBUCK JIP. *Pipeline Technology Conference*.

Corona, E. and Kyriakides, S. (1988). On the collapse of inelastic tubes under combined bending and pressure. *International Journal of Solids and Structures* **24**, 505-535.

Corona, E. and Kyriakides, S. (1991). An experimental investigation of the degradation and buckling of circular tubes under cyclic bending and external pressure. *Thin-Walled Structures* **12**, 229–263.

Corona, E., Lee, L.-H. and Kyriakides, S. (2006). Yield anisotropy effects on buckling of circular tubes under bending. *International Journal of Solids and Structures* **43**, 7099-7118.

Corona, E., Shaw, J.A. and Iadicola, M.A. (2002). Buckling of steel bars with Lüders bands. *International Journal of Solids and Structures* **39**, 3313-3336.

Cottrell, A.H. and Bilby, B.A. (1949). Dislocation theory of yielding and strain ageing of iron. *Proceedings of the Physical Society* **62/I-A**, 49–62.

Ericksen, J.L. (1975). Equilibrium of bars. *Journal of Elasticity* **5**, 191-201.

Fry, A.D. (1921). Kraftwirkungsfiguren in Flußeisen dargestellt durch ein neues Atzverfahren. *Stahl und Eisen* **41**, 1093-1097.

Fujita, H. and Miyazaki, S. (1978). Lüders deformation in polycrystalline iron. *Acta Metallurgica* **26**, 1273–1281.

Hahn, G.T. (1962). A model for yielding with special reference to the yield-point phenomena of iron and related BCC metals. *Acta Metallurgica* **10**, 727–738.

Hall, E.O. (1950). An Optical Method for Studying the Deformation of Mild Steel. *Proceedings of the Physical Society* **B 63**, 724-726.

Hall, E.O. (1970). *Yield point phenomena in metals and alloys*. Plenum Press, New York.

Hartmann (1896). *Distribution des déformations dans les métaux soumis à des efforts*. Berger-Levrault et Cie, Paris.

Hill, R. (1948). A Theory of the Yielding and Plastic Flow of Anisotropic Metals. *Proceedings of the Royal Society of London. Series A, Mathematical and Physical Sciences* **193**, 281-297.

Hill, R. (1952). On discontinuous plastic states, with special reference to localized necking in thin sheets. *Journal of the Mechanics and Physics of Solids* **1**, 19–30.

Hughes, T.J.R and Ferencz, R.M. (1990). *Finite element methods for nonlinear problems*.

Imamura, J., Hayakawa, H. and Taoka, T. (1971). Contribution of local strain rate at Lüders band front to grain size dependence of lower yield stress in iron. *Transactions of the Iron and Steel Institute of Japan* **11**, 191-200.

Iricibar, R., Panizza, G. and Mazza, J. (1977). On the Lüders band front in mild steel - II. elastic-plastic analysis of the front by the finite element method. *Acta Metallurgica* **25**, 1169–1177.

Itoh, M., Yoshida, F., Yamashita, Y. and Ohmori, M. (1992). FEM analysis for nonuniform yielding processes in mild steel plates under stretching. *JSME International Journal (series I)* **35**, 70-77.

Johnston, W.G. (1962). Yield points and delay times in single crystals. *Journal of Applied Physics* **33**:9, 2716-2730.

Johnston, W.G. and Gilman, J.J. (1959). Dislocation velocities, dislocation densities, and plastic flow in lithium fluoride crystals. *Journal of Applied Physics* **30**, 129–144.

Ju, G.-T. and Kyriakides, S. (1988). Thermal buckling of offshore pipelines. *Journal of Offshore Mechanics and Arctic Engineering* **110**, 355-364.

Ju, G.-T. and Kyriakides, S. (1991). Bifurcation buckling versus limit load instabilities of elastic-plastic tubes under bending and external pressure. *Journal of Offshore Mechanics and Arctic Engineering* **113**, 43-52.

Ju, G.-T. and Kyriakides, S. (1992). Bifurcation and localization instabilities in cylindrical shells under bending: Part II Predictions. *International Journal of Solids and Structures* **29**, 1143-1171.

Kyriakides, S. (1993). Propagating instabilities in structures. In: Hutchinson, J.W., Wu, T.Y. (Eds.), *Advances in Applied Mechanics* **30**, Academic Press, Boston, MA, 67–189.

Kyriakides, S. (2001). Propagating instabilities in materials. In: *Materials Science for the 21th Century, Society of Materials Science, Japan,* **1**, 316–325, May 2001.

Kyriakides, S. and Corona, E. (2007). *Mechanics of Offshore Pipelines: Vol. 1 Buckling and Collapse*. Elsevier, Oxford, UK, Burlington, MA.

Kyriakides, S. and Ju, G.-T. (1992). Bifurcation and localization instabilities in cylindrical shells under bending: Part I Experiments. *International Journal of Solids and Structures* **29**, 1117-1142.

Kyriakides, S. and Miller, J.E. (2000). On the propagation of Lüders bands in steel strips. *Journal of Applied Mechanics* **67**, 645-654.

Kyriakides, S., Ok, A. and Corona, E. (2008). Localization and propagation of curvature under pure bending in steel tubes with Lüders bands. *International Journal of Solids and Structures* **45**, 3074-3087.

Le Chatelier, A. (1909). Influence du temps et de la température sur les essais au choc. *Revue de Métallurgie* **6**, 914-917.

Lomer, W.M. (1952). The yield phenomenon in polycrystalline mild steel. *Journal of the Mechanics and Physics of Solids* **1**, 64–73.

Lüders, W. (1860). Ueber die Aeußerung der Elasticität an stahlartigen Eisenstäben und Stahlstäben, und über eine beim Biegen solcher Stäbe beobachtete Molecularbewegung. *Dingler's Polytechnische Journal*, **155**, 18-22.

Moon, D.W. (1971). Considerations on the present state of Lüders band studies. *Materials Science and Engineering* **8**, 235-243.

Nacar, A., Needleman, A. and Ortiz, M. (1989). A finite element method for analyzing localization in rate dependent solids at finite strains. *Computer Methods in Applied Mechanics and Engineering* **73**, 235–258.

Nakanishi, F. (1929). Strength of mild steel beams under uniform bending. *Journal of the Japan Society of Mechanical Engineers* **32**, 171-178.

Nakanishi, F. (1931). On the yield point of mild steel. *Report of the Aeronautical Research Institute*, **6**, 83-140. Reprinted in: Selected Papers of F. Nakanishi, Dept. of Aeronautics, University of Tokyo, 1966.

Nakanishi, F., Ito, M. and Kitamura, K. (1934). On the yield points of mild steel beams under uniform bending. *Report of the Aeronautical Research Institute*, **8**, 273-290. Reprinted in: Selected Papers of F. Nakanishi, Dept. of Aeronautics, University of Tokyo, 1966.

Needleman, A. (1988). Material rate dependence and mesh sensitivity in localization problems. *Computer Methods in Applied Mechanics and Engineering* **67**, 69-85.

Ortiz, M., Leroy, Y. and Needleman, A. (1987). A finite element method for localized failure analysis. *Computer Methods in Applied Mechanics and Engineering* **61**, 189–214.

Penning, P. (1972). Mathematics of the Portevin-Le Chatelier effect. *Acta Metallurgica* **20**, 1169–1175.

Piobert, G., Morin A.J. and Didion, I. (1842). Commission des principes du tir de l'école de Metz. *Mémorial de l'Artillerie* **5**, 501-552.

Portevin, A. and Le Chatelier, F. (1923). Sur un phénomène observé lors de l'essai de traction d'alliages en cours de transformation. *Comptes Rendus de l'Académie des Sciences, Paris* **176**, 507-510.

Shaw, J.A. (2000). Simulations of localized thermo-mechanical behavior in a NiTi shape memory alloy. *International Journal of Plasticity* **16**, 541-562.

Shaw, J.A. and Kyriakides, S. (1997). On the nucleation and propagation of phase transformation fronts in a NiTi alloy. *Acta Materialia* **45**, 683-700.

Shaw, J.A. and Kyriakides, S. (1998). Initiation and propagation of localized deformation in elasto-plastic strips under uniaxial tension. *International Journal of Plasticity* **13**, 837–871.

Shioya, T. and Shiroiri, J. (1976). Elastic-plastic analysis of the yield process in mild steel. *Journal of the Mechanics and Physics of Solids* **24**, 187–204.

Shioya, T. and Machida, T. (1984). Yield process of mild steel in plane problems. *International Journal of Solids and Structures* **20**, 953-961.

Simo, J.C. and Armero, F. (1992). Geometrically non-linear enhanced strain mixed methods and the method of incompatible modes. *International Journal for Numerical Methods in Engineering* **33**, 1413–1449.

Tsukahara, H. and Iung, T. (1998). Finite element simulation of the Piobert-Lüders behavior in an uniaxial tensile test. *Materials Science and Engineering* **A248**, 304-308.

Tsukahara, H. and Iung, T. (1999). Piobert-Lüders and Portevin-Le Chatelier instabilities. Finite element modelling with ABAQUS. *Journal de Physique IV* **9, Pr9** 157-164.

van Rooyen, G.T. (1968). The stress and strain distribution in a propagating Lüders front accompanying the yield-point phenomenon of iron. *Materials Science and Engineering* **3**, 105-117.

Vaze, S. and Corona, E. (1995). Effect of friction and weight of solid rod extensions on Moment Measurement in Four Point Bending Device. Structural/Solid Mechanics Laboratory Report No. 95/4, Department of Aerospace and Mechanical Engineering, University of Notre Dame.

Wenman, M.R. and Plant, R.D. (2006). Simple model of Lüders behaviour in a novel compact tension specimen for investigation of residual stress effects. *Proceedings of the 2006 ASME Pressure Vessels and Piping Division Conference, PVP2006-ICPVT-11-93450*, 607-613.

Wilson, E.L., Taylor, R.L., Doherty, W.P. and Ghaboussi, J. (1973). Incompatible displacement models. In: Fenves, S.J. et al. (Eds.), *Numerical and Computer Models in Structural Mechanics*. Academic Press, New York.

Yoshida, F. (2000). A constitutive model of cyclic plasticity. *International Journal of Plasticity* **16**, 359-380.

Yoshida, F., Kaneda, Y. and Yamamoto, S. (2008). A plasticity model describing yield-point phenomena of steels and its application to FE simulation of temper rolling. *International Journal of Plasticity* **24**, 1792-1818.

Zhang, Y.T., Ao, T, Jiao, W. and Cui, Y.H. (2008). Prediction of the Lüders band in fine grained steel strips under uniaxial tension. *Computational Materials Science* **41**, 547-552.

Vita

Julian de Freitas Hallai entered the Polytechnic School of the University of São Paulo in 1996 and graduated in 2000 with a 5-year Diploma in Naval Architecture and Marine Engineering with concentration on structures; he graduated at the top of his class and received the "SOBENA" and "Marinha do Brasil" awards. He subsequently earned a Master's degree in Naval Architecture and Marine Engineering at the same university with a thesis entitled "Mooring Line Damping" on the dynamic analysis of mooring lines of floating offshore platforms. After 4 years in the offshore industry, in August 2006, he entered the Graduate School of The University of Texas at Austin to pursue a Ph.D. degree in Engineering Mechanics. Among other activities, he taught Mechanics of Solids as an assistant instructor in the Department of Aerospace Engineering and Engineering Mechanics. He made several presentations at national meetings and co-authored the following conference and journal publications:

Hallai, J.F. and Kyriakides, S. (2011). "On the Effect of Lüders Bands on the Bending of Steel Tubes. Part I: Experiments", *Int. J. Solids and Structures* **48**, 3275-3284.

Hallai, J.F. and Kyriakides, S. (2011). "On the Effect of Lüders Bands on the Bending of Steel Tubes. Part II: Analysis", *Int. J. Solids and Structures* **48**, 3285-3298.

Hallai, J.F. and Kyriakides, S. (2010). "Effect of Lüders Bands on the Bending Capacity of Steel Tubes", *Proceedings of the 29th International Conference on Ocean, Offshore and Arctic Engineering, Shanghai, China, June 6-11, 2010*, OMAE2010-20982.

Permanent address: jhallai@hotmail.com

This dissertation was typed by the author.